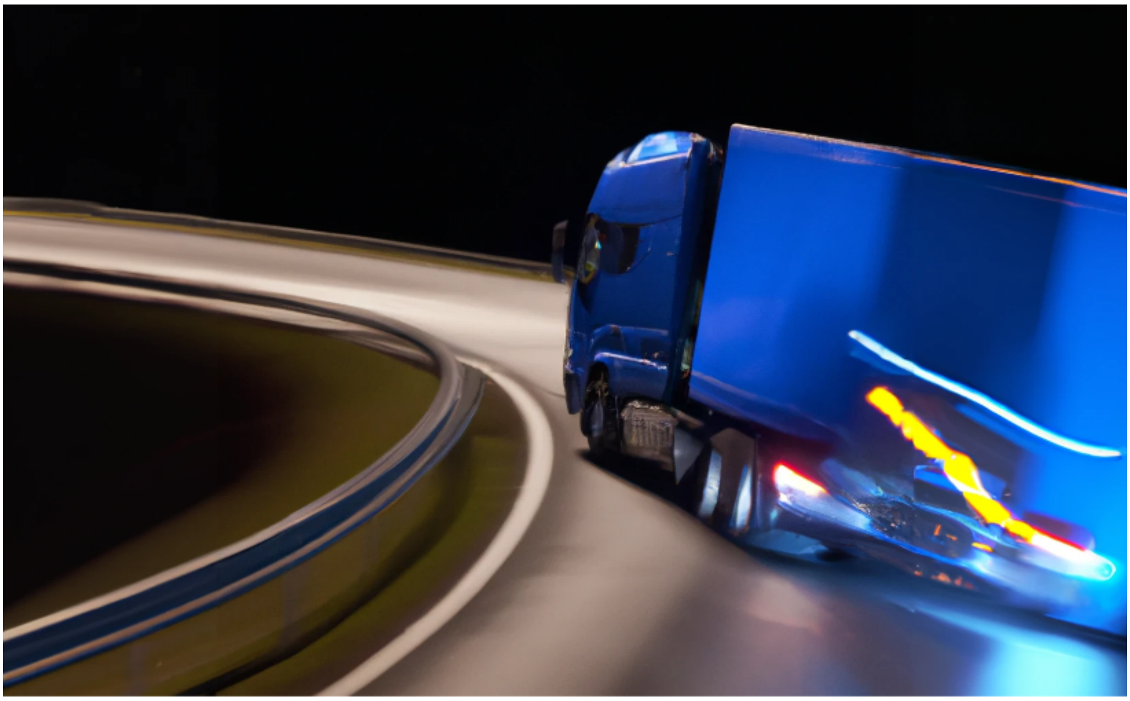

Predictive Threat Assessment for Early Rollover Detection in Articulated Heavy Vehicles

Detecting Potential Rollovers by Incorporating Road Geometry Data into Predictive Algorithm

Master's thesis in System, Control and Mechatronics

NICHOLAS GRANLUND, MARTIN LAMM

DEPARTMENT OF ELECTRICAL ENGINEERING
CHALMERS UNIVERSITY OF TECHNOLOGY
Gothenburg, Sweden 2024
www.chalmers.se

Master's thesis 2024

Predictive Threat Assessment for Early Rollover Detection in Articulated Heavy Vehicles

Detecting Potential Rollovers by Incorporating Road Geometry Data into Predictive Algorithm

NICHOLAS GRANLUND

MARTIN LAMM

Department of Electrical Engineering
Division of Systems and Control
Chalmers University of Technology
Gothenburg, Sweden 2024

Predictive Threat Assessment for Early Rollover Detection in Articulated Heavy Vehicles
Detecting Potential Rollovers by Incorporating Road Geometry Data into Predictive Algorithm
NICHOLAS GRANLUND
MARTIN LAMM

Supervisor: Leon Henderson, Volvo GTT, Chalmers University of Technology
Examiner: Paolo Falcone, Department of Electrical Engineering, Chalmers University of Technology

Master's Thesis 2024
Department of Electrical Engineering
Division of Systems and Control
Chalmers University of Technology
SE-412 96 Gothenburg
Telephone +46 31 772 1000

Cover: AI-generated image of generic truck approaching a turn at high velocity, reaching an unstable state.

Typeset in LaTeX
Printed by Chalmers Reproservice
Gothenburg, Sweden 2024

Predictive Threat Assessment for Early Rollover Detection in Articulated Heavy Vehicles
Detecting Potential Rollovers by Incorporating Road Geometry Data into Predictive Algorithm
NICHOLAS GRANLUND
MARTIN LAMM
Department of Electrical Engineering
Chalmers University of Technology

Abstract

Due to the high center of mass and heavy payload, rollovers is a serious threat towards heavy articulated vehicles. Studies have shown that rollovers are more common on poorly designed roads [3, 7], prompting the question of whether future rollover risks can be detected if the road geometry is known. The thesis proposes a predictive threat assessment, that has the potential to detect rollovers up to 3 seconds before they occur, according to the simulation results presented in the manuscript. The predictive threat assessment proposed in this thesis utilizes a linear vehicle model to predict the future state of the vehicle along with uncertainties of the predictions. The linear model was evaluated against a high-fidelity model. To predict the future road properties and the driver inputs, a road model and a predictive driver model was developed. An extended Kalman filter was also implemented using the vehicle model to estimate the vehicles current state and uncertainties. The conclusion from the study is that it is indeed possible to predict the threat of rollovers, given that the road is known. The results sow that the proposed predictive threat assessment algorithm can predict the vehicle state trajectory up to 3s in simulation, while the risk of rollover is quantified as a probability. We show that the proposed method is flexible, where it becomes a question of optimizing tuning parameters to perform an accurate threat assessment.

Keywords: rollover, predictive threat assessment, vehicle dynamics, road geometry, road banking, road grade, stochastic modelling, uncertainties.

Acknowledgements

This thesis would not have been possible without the support, guidance, and encouragement of many individuals.

First and foremost, we would like to express our gratitude to our industrial Supervisor Leon Henderson. His expertise, insightful feedback, and continuous dedication have been essential for the completion of this thesis.

We would also like to thank Lei Ni and Cecilia Bustrén for demonstrating profound interest in our thesis and for generously offering valuable suggestions, and encouragement throughout the entire process.

We are also grateful to our examiner and academic supervisor, Paolo Falcone. His extensive expertise in the field, and invaluable advice have guided the direction of our research.

Finally, we want to thank all the members of the Vehicle Motion Management team at Volvo Group Truck Technology. Their warm welcome and inclusive approach have made us feel deeply appreciated and respected as a part of the team. You really made this journey a pleasant experience.

Thank you all for your contributions to this work.

Nicholas Granlund, Gothenburg, June 2024
Martin Lamm, Gothenburg, June 2024

List of Acronyms

Below is the list of acronyms that have been used throughout this thesis listed in alphabetical order:

AD	Autonomous Driving
ADAS	Advanced Driver Assistance Systems
AHV	Articulated Heavy Vehicle
CDF	Cumulative Distribution Function
COM	Center Of Mass
EOM	Equations Of Motion
ESC	Electronic Stability Control
HD	High Definition
LTR	Load Transfer Ratio
LTV	Linear Time Variant
MSE	Mean Squared Error
NHTSA	National Traffic Highway Safety Administration
ODE	Ordinary Differential Equation
PDF	Probability Density Function
PID	Proportional – Integral – Derivative (controller)
RK	Runge-Kutta
SMA	Simple Moving Average
SPDM	Simple Predictive driver model
TCS	Tyre Coordinate System
VCS	Vehicle Coordinate System
VGTT	Volvo Group Trucks Technology
VTM	Volvo Transport Models
WCS	World Coordinate System

Nomenclature

Below is the nomenclature of indices, sets, parameters, and variables that have been used throughout this thesis sorted according to area.

Indices

i	Index for vehicle unit	[.]
j	Index for vehicle unit wheel axle	[.]
k	Index for discrete time step	[.]
n	Index for arbitrary prediction time step	[.]
p	Index for prediction time step	[.]

Vehicle Dynamics Parameters and Variables

$\lambda_{b,i}$	Road bank angle for vehicle unit i	$[rad]$
$\lambda_{g,i}$	Road grade angle for vehicle unit i	$[rad]$
m_i	Mass of vehicle unit i	$[kg]$
h_i	Height of center of mass of vehicle unit i	$[kg]$
w_i	Wheel axle length of vehicle unit i	$[kg]$
g	Gravitational acceleration	$[m/s^2]$
$I_{xx,i}$	Moment of inertia around x-axis for unit i	$[kg \cdot m^2]$
$I_{yy,i}$	Moment of inertia around y-axis for unit i	$[kg \cdot m^2]$
$I_{zz,i}$	Moment of inertia around z-axis for unit i	$[kg \cdot m^2]$
$x_{a,ij}$	Distance from COM of unit i to axle j	$[m]$
$x_{c,ij}$	Distance from COM of unit i to coupling point on unit j	$[m]$

$s_{y,ij}$	Lateral slip of unit i on wheel axle j	$[.]$
$C_{y,ij}$	Tire cornering stiffness	$[N/.]$
$CC_{y,ij}$	Lateral slip stiffness coefficient	$[./N]$
$v_{x,i}$	Longitudinal velocity of vehicle unit i in VCS	$[m/s]$
$v_{y,i}$	Lateral velocity of vehicle unit i in VCS	$[m/s]$
$v_{X,i}$	Longitudinal velocity of vehicle unit i in WCS	$[m/s]$
$v_{Y,i}$	Lateral velocity of vehicle unit i in WCS	$[m/s]$
$v_{xw,i}$	Longitudinal velocity of wheels of unit i in TCS	$[m/s]$
$v_{yw,i}$	Lateral velocity of wheels of unit i in TCS	$[m/s]$
$a_{x,i}$	Longitudinal acceleration of vehicle unit i in VCS	$[m/s^2]$
$a_{y,i}$	Lateral acceleration of vehicle unit i in VCS	$[m/s^2]$
δ	Steering wheel angle	$[rad]$
α	Wheel slip angle	$[rad]$
ϕ_i	Yaw angle at centre of gravity for vehicle unit i	$[rad]$
$\dot{\phi}_i$	Yaw angle rate at centre of gravity for vehicle unit i	$[rad/s]$
$\ddot{\phi}_i$	Angular acceleration at centre of gravity for vehicle unit i	$[rad/s^2]$
θ_i	Articulation angle between vehicle unit i and $i+1$	$[rad]$
$\dot{\theta}_i$	Articulation angle rate between vehicle unit i and $i+1$	$[rad/s]$

Euler-Lagrange Parameters and Variables

t	Time variable	$[s]$
$\mathbf{q}$	Generalized coordinates	
$\dot{\mathbf{q}}$	Time derivatives of the generalized coordinates	
$\mathbf{Q}$	External forces acting on the generalized coordinates $\mathbf{q}$	
$\mathcal{L}$	The Lagrangian	
T	Kinetic energy of the system	
U	Potential energy of the system	
$\frac{\partial \mathcal{L}}{\partial \dot{\mathbf{q}}_\mathbf{i}}$	Partial derivative of the Lagrangian w.r.t $\dot{q}_i$	
$\frac{\partial \mathcal{L}}{\partial \mathbf{q}_\mathbf{i}}$	Partial derivative of the Lagrangian w.r.t q_i	

Road Modelling Variables

λ_{br}	Bank angle for road segment	$[rad]$
λ_{gr}	Grade angle for road segment	$[rad]$
s_r	Longitudinal distance on road reference line	$[m]$
t_r	Lateral distance on road reference line	$[m]$
κ_r	Curvature of road segment	$[m^{-1}]$
c_r	Present road crown on road segment	$[Boolean]$
$\mathbf{s}_r$	Longitudinal distance vector	
$\mathbf{t}_r$	Lateral distance vector	
$\mathbf{c}_r$	Boolean crown vector	
$\mathbf{\Lambda}_{br}$	Road segment banking vector	
$\mathbf{\Lambda}_{gr}$	Road segment grade vector	
ds_r	Longitudinal resolution	
$\mathbf{s'}_r$	High resolution longitudinal distance vector	
κ'_r	High resolution curvature vector	
$\mathbf{\Lambda'}_{br}$	High resolution road segment banking vector	
$\mathbf{\Lambda'}_{gr}$	High resolution road segment grade vector	
$\mathbf{\Lambda'}_{zb}$	High resolution elevation profile, banking	
$\mathbf{\Lambda'}_{zg}$	High resolution elevation profile, grade	
$\mathbf{M}_{\Sigma}$	Cumulative sum matrix	
$\mathbf{\Lambda}_z$	Total elevation profile matrix	
$\mathbf{\Delta s'}_r$	Altered step length	

State-space Variables and Matrices

$\mathbf{x}_k$	State vector at timestep k
$\dot{\mathbf{x}}_k$	Time derivative of state vector at timestep k
$\mathbf{u}_k$	Input vector to state-space model at timestep k
$\mathbf{y}_k$	Output vector from state-space model at timestep k
$\mathbf{A}_c$	Continuous state-transition matrix
$\mathbf{B}_{\mathbf{u}c}$	Continuous input matrix

$\mathbf{B}_{\mathbf{r}c}$	Continuous road geometry input matrix
$\mathbf{C}_c$	Continuous output matrix
$\mathbf{D}_c$	Continuous input feedthrough matrix
$\mathbf{D}_{\mathbf{r}c}$	Continuous road geometry feedthrough matrix
$\mathbf{A}_d$	Discretized state-transition matrix
$\mathbf{B}_d$	Discretized input matrix
$\mathbf{B}_{\mathbf{u}d}$	Discretized road geometry state-transition matrix
$\mathbf{C}_d$	Discretized output matrix
$\mathbf{D}_d$	Discretized input feedthrough matrix
$\mathbf{D}_{\mathbf{r}d}$	Discretized road geometry feedthrough matrix
$\mathbf{x}_k$	Linearization / equilibrium point for states
$\mathbf{u}_0$	Linearization / equilibrium point for inputs
$\mathbf{r}_0$	Linearization / equilibrium point for road

Stochastic Variables in Predictive Modelling

$\mathbf{P}$	State estimate covariance
$\mathbf{Q}$	Process noise covariance
$\mathbf{R}$	Measurement noise covariance
$\mathbf{S}$	Innovation covariance
$\mathbf{K}$	Kalman Gain
$\mathbf{X}$	Stochastic state variable vector
$\bar{\mathbf{X}}$	Concatenated stochastic state variable vector
$\bar{\mathbf{A}}$	Concatenated state transition matrix for predictions
$\bar{\mathbf{C}}$	Concatenated output matrix for predictions
$\bar{\mathbf{P}}$	Concatenated state estimate covariance
$\bar{\mathbf{Q}}$	Concatenated process noise covariance
$\mathbf{F}$	Linearized state transition matrix for EKF
$\bar{\mathbf{F}}$	Concatenated state transition matrix for EKF
$\bar{\mathbf{H}}$	Concatenated output matrix for EKF
$\mathbf{P}_{ay}$	Lateral acceleration covariance
$\mathbf{A}_y$	Stochastic lateral acceleration variable

$\mathbf{A}_{ylim}$	Stochastic lateral acceleration limit variable	
H	Stochastic COM height variable	
$p_{rollover}$	Probability for rollover	
Δt	Sample time for EKF step	$[s]$
Δt_{pred}	Sample time for prediction step	$[s]$

Contents

List of Figures

List of Tables

1

Introduction

Articulated Heavy vehicles (AHVs) are an essential part of today's freight transports. Due to the high center of mass and low roll stability of AHVs, they are susceptible to the severe rollover accidents. These incidents pose significant safety concern due to their serious consequences, including fatalities, large damages, and long traffic disruptions. This thesis investigates how Predictive threat assessment (PTA) can be utilized to detect future potential rollover situations. We also propose a PTA method, how the road geometry can be utilized for motion prediction and to detect rollover risk.

1.1 Background

Rollovers occur with undesirable frequency in AHVs. They are not the most common type of accident, but are the most fatal one. Only in the U.S. alone, there is around 15,000 reported incidents of rollovers for commercial trucks each year. About 9,400 of these involve tractor-semitrailer combinations. While only 4.4% of tractor-semtrailer accidents are rollovers, 58% of all fatal injuries are caused by rollover [1]. On Swedish roads the number of incidents reaches almost two rollovers per day [2].

Certain places are more prone to incidents than others. Rollover accidents are especially common at roads with high curvature, such as sharp turns or highway entries and exits [3]. The road geometry, such as the bank angle and the slope also influences the rollover risk [3]. Roads are today designed according to local standards to ensure safe travels. Traditionally, Swedish road are designed according to Vägar och Gators Utformning (VGU) [4], and designed with 3 levels of banking, 2.5%, 4%, and 5.5%, depending on the radius and the rated speed of the road. Straights and large curves are designed with a crown for water to drain off, and have adverse banking of -2.5% [4, 5]. Other countries uses different standards, where most states in the U.S. allow up to 10% of banking [6]. Even though the roads should be designed according to the standards, in some cases the banking still is not sufficient to ensure good stability of the vehicles. Just in Sweden, 16000 state owned roads has been identified as unsafe and are extra prone to accidents such as rollover [7]. This suggests that preventive measures could potentially be more effective if they incorporate specific road characteristics into their threat assessment.

As of today, most modern vehicles are equipped with Advanced Driver Assistance Systems (ADAS), that aid the driver and prevent loss of control. Some solutions that is readily available in production vehicles, and prevent rollover, include Electronic Stability Control (ESC) and Roll Stability Control (RSC) systems. An evaluation of the effectiveness of ESC and RSC systems demonstrated that these control systems can reduce the incidence of rollovers by enhancing vehicle stability during critical driving conditions [8]. ESC is primarily designed to prevent unintended vehicle oversteer and understeer, thus it can prevent rollovers caused by external objects while going of the intended path [9]. RSC adds an additional roll sensor to the ESC hardware to detect when a vehicle has reached a critical roll angle and tries to slow down the vehicle [10]. However, as the ESC and RSC systems only are aware of the current state from sensors, there still occurs crashes that are not prevented when vehicle speed is to high and the steering to large. The control systems do not adequately account for rollovers caused by the road geometry, and the driver maneuvers to remain on the road. As such, these systems may not provide optimal safety measures in scenarios where road geometry plays a critical role for stability.

A critical consideration is whether an ADAS function can assess the risk of rollover while accounting for road geometry in a predictive context, i.e. perform a predictive threat assessment of the rollover risk. There are plenty of PTA methods today for assessing the risk of collision, staying within the lanes etc, but the material addressing rollovers is scarce. Most studies that address the risk of rollovers only considers a single vehicle unit [9, 11, 12], while only assessing the risk of rollovers in the current point of time, and not in the close future. If a vehicle travels on a straight road, these threat assessment methods could indicate that there is imminent threat, but in reality a sharp turn might be approaching where the vehicle does not have the necessary time to slow down. There exist few papers that propose a predictive method to asses the treat of rollovers for tractor-semitrailers combinations. [11] proposed a method to assess the rollover risk predicatively as well as a Model Predictive Controller (MPC) to prevent rollovers, based on vehicle to infrastructure information. However, only a single vehicle unit was considered and it was assumed that the steering request was known. In [13], an empirical model to predict the rollover risk, while travelling in a curve, was designed. Unfortunately it was also just developed for a single unit. Three studies have been found that assess the risk of rollover for articulated vehicles [14, 15, 16]. However none of them consider the geometry of the road and how that will impact the threat.

Threat assessment can, on a high level, be divided into two types, physical model-based methods, and data-driven methods. The physical models can be further divided into several categories, namely: Threat metrics, optimization methods, formal methods and probabilistic approaches [17]. Threat metrics utilizes a single behaviour to quantify the risk. Commonly used threat metrics for rollovers are: the lateral load transfer ratio (LTR), the roll angle, and the lateral acceleration of the vehicle [9]. Optimization methods and formal methods involve MPC and/or set-theory to quantify the threat, and has seen some promising results in predicting safe vehicle motion [18]. Probabilistic approaches are used mainly to leverage the systems uncertainties to make an assessment at a given level of confidence and make decisions thereafter [19]. The data driven approaches utilizes machine learning (ML) methods, to continuously learn from driver behaviour and model responsiveness to predict potential harm. Most threat assessment studies considering rollovers uses threat metrics and probabilistic approaches [9, 11, 12, 14, 15, 16, 20].

This thesis will specifically focus on assessing the risk of rollovers in multi-unit vehicle combinations, utilizing threat metrics and probabilistic frameworks. The approach is designed to account for system uncertainties and quantify the threat with a specified level of confidence. The thesis work is performed on behalf of Volvo Group Trucks Technology (VGTT) to further their advancements in the field of Autonomus driving (AD) and ADAS solutions.

1.2 Objective

The aim of this thesis is to develop and evaluate a predictive threat assessment method suited for early rollover risk detection for a tractor-semitrailer combination. This includes developing a vehicle dynamics model, a road model, and a predictive driver model - that can be used to predict the lateral acceleration of the two vehicle units. The developed PTA aims to detect a risk of a rollover in a future time horizon. The ultimate goal of the thesis is to develop a flexible, accurate and efficient threat assessment algorithm that has the potential to be implemented, real time, on many different combination vehicles. This means that the model needs to be capable of handling uncertainties such as measurement noise, state trajectory deviations and varying driver inputs.

Additionally, for the PTA to be effective, the computation time of the predictive algorithm needs to be sufficiently fast and the prediction horizon sufficiently long, ensuring that the driver, and/or an AD function has time to respond to a potential threat. The prediction will be done by considering information about the current and the future driving conditions. More specifically, the intended outcome is to obtain a PTA method that considers the road geometry, the vehicle state and the model uncertainties. The effectiveness of this approach will be validated through high fidelity simulations and against real vehicle data.

1.3 Limitations

The study is conducted over five months, and the following limitations has been done to constrain the scope of the thesis:

1. We will only detect potential rollovers, not actively try to prevent them.

2. We will only consider untripped rollovers caused by the geometry of the road.

3. We will assume that the driver aims to follow the road.

4. We will assume that the road geometry is constant over the entire vehicle unit and can be extracted if the position is known.

5. We will assume that all uncertainties can be expressed as Gaussian distributed variables.

1.4 Scientific questions

To conclude, the thesis aims to answer the following four questions:

1. What are the key variables to consider in a predictive threat assessment model, focused on rollover detection for multi-unit vehicles?

2. How can the geometry of the road effectively be integrated in a motion prediction and threat assessment algorithm?

3. Will the inclusion of the road in the model result in an improved threat assessment compared to its exclusion?

4. What are the uncertainties that influence the risk of rollover and how can they be accounted for by utilizing predictive threat assessment?

2

Threat definition

This chapter aims to provide an understanding of rollovers, their causes, and how basic road geometry affects rollover risk. It also examines the vehicle states and parameters that influence rollover risk and identifies associated uncertainties. The chapter concludes by defining the upper and lower limits for the rollover threshold, considering road geometry, and discussing the uncertainties in these limits.

2.1 Rollover threat definition

Rollovers in vehicles occur when the lateral acceleration exceeds a certain threshold, causing the vehicle to overturn and pivot around the outer wheels. This can happen during sharp turns, sudden maneuvers at high speeds or loss of control situations [1]. Another way to describe a rollover is through the application of D'Alembert's principle, where accelerations are represented as pseudo-forces which acts in the opposite direction to the acceleration. The sequence of events is illustrated in Figure 2.1. Rollovers are devided into two different categories; **tripped** rollovers and **untripped** rollovers.

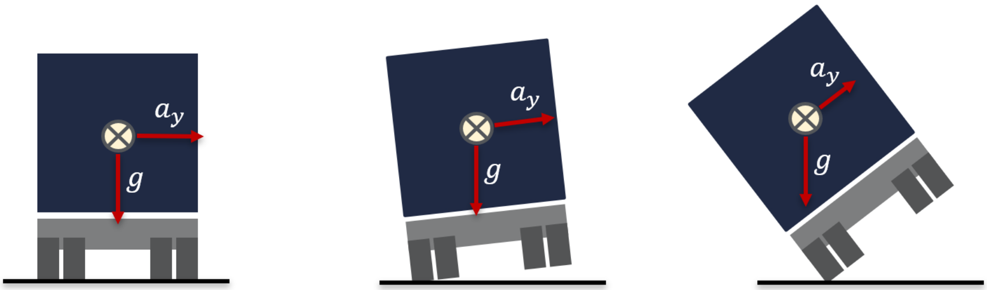

Figure 2.1: Rollover of vehicle as seen from behind. The vehicle is experiencing a lateral acceleration that makes the vehicle change its planar heading as it is performing a right turn. If the lateral acceleration is large enough, the vehicular body may initiate a rotation around the outer wheels, starting the sequence of events illustrated.

Tripped rollover: Are the end result from loss of control accidents, such as when the vehicle loses traction and slides into an external object such as a guardrail, or a curb, and where an external contact force is generated from the collision that trips the vehicle over. Tripped rollovers can also originate from uneven pavement that destabilize the vehicle, such as when the tyres hit a pot-hole, or if the vehicle goes off the road and the tyres dig into soft soil. A common element of tripped rollovers is their unpredictability, as they are caused by environmental factors that vary from situation to situation.

Untripped rollover: Are the result of high-speed maneuvers, sharp turns, or sudden steering inputs that cause the vehicle to lose balance. When the driver steers, the lateral force generated from the tyres is opposed by the centrifugal pseudo force in the vehicle body, that if large enough can overturn the vehicle. Unlike tripped rollovers, untripped rollovers are primarily caused by the dynamics of the vehicle and the driver behavior, making them more predictable.

This thesis exclusively investigates untripped rollovers. The reason for this is that they occur due to factors that are in some sense possible to account for in a PTA. A rollover will in this study be defined as a wheel contact loss with the road. A wheel lift does not necessarily cause a rollover but a rollover is always initiated with a wheel lift. Therefore, if a wheel lift effectively can be detected and prevented, rollovers also will be avoided.

2.2 Road properties that influence rollover risk

The main properties of the road that influence the rollover risk are the road geometry and the road pavement [12]. The road geometry consists of lateral and longitudinal slopes, and horizontal alignments, portrayed in Figure 2.2a, 2.2b, and 2.2c.

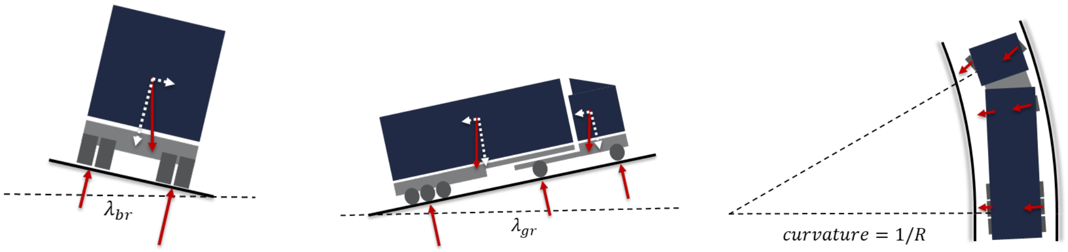

(a) Road banking **(b)** Road grade **(c)** Road curvature

Figure 2.2: Road Geometric Properties. (a) Road banking, (b) Road grade, (c) Road curvature.

The lateral slope, also called superelevation, cant or road banking generates additional lateral forces through the normal forces. If the banking is the same for all the wheels on a unit, the resulting force acting on the vehicle unit can be simplified to the lateral component of the gravitational force [21]. In a banked, curve the resulting force counteracts the centrifugal force generated by turning, reducing the risk of rollover. Banking also transfers load to the wheels that are placed at the lower side of the banking, which counteracts the risk of wheel lift. In the case of adverse superelevation, the rollover risk increases due to the resulting force added up to the centrifugal force, as well as transferring weigh from the inner to the outer wheels.

As a vehicle is traveling on an inclined road, also known as longitudinal slope and road grade, an additional longitudinal force will emerge which will decrease or increase the speed of the vehicle, depending on if it is an uphill or a downhill. An increase in longitudinal speed will make the vehicle more prone for rollovers. The road grade also shifts the weight longitudinally, which can cause instabilities and increased risk of wheel lift for wheels having the lower load.

The most significant road geometric property that impacts the lateral acceleration of a vehicle is the curvature. While the curvature itself does not directly generate lateral acceleration, if the driver wants to remain on the road, he or she needs to steer which generates lateral forces.

Two other properties of the road that affects rollover risk are the pavement friction coefficient, and smoothness [12]. However, in this study the only properties considered to vary with the road are the geometric properties, i.e., the bank, grade and curvature of the road. The friction coefficient is assumed to be high (= 1) since generally a higher friction increases the risk of rollover, and if a rollover can be avoided for the worst case scenario, it will arguably be avoided for the cases with lower friction as well. Rollover accidents due to a rough pavement is more closely related to tripped rollovers, which is outside the scope of the thesis.

2.3 Vehicle properties that influence rollover risk

However, the road is not the only factor that impact the rollover risk. The vehicle configuration and payload also impacts the stability. The main factors contributing to rollover risk is concluded in the following list:

- **Centre of mass height**: A higher center of mass (COM) makes the vehicle more prone to tipping. If the mass is distributed higher, it creates a longer lever for lateral centrifugal force to the ground. It also shifts the placement of the COM more during body roll.

- **Track width**: Large track width makes the vehicle more difficult to roll over by providing a wider base. Small track width increases rollover tendency.

- **Weight distribution**: Uneven payload shifts the center of mass off the longitudinal centerline. Increases rollover propensity in one direction compared to the other.

- **Compliant tires**: Tires that compress and strain shift the tire's contact patch, decreasing the lateral stability and making the vehicle more prone to tipping.

- **Compliant springs**: Springs allow vehicle body to squat, inducing body roll. Roll shifts COM laterally and increases the load on one side.

- **Compliant Body**: Rollovers most commonly initiate from the rear of the vehicle unit [1]. If the vehicle body is flexible a wheel lift of the rear is more easily induced.

- **Number of vehicle units**: A combination vehicle is less stable than a single unit vehicle due to compliant couplings and rearward amplification [22].

- **Vehicle speed**: Speed itself doesn't directly imply high lateral acceleration. However, the combination of speed and turning is the most significant reason for rollovers [9].

2.4 Defining lateral acceleration limit for rollover detection

In order to detect potential rollover situations, a lateral acceleration threshold that should not be exceeded needs to be defined. As already mentioned, we define rollovers as when a single wheel lifts from the ground. In other words, when any of the wheel vertical forces are equal to zero. However wheel lift is rather difficult to measure, and even harder to predict. Fortunately, wheel lift can also be estimated through lateral load transfer, arising from the lateral accelerations of the vehicle and banking of the road. Based on the load transfer ratio (LTR) on a rigid vehicle unit, we can derive a lateral acceleration limit starting from:

$$LTR = \frac{F_{zl} - F_{zr}}{F_{zl} + F_{zr}}, \qquad LTR \in [-1, 1] \tag{2.1}$$

Where the subscript l and r denotes left and right side respectively. Wheel lift happens when either $F_{zl} = 0$ or $F_{zr} = 0$ which gives a $LTR = \pm 1$. Next, the lateral load transfer for a rigid vehicle can be written as:

$$\Delta F_z = \frac{m a_y h}{w} \tag{2.2}$$

Where m is the mass of the vehicle, a_y is the lateral acceleration, h is the height of center of mass (COM), and w is the track width. The vertical wheel forces during operation can be estimated by the stationary forces and the load transfer:

$$F_{zl} = F_{z0l} + \Delta F_z \tag{2.3}$$

$$F_{zr} = F_{z0r} - \Delta F_z \tag{2.4}$$

If we assume that the static loads over the two sides of the vehicle are evenly distributed (COM is placed perfectly in the middle of the vehicle over the longitudinal axis), namely: $F_{z0l} = F_{z0r} = mg/2$, it is possible to rewrite the lateral load transfer ratio as:

$$LTR = \frac{2\Delta F_z}{mg} = \frac{2a_y h}{gw} \tag{2.5}$$

By considering the safe driving conditions when $-1 < LTR < 1$ we derive the limits for a rigid vehicle driving on a flat road.

$$-\frac{gw}{2h} < a_y < \frac{gw}{2h} \tag{2.6}$$

Now, if we instead consider the vehicle to travel on a banked road - we need to account for the additional acceleration generated by the vehicle tilting [21]. Therefore we get the new upper and lower bounds:

$$LTR = \frac{2h}{gw}\Big(a_y + g\sin(\lambda_b)\Big) \tag{2.7}$$

$$-\frac{gw}{2h} - g\sin(\lambda_b) < a_y < \frac{gw}{2h} - g\sin(\lambda_b) \tag{2.8}$$

Considering a non-rigid vehicle, accounting for the tire-, spring-, and body compliance, the acceleration limits needs to be lowered [1]. Depending on the vehicle configuration and that the lateral load transfer of the front and rear axles are almost independent due to the flexibility of the chassis, where the load transfer of the front axle could differ as much as $56\% - 70\%$ to the rear [23] the limit needs to be reduced even further. By introducing the compliance scaling factor α_{comp}, the final acceleration limit is then formulated as:

$$\alpha_{comp}\Big(-\frac{gw}{2h} - g\sin(\lambda_b)\Big) < a_y < \alpha_{comp}\Big(\frac{gw}{2h} - g\sin(\lambda_b)\Big) \tag{2.9}$$

Or expressed as individual upper and lower acceleration limits as:

$$a_{ylim,lower} = \alpha_{comp}\Big(-\frac{gw}{2h} - g\sin(\lambda_b)\Big) \tag{2.10}$$

$$a_{ylim,upper} = \alpha_{comp}\Big(\frac{gw}{2h} - g\sin(\lambda_b)\Big) \tag{2.11}$$

2.5 Uncertainties in acceleration limit

If all of the parameters for the vehicle and road are known, then a rather accurate estimate for the lateral acceleration limit can be made. However multiple, if not all, of these parameters are difficult to estimate. The most significant being the height of the COM. The height of the COM has arguably the largest influence over the lateral acceleration limit, meanwhile it is a parameter which is fairly difficult to estimate. The COM height also varies depending on the load of the truck. I.e., for one trip, the height may be vastly different compared to another trip.

Developing a method to obtain a good estimate of the COM height is outside the scope of this thesis. We will assume that the COM height is known - either as a constant, stochastic variable or continuously estimated by a method such as [24]. To cover a range of possible heights, we will model the COM height as a Gaussian variable, and approximate the corresponding uncertainty in acceleration limit by linearization. That is done in section 8.2.

The other factors, such as the compliance of the vehicle from the springs, tyres, body flexibility etc. are also difficult to estimate. As a more compliant system decreases the lateral acceleration limit, it is difficult to estimate using a static and/or dynamic rollover limit. In this thesis we introduced the compliance factor α_{comp} which acts as a tuning parameter. This tuning parameter is highly dependent on the vehicle configuration and could also differ between vehicle units. The tuning parameter can also be used as a safety margin, ensuring an additional layer of protection against the threat of an impeding rollover.

3

Vehicle Dynamics

This chapter delves into the vehicle dynamics and the derivation of the equations of motion (EOM). The chapter firstly clarifies the coordinate systems and the tyre model used. The derivation of the multi-unit vehicle model follows a Lagrangian approach. The vehicle model described in this chapter is largely inspired from a nonlinear model used to simulate the state trajectories of multi-trailer combinations [25].

3.1 Coordinate systems

In order to formulate the dynamics that are present in the vehicle, one needs to consider the multiple coordinate systems present. This is vital in order to translate the forces acting on the individual bodies to the desired reference frame. In this thesis we use coordinate system in accordance with ISO-8855 [26]. An overview is given in Figure 3.1.

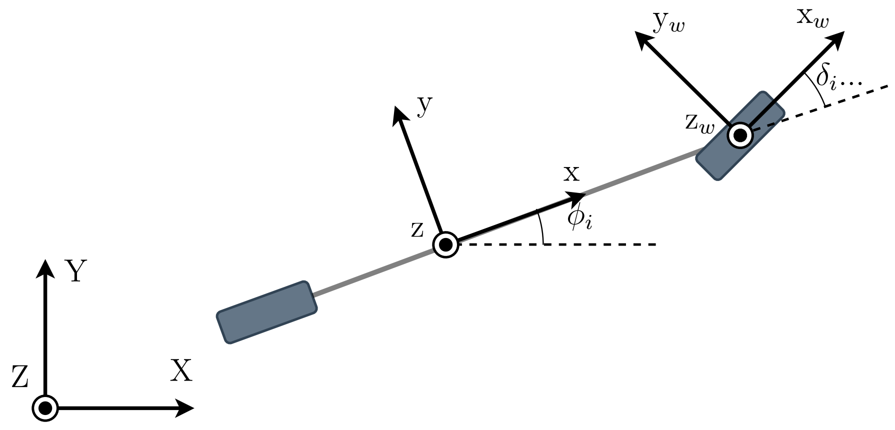

Figure 3.1: Visualization of the three coordinate systems present in a One-Track, One-Unit Model. The coordinate system in the external reference frame is the World Coordinate System (X, Y, Z), the coordinate system located in the vehicle COM is the Vehicle Coordinate System (x, y, z) and the coordinate system located in the wheel is the Tire Coordinate System (x_w, y_w, z_w).

World Coordinate System (WCS):

- The world coordinate system (WCS) is an external reference frame used to describe the motion of the vehicle in its environment.
- The X-axis points to the east (increasing longitude).
- The Y-axis points to the north (increasing latitude).
- The Z-axis points upwards perpendicular to the Earth's surface (increasing altitude).

Vehicle Coordinate System (VCS):

- The origin of the vehicle coordinate system (VCS) is located at the vehicle's center of mass (COM).
- The x-axis is aligned with the longitudinal axis of the vehicle body, pointing forward.
- The y-axis is aligned with the lateral axis of the vehicle, pointing to the left side.
- The z-axis is aligned with the vertical axis, pointing upward.

Tire Coordinate System (TCS):

- The tire coordinate system (TCS) is aligned with the plane of the tire contact patch.
- The x_w-axis points in the direction of the tire's longitudinal axis.
- The y_w-axis points in the direction of the tire's lateral axis, to the left side.
- The z_w-axis points outward from the tire surface, perpendicular to the contact patch, upwards.

In multi-unit vehicle configurations, individual VCS are defined for each unit while maintaining a single fixed WCS as the external reference frame.

Now, to transform forces, distances, velocities, or other spatial/directional states, one must employ rotation matrices. These matrices enable the rotation of spatial entities according to the rotation matrix M:

$$M_B^A(\alpha) = \begin{bmatrix} \cos(\alpha) & -\sin(\alpha) \\ \sin(\alpha) & \cos(\alpha) \end{bmatrix} \tag{3.1}$$

$$M_B^{A^{-1}}(\alpha) = \begin{bmatrix} \cos(\alpha) & \sin(\alpha) \\ -\sin(\alpha) & \cos(\alpha) \end{bmatrix} \tag{3.2}$$

Here, the arbitrary variable α represents the angle of rotation from the coordinate system A to the coordiate system B. These rotations are extensively utilized throughout the thesis. We will use notation such as M_{WCS}^{VCS} for rotation from VCS to WCS, M_{VCS}^{TCS} for rotation from TCS to VCS etc.

3.2 Tyre model

Tire models are a crucial and well studied part of vehicle dynamics as the forces generated by the tires on the road are what propagates the system forward. There are multiple tire-models that uses different parameters and variables to compute the generated forces, such as linear models, Brush models, Pacejka magic formula etc [27]. In this thesis, we will use a linear tire model since rollovers in AHVs can occur at small slip angles and relatively low lateral forces, making this approach sufficient. A comparison between a linear and nonlinear model can be seen in Figure 3.2. At large slip angles, this model tends to overestimate the lateral force generated from turning. As a result the model will predict that a rollover is more likely to happen. However, at those higher slip angles a rollover is likely to occur even for the more accurate nonlinear model, as it does not take much force to overturn an AHV.

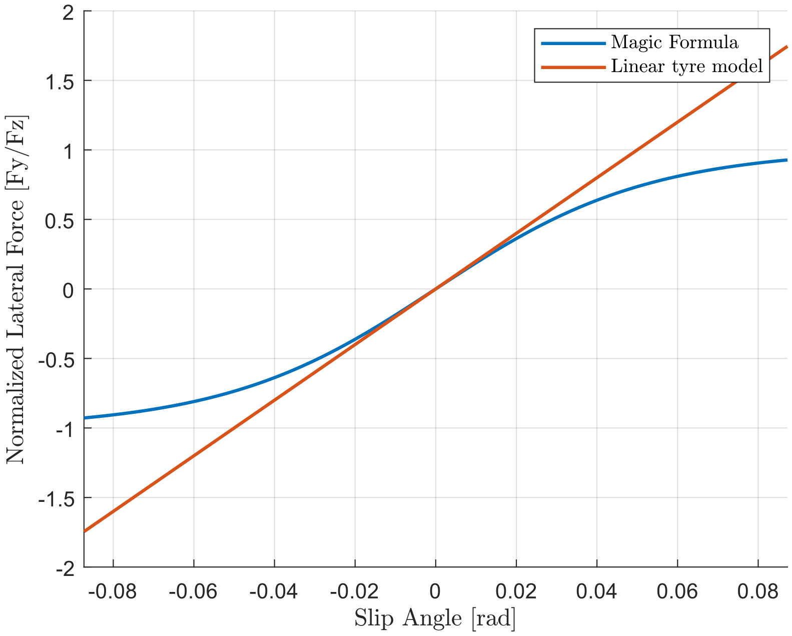

Figure 3.2: Comparison of the Lateral forces estimated from a Linear and nonlinear tyre model.

A close up of the front tire in a one-track model is shown in Figure 3.3. The actual direction of travel of the wheel can expressed as factors of $v_{xw,ij}$ $v_{yw,ij}$ in the TCS. The tire is pointing δ_{ij} radians relative to the VCS. The angle between the wheels direction of travel and direction of pointing is creating the slip angle α. The slip angle generates the lateral force $F_{yw,ij}$ which is also expressed in TCS. The longitudinal wheel force $F_{xw,ij}$ is generated from the axle torque from propulsion or braking.

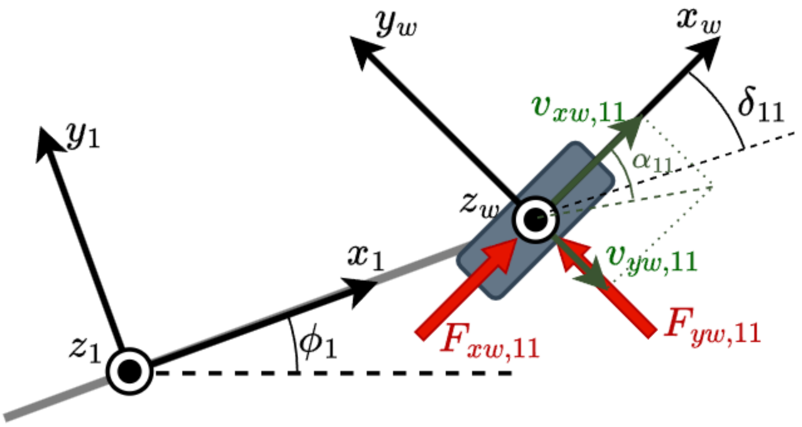

Figure 3.3: Close up of a steered tire in a one-track unit. Illustration of the velocities, forces, slip angles and how they are aligned with TCS and VCS.

Moreover, if we assume that the vehicle is operating at small slip angles the relation between slip angle and generated lateral force can be described linearly. The lateral force for the turning wheel can be computed as:

$$F_{yw,ij} = -C_{y,ij} s_{y,ij} \tag{3.3}$$

$$s_{y,ij} = \tan(\alpha_i) \tag{3.4}$$

Where $C_{y,ij}$ is the tire cornering stiffness, and $s_{y,ij}$ is the lateral slip of the wheel. If the conditions for pure lateral slip is met, one simple way to estimate the cornering stiffness is to assume that it is proportional to the wheel vertical force, which only leaves us to find the lateral slip stiffness coefficient CC_y [27]:

$$C_{y,ij} = CC_y F_{zw,ij}. \tag{3.5}$$

The lateral slip can also be expressed as the fraction between the tire lateral velocity and longitudinal velocity:

$$s_{y,ij} = \frac{v_{yw,ij}}{\mid v_{xw,ij} \mid} \tag{3.6}$$

In Equation (3.6) it is apparent that the model will not be valid when $v_{xw,ij} \neq 0$. In the essence of expressing the velocities in the WCS, we can perform the rotation from TCS to WCS by two consecutive rotations:

$$\begin{bmatrix} \dot{X}_{w,ij} \\ \dot{Y}_{w,ij} \end{bmatrix} = M_{WCS}^{VCS}(\phi_i) M_{VCS}^{TCS}(\delta_i) \begin{bmatrix} v_{xw,ij} \\ v_{yw,ij} \end{bmatrix} \tag{3.7}$$

$$\begin{bmatrix} v_{xw,ij} \\ v_{yw,ij} \end{bmatrix} = M_{VCS}^{TCS-1}(\delta_i) M_{WCS}^{VCS-1}(\phi_i) \begin{bmatrix} \dot{X}_{w,ij} \\ \dot{Y}_{w,ij} \end{bmatrix} \tag{3.8}$$

After this, the wheel velocities expressed in WCS can be expressed in terms of the vehicle position X, Y, which is important in the next section 3.3 for deriving the vehicle dynamics model.

3.3 Derivation of multi-unit vehicle model

The following section describes the derivation of the vehicle model used for the motion prediction. The derivation of the model follows a Lagrangian approach [28], and is applicable for any vehicle combination. This thesis will however be limited to only analyze two unit combinations. To reduce the complexity of the model, it was decided to model the vehicle as a one-track model, meaning all the wheels on each axle was lumped together at the axle center. The one-track two-unit model is illustrated in Figure 3.4 below.

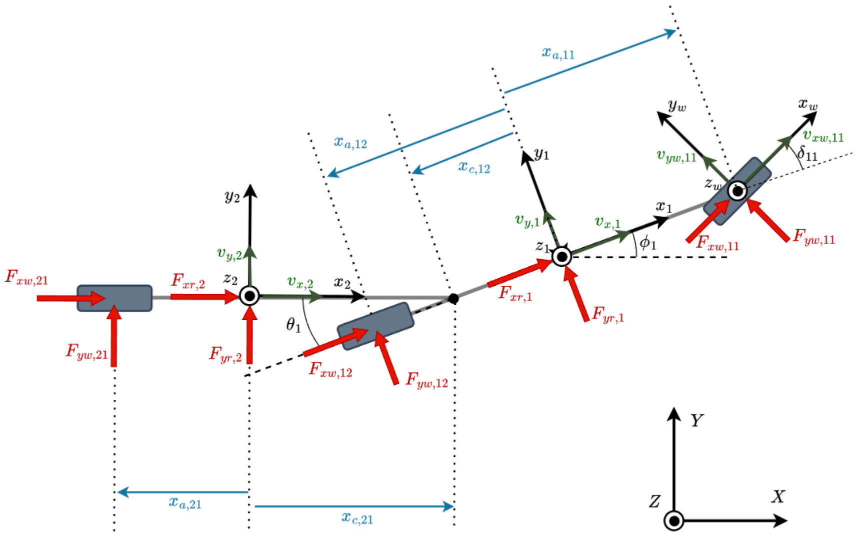

Figure 3.4: Visualization of a One-Track Two-Unit Model. The model is situated in the external coordinate frame WCS.

The derivation of the model is done in five steps: Defining the generalized coordinates, computing the internal energy of the system, deriving the generalized forces applied to the system, transforming the model to the VCS, and finally merge them in the Euler-Lagrange equation to obtain the equations of motion (EOM).

We start with defining the generalized coordinates. For the general case, with any number of vehicle units, the generalized coordinates and their respective time derivatives are chosen as:

$$\mathbf{q} = \begin{bmatrix} X_1 \\ Y_1 \\ \phi_1 \\ \theta_i \\ \theta_{i+1} \\ \vdots \\ \theta_{n_u-1} \end{bmatrix}, \quad \dot{\mathbf{q}} = \begin{bmatrix} \dot{X}_1 \\ \dot{Y}_1 \\ \dot{\phi}_1 \\ \dot{\theta}_i \\ \dot{\theta}_{i+1} \\ \vdots \\ \dot{\theta}_{n_u-1} \end{bmatrix}$$

Where X_1, and Y_1 are the global position of the first unit, ϕ_1 is the yaw of the first unit and θ_i is the articulation angle between unit $i+1$ and i. n_u is the number of units in the configuration. For a tractor-semitrailer combination we have $n_u = 2$.

Now we compute the internal energy of the dynamical system. The kinetic energy of the entire system is the sum of the kinetic energy for each vehicle unit. The potential energy is assumed to be 0 since the model has no translational motion along the vertical Z-axis. The energies are obtained as:

$$T(\mathbf{q}, \dot{\mathbf{q}}) = \frac{1}{2} \sum_{i=1}^{n_u} m_i \left(\dot{X}_i^2 + \dot{Y}_i^2 \right) + I_{zz,i} \dot{\phi}_i^2 \tag{3.9}$$

$$V(\mathbf{q}) = 0 \tag{3.10}$$

Moreover, the yaw and the yaw rate of each trailing unit is computed according to the ISO8855 standard [26] as:

$$\phi_i = \phi_{i-1} - \theta_{i-1}, \tag{3.11}$$

$$\dot{\phi}_i = \dot{\phi}_{i-1} - \dot{\theta}_{i-1}, \tag{3.12}$$

The positions of COM for each unit can be derived from the first unit and the coupling positions as:

$$\begin{bmatrix} X_i \\ Y_i \end{bmatrix} = \begin{bmatrix} X_{i-1} \\ Y_{i-1} \end{bmatrix} + \begin{bmatrix} x_{c(i-1)2} \cos(\phi_{i-1}) - x_{ci1} \cos(\phi_i) \\ x_{c(i-1)2} \sin(\phi_{i-1}) - x_{ci1} \sin(\phi_i) \end{bmatrix}, \quad i = 2, ..., n_u \tag{3.13}$$

Where $x_{c(i-1)1}$ is the length from the COM of the leading unit to the coupling point, and x_{ci1} is the distance from the COM of the trailing unit to the coupling point. The global velocities of each unit can be derived by time differentiation of their positions:

$$\begin{bmatrix} \dot{X}_i \\ \dot{Y}_i \end{bmatrix} = \begin{bmatrix} \dot{X}_{i-1} \\ \dot{Y}_{i-1} \end{bmatrix} + \begin{bmatrix} -x_{c(i-1)2} \sin(\phi_{i-1})\dot{\phi}_{i-1} + x_{ci1} \sin(\phi_i)\dot{\phi}_i \\ x_{c(i-1)2} \cos(\phi_{i-1})\dot{\phi}_{i-1} - x_{ci1} \cos(\phi_i)\dot{\phi}_i \end{bmatrix}, \quad i = 2, ..., n_u \tag{3.14}$$

Similarly, the position of the wheels of each axle j can be expressed in the WCS as:

$$\begin{bmatrix} X_{w,ij} \\ Y_{w,ij} \end{bmatrix} = \begin{bmatrix} X_i \\ Y_i \end{bmatrix} + M_{WCS}^{VCS}(\phi_i) \begin{bmatrix} x_{a,ij} \\ 0 \end{bmatrix} \tag{3.15}$$

Where $x_{a,ij}$ is the length from the unit COM to the axle where the wheel is attached. We can now obtain the Lagrangian for the configuration of n_u units as:

$$\mathcal{L}(\mathbf{q}, \dot{\mathbf{q}}) = T(\mathbf{q}, \dot{\mathbf{q}}) - V(\mathbf{q}) \tag{3.16}$$

$$\mathcal{L}(\mathbf{q}, \dot{\mathbf{q}}) = \sum_{i=1}^{n_u} \frac{1}{2} m_i \Big(\dot{X}_i^2 + \dot{Y}_i^2 \Big) + \frac{1}{2} I_{zz,i} \dot{\phi}_i^2 \tag{3.17}$$

Continuing the model derivation, we now have to consider how the external forces act on the system, i.e. we need to define the generalized forces $\mathbf{Q}$. We do so by determining the components of

$$\mathbf{Q} = \begin{bmatrix} Q_{X_1} \\ Q_{Y_1} \\ Q_{\phi_1} \\ Q_{\theta_i} \\ Q_{\theta_{i+1}} \\ \vdots \\ Q_{\theta_{n_u - 1}} \end{bmatrix} \tag{3.18}$$

The generalized forces $\mathbf{Q}$ have to be expressed in the same coordinate system as the generalized coordinates $\mathbf{q}$, i.e. the WCS, and can be formulated through the forces acting on the system and their point of action according to:

$$\mathbf{Q} = \sum_{i=1}^{n_f} \frac{\partial \mathbf{p}_i^\top}{\partial \mathbf{q}} \mathbf{F}_i \tag{3.19}$$

The forces acting on the system consist of the lateral and longitudinal tyre forces, originating from the steering and vehicle acceleration. And, the body forces acting on the COM of each unit arising from the grade and banking of the road, explained further in section 4.5.

Equations (3.9 - 3.19) are sufficient to formulate the Euler-Lagrange equation describing the dynamics of the system in the global frame of reference WCS:

$$\frac{d}{dt}\frac{\partial \mathcal{L}}{\partial \dot{\mathbf{q}}} - \frac{\partial \mathcal{L}}{\partial \mathbf{q}} = \mathbf{Q} \tag{3.20}$$

However, in vehicle dynamics, it is often more convenient to express the dynamics in terms of variables in the inertial reference frame (VCS) rather than the external coordinate system (WCS). This is because control input signals and vehicle state measurements are typically expressed in the VCS frame of reference. As a result, we aim to express the Euler-Lagrange Equation (3.20) in terms of v_{x1}, v_{y1}, and local wheel forces F_w instead of global forces. Utilizing the Pythagorean identity, the Lagrangian function (3.17) can thus be expressed in terms of local velocities as follows:

$$\mathcal{L}(v_{x1}, v_{y1}, \dot{\phi_1}) = \frac{1}{2} m_1 \Big(v_{x1}^2 + v_{y1}^2 \Big) + \frac{1}{2} I_{zz,1} \dot{\phi_1}^2, \tag{3.21}$$

To go from the velocities in WCS to VCS, a rotation is applied:

$$\begin{bmatrix} v_{x1} \\ v_{y1} \end{bmatrix} = M_{VCS}^{WCS}(\phi_1) \begin{bmatrix} \dot{X}_1 \\ \dot{Y}_1 \end{bmatrix}, \tag{3.22}$$

This means that $v_{x,1}$ and $v_{y,1}$ will be expressed as functions of $\dot{X}_1, \dot{Y}_1$ and ϕ_1. Therefore chain rule differentiation needs to be performed on the Euler-Lagrange expression:

$$\frac{\partial \mathcal{L}}{\partial \dot{X}_1} = \frac{\partial \mathcal{L}}{\partial v_{x1}} \frac{\partial v_{x1}}{\partial \dot{X}_1} + \frac{\partial \mathcal{L}}{\partial v_{y1}} \frac{\partial v_{y1}}{\partial \dot{X}_1} = \frac{\partial \mathcal{L}}{\partial v_{x1}} \cos(\phi_1) - \frac{\partial \mathcal{L}}{\partial v_{y1}} \sin(\phi_1) \tag{3.23}$$

$$\frac{\partial \mathcal{L}}{\partial \dot{Y}_1} = \frac{\partial \mathcal{L}}{\partial v_{x1}} \frac{\partial v_{x1}}{\partial \dot{Y}_1} + \frac{\partial \mathcal{L}}{\partial v_{y1}} \frac{\partial v_{y1}}{\partial \dot{Y}_1} = \frac{\partial \mathcal{L}}{\partial v_{x1}} \sin(\phi_1) + \frac{\partial \mathcal{L}}{\partial v_{y1}} \cos(\phi_1) \tag{3.24}$$

$$\frac{\partial \mathcal{L}}{\partial \phi_1} = \frac{\partial \mathcal{L}}{\partial v_{x1}} \frac{\partial v_{x1}}{\partial \phi_1} + \frac{\partial \mathcal{L}}{\partial v_{y1}} \frac{\partial v_{y1}}{\partial \phi_1} = \underbrace{\frac{\partial \mathcal{L}}{\partial v_{x1}}}_{A} v_{y1} - \underbrace{\frac{\partial \mathcal{L}}{\partial v_{y1}}}_{B} v_{x1}, \tag{3.25}$$

The rest of the terms in the Lagrangian remains the same, since the yaw and articulation angles are independent of the frame of reference.

To simplify the expressions, the partial derivatives are substituted with A and B. The time derivatives of Equations (3.23 - 3.24) can then be derived by the product rule:

$$\frac{d}{dt}\frac{\mathcal{L}}{\dot{X}_1} = -A\sin(\phi_1)\dot{\phi}_1 + \dot{A}\cos(\phi_1) - B\cos(\phi_1)\dot{\phi}_1 - \dot{B}\sin(\phi_1) \tag{3.26}$$

$$\frac{d}{dt}\frac{\mathcal{L}}{\dot{Y}_1} = A\cos(\phi_1)\dot{\phi}_1 + \dot{A}\sin(\phi_1) - B\sin(\phi_1)\dot{\phi}_1 + \dot{B}\cos(\phi_1) \tag{3.27}$$

Or in VCS, given the rotation $M_{VCS}^{WCS}(\phi_1)$, it can simply be expressed as:

$$\frac{d}{dt}\frac{\mathcal{L}}{v_{x1}} = \dot{A} - B\dot{\phi}_1 \tag{3.28}$$

$$\frac{d}{dt}\frac{\mathcal{L}}{v_{y1}} = \dot{B} + A\dot{\phi}_1 \tag{3.29}$$

At this point, we have expressed the LHS of the Euler-Lagrange equation in terms of variables in the vehicle unit. Now, we need to do the same for the RHS i.e. the generalized forces $\mathbf{Q}$ are expressed as:

$$\mathbf{Q}_{VCS} = \begin{bmatrix} Q_{x1} \\ Q_{y1} \\ Q_{\phi_1} \\ Q_{\theta_i} \end{bmatrix} = \begin{bmatrix} M_{VCS}^{WCS}(\phi_1) & \mathbf{0}_{2\times n_u} \\ \mathbf{0}_{n_u\times 2} & \mathbf{I}_{n_u\times n_u} \end{bmatrix} \begin{bmatrix} Q_{X_1} \\ Q_{Y_1} \\ Q_{\phi_1} \\ Q_{\theta_i} \end{bmatrix} \tag{3.30}$$

And finally, if we define the state vector as $\mathbf{x} = [v_{x1}, v_{y1}, \phi_1, \dot{\phi}_1, \theta_i, \dot{\theta}_i]^\top$, the input vector as $\mathbf{u} = [\delta_{11}, F_{xw,ij}]^\top$, and the road properties of each unit as $\mathbf{r} = [\lambda_{b,i}, \lambda_{g,i}]^\top$, we obtain the implicit EOM:

$$F(\mathbf{x}, \dot{\mathbf{x}}, \mathbf{u}, \mathbf{r}) = 0 = \begin{cases} \frac{d}{dt}\frac{\partial\mathcal{L}}{\partial v_{x1}} - Q_{x1} \\ \frac{d}{dt}\frac{\partial\mathcal{L}}{\partial v_{y1}} - Q_{y1} \\ \frac{d}{dt}\frac{\partial\mathcal{L}}{\partial\dot{\phi}_1} - \frac{\partial\mathcal{L}}{\partial\phi_1} - Q_{\phi_1} \\ \frac{d}{dt}\frac{\partial\mathcal{L}}{\partial\dot{\theta}_i} - \frac{\partial\mathcal{L}}{\partial\theta_i} - Q_{\theta_i} \end{cases} \tag{3.31}$$

4

Road Modelling

This chapter covers common geometric design of roads, and presents current methods to estimate road geometry, namely the use of high definition maps. The chapter continues by explaining how a road surface can be constructed from its geometric properties. It finishes by explaining how the road model is integrated into the vehicle dynamics model.

4.1 Road geometric design

The geometric design of roads can mainly be represented by horizontal alignments, longitudinal slopes, superelevation and road crowns [3, 4]. The horizontal alignments consists of straights, transition curves and circular curves, depicted in Figure 8.3a. The longitudinal slope, or road grade, consists of even sections and transitions, shown in Figure 4.1b. In order to mitigate parts of the centrifugal force generated while turning, roads surfaces are often designed with a one-way lateral cross slope, depicted in Figure 4.1c. Straights are often designed with a crown in the center and lateral slope on either side in order to facilitate water drainage, as shown in Figure 8.3b. For vehicle stability reasons, transition of banking is designed by rotation around the inside of the road curve [4]. Figure 4.2, portrays two ways of how transition of banking should be designed for two way traffic to the left, and one way traffic to the right.

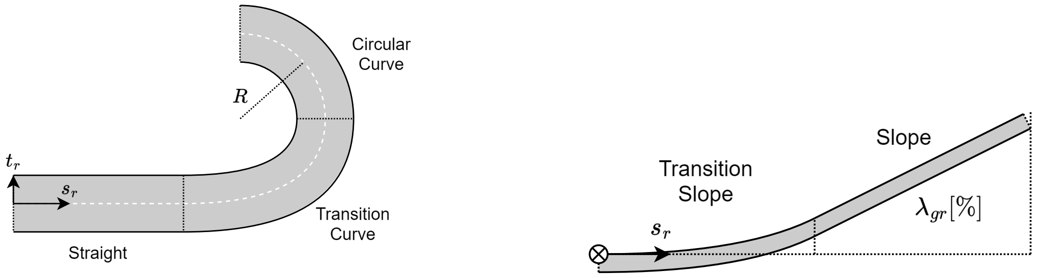

(a) Horizontal alignments.

(b) Road grade.

(c) Superelevation banking.

(d) Road crown banking.

Figure 4.1: Road geometric design. (a) depicts horizontal alignments, (b) road grade, (c) superelevation curves, and (d) road crown.

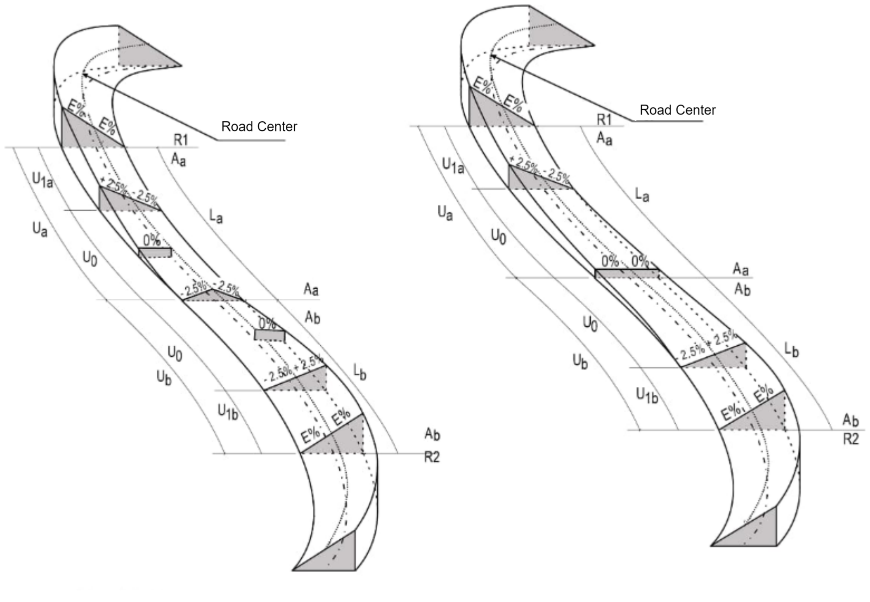

Figure 4.2: Transition of banking, according to VGU. Left figure is for two-way traffic, and right figure for one-way traffic. *Reworked from* [4].

In this thesis both the cross slope from superelevation and road crown will be considered equally and will here on be referred to as the road banking. Positive bank angle is defined as being positive uphill at the left side in the traveling direction. Road grade is defined as being positive uphill in the travelling direction. Both road grade and banking is most commonly expressed as percentages, i.e., it is the ratio of rise over run.

4.2 Available methods to estimate road geometry

As of today, several different approaches exist for estimating road geometry. However, the approaches can mainly be split into two groups: road geometry estimation by perception sensors, such as lidar/radar/stereo camera [29, 30] and road geometry estimation by localization and high definition (HD) maps [31]. The former alternative however requires a separate method to firstly record and generate the map, for instance by driving with an inertial profiler, or by perception sensors. We will not go further into the available methods for road estimation in this thesis and instead assume that the road properties are available from a HD map, and that an accurate localization algorithm exist.

4.3 High definition maps

In contrast to regular maps, which mostly contain information about the road network, street names and speed limits useful for route planning, HD maps contain more detailed information necessary for most AD/ADAS applications, where high precision localization is of importance [31]. Some of the current providers of HD Maps for such applications are HERE technologies, TOMTOM, Baidu Apollo, and Civil Maps [31].

Even though the architecture of HD maps is not standardized, most are designed similarly, consisting of layers that include road networks, lanes, and various features such as traffic signs, road barriers, and landmarks [31]. These layers are suitable for different types of applications, such as route planning, motion control and localization. Figure 4.3 illustrates the architecture of HERE Technology's HD map [32], which is currently used in ADAS applications within Volvo Trucks. As can be seen in the Figure, the map consists of three layers: the road model, the lane model, and the localization model. The first layer portrays the road topology, i.e the location of intersections and the geometry of the roads. The road geometry is described by a road centerline including the heading, curvature and road gradient. The second layer describes the geometry of the lanes, including the number of lanes, their borders and width. And the last layer contains additional objects and features useful for localization. As seen in the HD map from HERE technologies, most of the road properties of interest for our model can be found in the first layer of the map. The banking is not available as as standard feature in the first layer and would have to be derived from the 3D-lane model.

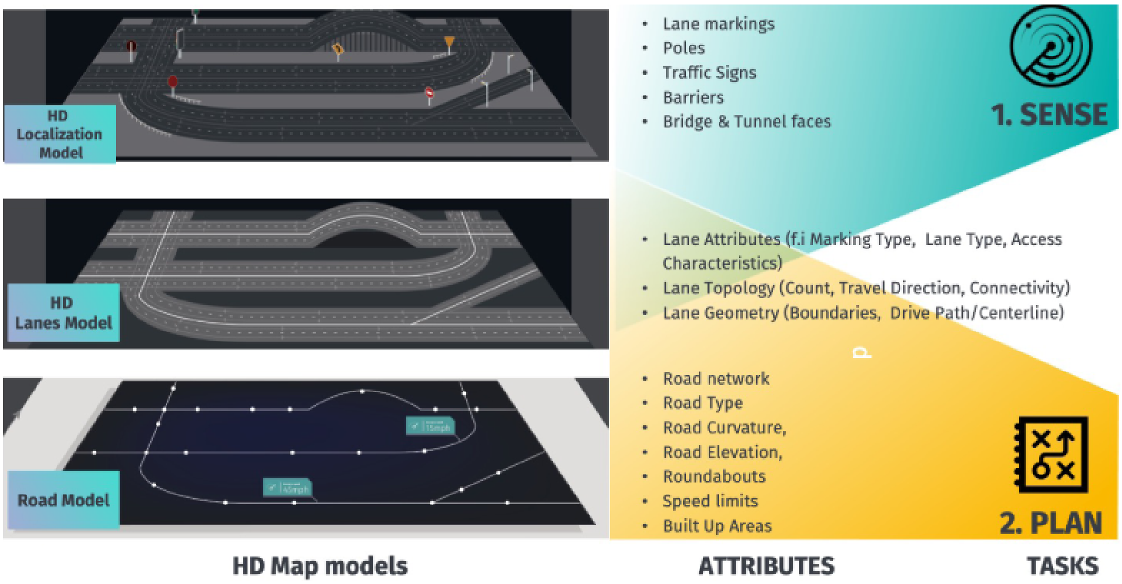

Figure 4.3: Representation of HERE technology's HD Map architecture. *Reworked from* [32].

As it is challenging to import a HD map into the simulation environment, we have developed our own efficient way to construct and represent a road to be integrated with the vehicle model. We have based the design of the road on the properties from HD maps, and the design standards from VGU [4], to closely simulate how it would be represented in a real-world scenario.

4.4 Constructing a road surface from properties

Similar to the map from HERE technology [32], our road is based on a reference line defined by the distance travelled s_r, curvature κ_r, road grade λ_{g_r}, and additionally the banking λ_{b_r}. To convert from the reference line to global coordinates, the start location and heading of the road must be specified. We assume all roads start at the origin, i.e., $X = Y = \phi_r = 0$. The road consists of several sections defined by their starting point and endpoints and the properties at those locations. Linear interpolation is used to create smooth transitions over the section.

To define the road surface geometry, the road width and presence of a crown c_r, must be specified. The road crown is represented as a boolean variable, typically true in straight sections and false in curves. The road width is discretized into fixed distances from the center, denoted t_r, where $t_r < 0$ indicates the right side of the road. The road surface is described by a grid pattern using the center line as a reference. Road grade and banking are represented by matrices $\mathbf{\Lambda}_{g_r}$ and $\mathbf{\Lambda}_{b_r}$, where each column describes the properties at a distinct offset from the center line. The construction of the road profile involves seven steps:

1. Firstly, the distance vectors $\mathbf{s}_r$, $\mathbf{t}_r$, the crown vector $\mathbf{c}_r$ and the corresponding road property vectors $\kappa_r, \lambda_{b_r}, \lambda_{g_r}$, needs to be defined. An example road consisting of a 50-meter straight section with a constant 1% slope and a 2.5% crowned banking, transitioning over 25 meters into a 50-meter left turn with a 50-meter radius and -5% banking would be defined by:

$$\begin{aligned}
\mathbf{s}_r &= [0, 50, 75, 125]^\top \\
\kappa_r &= [0, 0, 1/50, 1/50]^\top \\
\mathbf{c}_r &= [1, 1, 0, 0]^\top \\
\lambda_{b_r} &= [0.025, 0.025, -0.05, -0.05]^\top \\
\lambda_{g_r} &= [0.01, 0.01, 0, 0]^\top
\end{aligned}$$

2. The next step is to assume constant banking and grade over the entire road width. This is achieved by repeating the banking and grade vectors based on the discretized width. If the road width is 6.5 m, and it has ben discretized into $n_{t_r} = 5$ elements, it gives $t_r = [-3.25, -1.625, 0, 1.625, 3.25]$. This means the road banking and grade vector will be repeated five times to build up surface grids:

$$\begin{aligned}
\mathbf{\Lambda}_{b_r} &= [\lambda_{b_r}, \lambda_{b_r}, \lambda_{b_r}, \lambda_{b_r}, \lambda_{b_r}] \\
\mathbf{\Lambda}_{g_r} &= [\lambda_{g_r}, \lambda_{g_r}, \lambda_{g_r}, \lambda_{g_r}, \lambda_{g_r}]
\end{aligned}$$

3. If the road contains a crown the banking needs to be reversed in the opposing lane where $t_r > 0$. For the example road with $\mathbf{c}_r = [1, 1, 0, 0]$ and $t_r = [-3.25, -1.625, 0, 1.625, 3.25]$ the elements in the last two columns, first and second row switch sign:

$$\mathbf{\Lambda}_{b_r} = \begin{bmatrix} 0.025 & 0.025 & 0.025 & -0.025 & -0.025 \\ 0.025 & 0.025 & 0.025 & -0.025 & -0.025 \\ -0.05 & -0.05 & -0.05 & -0.05 & -0.05 \\ -0.05 & -0.05 & -0.05 & -0.05 & -0.05 \end{bmatrix}$$

4. The subsequent step is to refine the resolution of both the travelled distance and the corresponding properties. This is achieved by linear interpolation and is necessary to achieve smooth transitions. The resolution, i.e. the sample length, is denoted ds_r and new variables with increased resolution are marked by an apostrophe, e.g., $\mathbf{s}'_r$, κ'_r, $\mathbf{\Lambda}'_{b_r}$, $\mathbf{\Lambda}'_{b_r}$. If the example road, is discretized into 1m intervals, $ds_r = 1$, the newly created grid arrays will contain $n_{s'_r} = 126$ rows.

5. The surface grids with higher resolution are then used to compute the elevation profile of the road. Starting with the banking, the road centerline, $t_r = 0$ is initially used as reference $z_r = 0$. The elevation is then computed by elementwise multiplication of the rows in $\mathbf{\Lambda}'_{b_r}$ and the width $\mathbf{t}_r$. However, since the roads are designed to alter the elevation from the inner curve, the reference height is shifted to the lowest side by subtracting the minimum elevation of each row.

   $$\mathbf{\Lambda}'_{z_b} = \mathbf{\Lambda}'_{b_r} \odot \mathbf{t}_r - \min(\mathbf{\Lambda}'_{b_r} \odot \mathbf{t}_r) \tag{4.1}$$

   For the road grade, the beginning of the road section $s'_r = 0$ is used as reference height. The elevation is then computed by the cumulative sum of the road grade, multiplied by the resolution ds_r:

   $$\mathbf{\Lambda}'_{z_g} = \mathbf{M}_\Sigma \mathbf{\Lambda}'_{g_r} ds, \tag{4.2}$$

   $$\mathbf{M}_\Sigma = \begin{bmatrix} 1 & 0 & 0 & \dots & 0 & 0 \\ 1 & 1 & 0 & \dots & 0 & 0 \\ 1 & 1 & 1 & \dots & 0 & 0 \\ \vdots & \vdots & \vdots & \ddots & \vdots & \vdots \\ 1 & 1 & 1 & \dots & 1 & 0 \\ 1 & 1 & 1 & \dots & 1 & 1 \end{bmatrix}$$

   The total elevation profile is then given by the sum of the two elevation profiles:

   $$\mathbf{\Lambda}_z = \mathbf{\Lambda}_{z_b} + \mathbf{\Lambda}_{z_g} \tag{4.3}$$

6. To compute the combined road grade, we also need to consider that the distance is shorter in the inside of the curves. An intuitive example of this is how a spiral staircase is steeper near the center than at the outer edge. Using the formula for arc length as a starting point: $s_{arc} = R\alpha$, where α is an arbitrary angle that subtends at the circle's center, it is possible to derive the altered distance in a curve. Since the arc length for the road centerline matches the resolution ds_r, the angle α over the traveled distance can be computed as:

   $$\alpha = \kappa_r' ds_r \tag{4.4}$$

   The altered radius, and altered step length, in the curves can be derived as:

   $$R_{alter} = R - \mathbf{t}_r = \left(\frac{1}{\kappa_r'} - \mathbf{t}_r\right) \tag{4.5}$$

   $$\boldsymbol{\Delta} s_r' = \frac{1}{\kappa_r'}\alpha - \left(\frac{1}{\kappa_r'} - \mathbf{t}_r\right)\alpha = -\kappa_r' \mathbf{t}_r ds_r \tag{4.6}$$

   By computing the cumulative sum of the altered step length, and adding the total distance, it is possible to derive the complete distance profile for all lines parallel to the centerline of the road, i.e., the total distance following different values of $\mathbf{t}_r$.

   $$\boldsymbol{\Lambda}_{s_r}' = \mathbf{M}_{\Sigma} \boldsymbol{\Delta} s_r + \mathbf{s}_r' \tag{4.7}$$

7. Finally, the combined longitudinal slope profile can be computed from the change in elevation over the change in distance.

   $$\boldsymbol{\Lambda}_{g_r}' = \frac{d\boldsymbol{\Lambda}_{z_r}'}{d\boldsymbol{\Lambda}_{s_r}'} \tag{4.8}$$

Figure 4.4a portrays the elevation profile $\boldsymbol{\Lambda}_{z_r}'$ of the example road in reference coordinates $(\mathbf{s}_r, \mathbf{t}_r)$, and Figure 4.4b displays the same road in global coordinates

(X, Y). However as vehicle dynamics model does not take elevation into consideration, a better way of describing the same road surface is by using the road banking and grade profiles $\mathbf{\Lambda}'_{b_r}, \mathbf{\Lambda}_{g'_r}$. The banking profile for the same example is showcased in Figure 4.4c, and the road grade in Figure 4.4d.

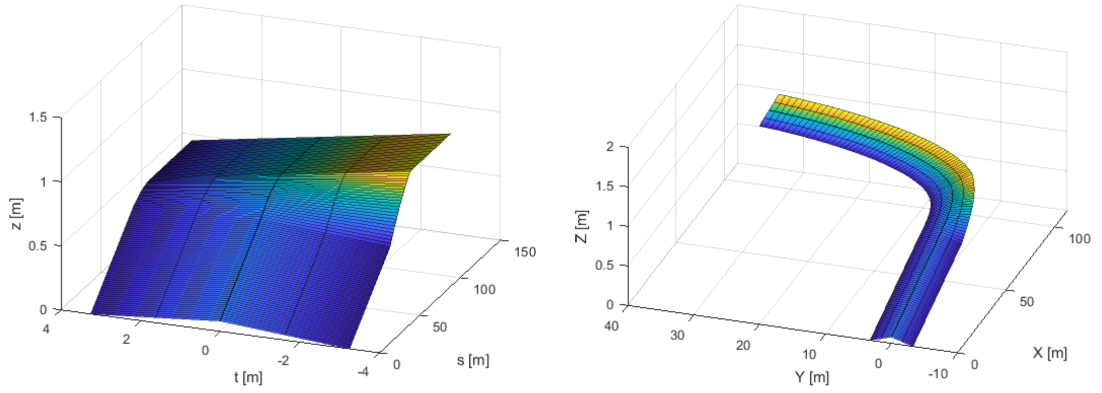

(a) Elevation - Reference coordinates **(b)** Elevation - Global coordinates

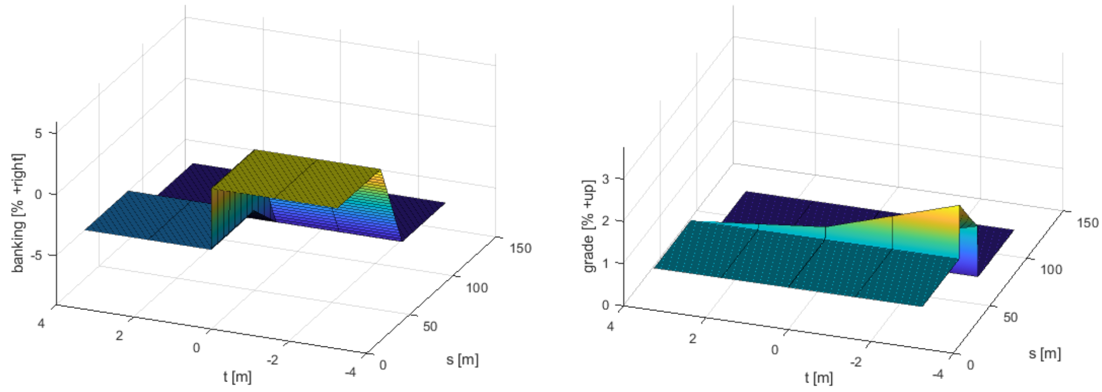

(c) Banking - Reference coordinates **(d)** Road grade - Reference coordinates

Figure 4.4: Generated elevation and slope profiles for an example road using the road construction algorithm.

4.5 Integrating road model with vehicle dynamics model

Even though the banking and road grade normally varies across a road surface. The variation in banking and road grade across the vehicle are negligible as long as the transition distances are long, and the driver does not cross the crown to an opposing lane. Since this is the case most of the time, it is possible to assume that the banking and inclination are the same for all of the wheels of the vehicle. Furthermore, if we assume that the driver follows a specific lane, and that the heading error is small, the problem of finding the properties is reduced to a single dimension. This is accomplished by determining the offset t_r, from the lane center to the road reference line, and then extracting the corresponding columns in $\mathbf{\Lambda}'_{b_r}$, and $\mathbf{\Lambda}'_{g_r}$, along with the longitudinal distance $\mathbf{\Lambda}'_{s_r}$. As long as the traveled distance of the vehicle is known, the road properties at that exact location can be determined using linear interpolation. It is also important to notice that the curvature changes from the reference line to the lane center, where the new curvature is derived from Equation (4.5) simply as $\kappa = 1/R_{alter}$.

In summary, the problem of finding the road properties is then reduced to only depend on the traveled distance of the vehicle units. Given the assumption that both of the vehicle units follow the road, the travelled distance for the second unit can simply be approximated from the COM lengths to the coupling points as:

$$s_2 = s_1 + (x_{c,12} - x_{c,21}) \tag{4.9}$$

It is hence possible to extract the road properties of both units along with the curvature, just from the position of the first unit:

$$\begin{bmatrix} \lambda_{b1} \\ \lambda_{b2} \\ \lambda_{g1} \\ \lambda_{g2} \\ \kappa_1 \end{bmatrix} = f_{road}(s_1) \tag{4.10}$$

As already described in section 2.2, The banking and road grade generates additional longitudinal and lateral forces affecting the vehicle motion. Since the variation of the banking across the different axles in the one-track model is assumed to be negligible, the resulting generated forces can be simplified to the lateral and longitudinal components of the gravitational pull [25]. Since the slope is expressed in percentages, they need to be transformed to angles. For small angles it is however justified to assume $\arctan(\lambda) \approx \sin(\lambda) \approx \lambda$.

$$F_{ryi} = m_i g \sin(\arctan(\lambda_{bi}) \tag{4.11}$$

$$F_{rxi} = -m_i g \sin(\arctan(\lambda_{gi}) \tag{4.12}$$

5

Derivation of state space models

In order to use the model to efficiently make predictions, it is convenient to have the model on explicit state space form, as in [20]. This chapter explains how the implicit equations of motion are used to formulate an explicit state space representation of the dynamics present in the systems. The chapter also delves into how the model is linearized and discretized.

5.1 Nonlinear State Space

For references, when deriving the EOM of the system by using Lagrange mechanics, the EOM are obtained on implicit ODE form expressed as:

$$F\Big(\dot{\mathbf{x}}(t), \mathbf{x}(t), \mathbf{u}(t), \mathbf{r}(t)\Big) = 0, \tag{5.1}$$

Where $\mathbf{x}(t)$ is the system state and $\mathbf{u}(t)$ and $\mathbf{r}(t)$ are the inputs affecting the motion. For a one-track two unit model, with the tractor having 2 axles, with a single steerable front axle, and the semitrailer having 3 axles, the states, inputs and road properties are given as:

$$\mathbf{x}(t) = \begin{bmatrix} v_{x1} \\ v_{y1} \\ \phi_1 \\ \dot{\phi}_1 \\ \theta_2 \\ \dot{\theta}_2 \end{bmatrix}, \mathbf{u}(t) = \begin{bmatrix} \delta_{11} \\ F_{xw11} \\ F_{xw12} \\ F_{xw21} \\ F_{xw22} \\ F_{xw23} \end{bmatrix}, \mathbf{r}(t) = \begin{bmatrix} \lambda_{b1} \\ \lambda_{b2} \\ \lambda_{g1} \\ \lambda_{g2} \end{bmatrix} \tag{5.2}$$

In this case $\mathbf{x}(t)$ can be solved, using implicit integration methods if the initial conditions are provided, i.e., $(\mathbf{x}(t_0), \dot{\mathbf{x}}(t_0))$, along with the control inputs and road properties at each time step. However, implicit integration methods requires to solve the EOM at each prediction step, which for the complex system could be difficult to achieve real time computations. Fortunately, the accelerations in the Lagrange equation enters linearly which means we can solve for $\dot{\mathbf{x}}(t)$ [28]. It is then possible to derive the explicit nonlinear state space form as:

$$\dot{\mathbf{x}}(t) = f\Big(\mathbf{x}(t), \mathbf{u}(t), \mathbf{r}(t)\Big), \tag{5.3}$$

$$\mathbf{y}(t) = g\Big(\mathbf{x}(t), \mathbf{u}(t), \mathbf{r}(t)\Big), \tag{5.4}$$

Where the non-linear function $f(\mathbf{x}(t), \mathbf{u}(t), \mathbf{r}(t))$ computes the state derivatives $\dot{\mathbf{x}}(t)$ and the function $g(\mathbf{x}(t), \mathbf{u}(t), \mathbf{r}(t))$ computes the outputs of interest $\mathbf{y}(t)$. In the case of a tractor-semitrailer combination where the lateral accelerations a_{y1}, a_{y2} are used to detect if the rollover limits are violated, $g\Big(\mathbf{x}(t), \mathbf{u}(t), \mathbf{r}(t)\Big)$ are given by:

$$\mathbf{y}(t) = g\Big(\mathbf{x}(t), \mathbf{u}(t), \mathbf{r}(t)\Big) = \begin{bmatrix} a_{y1} \\ a_{y2} \end{bmatrix} = \begin{bmatrix} \dot{v}_{y1} + v_{x1}\dot{\phi}_1 \\ \dot{v}_{y2} + v_{x2}\dot{\phi}_2 \end{bmatrix} \tag{5.5}$$

The output a_{y2} is dependent of the states of the second unit, however these states are not in the state vector $\mathbf{x}(t)$. Instead, the longitudinal and lateral velocity in the second unit, along with their time derivatives, are expressed in terms of the first unit. These states are acquired by applying a rotation on Equation (3.14), as well as computing the time derivative.

Moreover, as seen from Equation (5.5), the outputs do not just simply depend on the states $\mathbf{x}(t)$, but also the state derivatives $\dot{\mathbf{x}}(t)$. As such, another way of expressing the output function $g(\mathbf{x}, \mathbf{u}, \mathbf{r})$ is

$$\mathbf{y}(t) = g\Big(\mathbf{x}(t), \mathbf{u}(t), \mathbf{r}(t)\Big) = g\Bigg(f\Big(\mathbf{x}(t), \mathbf{u}(t), \mathbf{r}(t)\Big), \mathbf{x}(t)\Bigg) = g\Bigg(\dot{\mathbf{x}}(t), \mathbf{x}(t)\Bigg) \tag{5.6}$$

5.2 Numerical integration and discretization of nonlinear state space

In a control context, where the signals are measured in discrete time it is more convenient to express the states and inputs as discrete variables. Given the state vector, the inputs and the road properties at time t_k, the state vector for the next time instant t_{k+1} can be computed through integration:

$$\mathbf{x}(t_{k+1}) = \mathbf{x}(t_k) + \int_{t_k}^{t_{k+1}} f\Big(\mathbf{x}(\tau), \mathbf{u}(\tau), \mathbf{r}(\tau)\Big)\, d\tau \tag{5.7}$$

However, since the integral of f is not easily obtainable, it must must be approximated using numerical integration methods. Numerical integration methods can be split into two major families: implicit and explicit methods. The main difference between implicit and explicit methods is that explicit methods only use the information up to a given time to approximate a solution for the next state, while implicit methods also use subsequent information from the later states and solves an equation at each timestep. The implicit methods are more computationally expensive than the explicit ones, which can be a problem if the predictions are to be performed real time. The main benefit of using implicit integration schemes are that they are less prone to stability issues and hence more accurate for stiff systems. Due to the hard time constraint, of new predictions required to be performed every 10 ms, and to effectively be able to use the Kalman filter equations to predict the uncertainty, we have chosen to only evaluate the explicit methods in this thesis.

The easiest and least computationally expensive method to approximate the integral is the forward Euler method:

$$\mathbf{x}_{k+1} \approx \mathbf{x}_k + \dot{\mathbf{x}}_k \Delta t \tag{5.8}$$

where Δt is the step size. Equation 5.8 is derived from the first order Taylor expansion. However, since the accuracy of first order methods rely heavily on the step size Δt, the forward Euler method sometimes requires impractically small steps to remain accurate. In this thesis, where we are trying to predict the vehicle motion a specific time ahead, we are limited by the amount of steps we can take to obtain real-time computational capabilities. Higher order methods that are more accurate for larger step sizes might therefore be convenient to achieve this goal. Some widely used higher-order methods are the Runge-Kutta (RK) methods. RK methods take some intermediate steps, e.g. half-steps, which requires additional evaluations of the function, but obtain a higher order and accuracy [28]. The Euler, RK2 and RK4 integration schemes will be considered in this thesis for the nonlinear model.

5.3 Linearization of state space

The obtained state-space representation from Section 5.1 is nonlinear. However in vehicle dynamics and control context it is common to simplify the models and reduce the complexity for more efficient computations. If we assume constant longitudinal velocity, i.e the driver being a cruise controller, we can estimate the behavior of the system by linearizing around an equilibrium point, (constant longitudinal speed, no steering, on a flat road). For the nonlinear continuous-time system we can approximate the behavior as:

$$\dot{\mathbf{x}}(t) \approx \mathbf{A}_{c,k}\mathbf{x}(t) + \mathbf{B}_{uc,k}\mathbf{u}(t) + \mathbf{B}_{rc,k}\mathbf{r}(t) \tag{5.9}$$

$$\mathbf{y}(t) \approx \mathbf{C}_{c,k}\mathbf{x}(t) + \mathbf{D}_{uc,k}\mathbf{u}(t) + \mathbf{D}_{rc,k}\mathbf{r}(t) \tag{5.10}$$

Where the matrices $\mathbf{A}_{c,k}$, $\mathbf{B}_{uc,k}$, and $\mathbf{B}_{rc,k}$ are the partial derivatives of the vehicles dynamics function f with respect to the equilibrium point denoted by $(\mathbf{x}_{0,k}, \mathbf{u}_0, \mathbf{r}_0)$. The matrices $\mathbf{C}_{c,k}$, $\mathbf{D}_{uc,k}$, and $\mathbf{D}_{rc,k}$ are the partial derivatives of the output function g with respect to the same equilibrium point. The subscript k denotes the time instant of linearization, i.e the longitudinal velocity at that time. The matrices are obtained by computing the Jacobian with respect to the states, driver inputs and road inputs of the system:

$$\mathbf{A}_{c,k} = \left.\frac{\partial f}{\partial \mathbf{x}}\right|_{(\mathbf{x}_k,\mathbf{u}_0,\mathbf{r}_0)} \qquad \mathbf{B}_{uc,k} = \left.\frac{\partial f}{\partial \mathbf{u}}\right|_{(\mathbf{x}_k,\mathbf{u}_0,\mathbf{r}_0)} \qquad \mathbf{B}_{rc,k} = \left.\frac{\partial f}{\partial \mathbf{r}}\right|_{(\mathbf{x}_k,\mathbf{u}_0,\mathbf{r}_0)} \tag{5.11}$$

$$\mathbf{C}_{c,k} = \left.\frac{\partial g}{\partial \mathbf{x}}\right|_{(\mathbf{x}_k,\mathbf{u}_0,\mathbf{r}_0)} \qquad \mathbf{D}_{uc,k} = \left.\frac{\partial g}{\partial \mathbf{u}}\right|_{(\mathbf{x}_k,\mathbf{u}_0,\mathbf{r}_0)} \qquad \mathbf{D}_{rc,k} = \left.\frac{\partial g}{\partial \mathbf{r}}\right|_{(\mathbf{x}_k,\mathbf{u}_0,\mathbf{r}_0)} \tag{5.12}$$

Where the linearization is conducted around the equilibrium point where the vehicle is traveling straight forward with constant longitudinal speed $v_{x,k}$, no driver inputs, and the vehicle is situated on a flat road. The linearization point is given by:

$$\mathbf{x}_k = \begin{bmatrix} v_{x,k} \\ \mathbf{0}_{(n_x-1)\times 1} \end{bmatrix}, \quad \mathbf{u}_0 = \mathbf{0}_{n_u\times 1}, \quad \mathbf{r}_0 = \mathbf{0}_{n_r\times 1} \tag{5.13}$$

As the longitudinal velocity changes under operation, it means that the system is linear time variant (LTV). The linear matrices capture the local linear behavior of the system around the equilibrium point $(\mathbf{x}_k, \mathbf{u}_0, \mathbf{r}_0)$. By extending the linearization beyond just the ordinary $\mathbf{A}_{c,k}$ and $\mathbf{B}_{uc,k}$ matrices, it is possible to incorporate the information about the road $\mathbf{r}$ through the matrix $\mathbf{B}_{rc,k}$ and how the road properties will affect the state trajectory.

5.4 Numerical integration and discretization of linear state space

Similarly to the non-linear state space models, it requires integration methods to approximate the states at another time instant. It can also be computed using Forward Euler, RK methods or any other integration schemes. However, for the linear case, if the $\mathbf{A}_{c,k}$ matrix is non-singular, it is possible to convert the linear, continuous state-space model into a discrete form directly by analytically computing its discrete counterpart according to:

$$\begin{aligned}
\mathbf{A}_{d,k} &= e^{\mathbf{A}_{c,k}\Delta t} && (5.14)\\
\mathbf{B}_{ud,k} &= \left(\int_{\tau=0}^{\Delta t} e^{\mathbf{A}_{c,k}\tau} d\tau\right)\mathbf{B}_{uc,k} && (5.15)\\
\mathbf{B}_{rd,k} &= \left(\int_{\tau=0}^{\Delta t} e^{\mathbf{A}_{c,k}\tau} d\tau\right)\mathbf{B}_{rc,k} && (5.16)\\
\mathbf{C}_{d,k} &= \mathbf{C}_{c,k} && (5.17)\\
\mathbf{D}_{ud,k} &= \mathbf{D}_{uc,k} && (5.18)\\
\mathbf{D}_{rd,k} &= \mathbf{D}_{uc,k} && (5.19)
\end{aligned}$$

In this process, we obtain the discretized state-space representation:

$$\begin{aligned}
\mathbf{x}_{k+1} &\approx \mathbf{A}_{d,k}\mathbf{x}_k + \mathbf{B}_{ud,k}\mathbf{u}_k + \mathbf{B}_{rd,k}\mathbf{r}_k && (5.20)\\
\mathbf{y}_k &\approx \mathbf{C}_{d,k}\mathbf{x}_k + \mathbf{D}_{ud,k}\mathbf{u}_k + \mathbf{S}_{rd,k}\mathbf{r}_k && (5.21)
\end{aligned}$$

In this discrete state space representation the states are no longer expressed as a function of time $\mathbf{x}(t)$ but instead expressed at given time instances $\mathbf{x}_k$. The same logic applies for the input and road. If we assume that $\mathbf{u}(t)$ and $\mathbf{r}(t)$ are constant during the timestep the discretized LTV system can be computed more efficiently through matrix concatenation and slicing as:

$$\begin{bmatrix} \mathbf{A}_{d,k} & \mathbf{B}_{ud,k} & \mathbf{B}_{rd,k} \\ \mathbf{0} & \mathbf{I}_{n_u \times n_u} & \mathbf{0} \\ \mathbf{0} & \mathbf{0} & \mathbf{I}_{n_r \times n_r} \end{bmatrix} = e^{\begin{bmatrix} \mathbf{A}_{c,k} & \mathbf{B}_{uc,k} & \mathbf{B}_{rc,k} \\ \mathbf{0} & \mathbf{0} & \mathbf{0} \\ \mathbf{0} & \mathbf{0} & \mathbf{0} \end{bmatrix}\Delta t} \tag{5.22}$$

The matrix $\mathbf{B}_{rd,k}$ is computed in an identical manner as $\mathbf{B}_{ud,k}$. The reason for this is simply that the road $\mathbf{r}_k$ can be seen as a different set of inputs to the system. It would hence be possible to combine these matrices into a single matrix, but considering the significant difference of the two input types, where $\mathbf{u}_k$ comes from the driver and can be controlled whereas $\mathbf{r}_k$ comes from the road and is a direct function of the vehicle position, we have chosen to keep the terms separate.

To select a suitable model for the PTA, the accuracy, stability and computation time of the different methods were compared. The results are presented in the next chapter. The models where evaluated for both a stepsize of $\Delta t = 10ms$, and $\Delta t = 100ms$.

6

Evaluation and Comparison of models and integration methods

This chapter covers the test road that was constructed to be used in the evaluation process. How the models were evaluated against a high-fidelity model as well as the tuning of the vehicle dynamics models. Tables are presented that shows the mean squared error for the different models and integration methods to compare the strength and weaknesses for the different models.

6.1 Test manoeuvre

To evaluate the performance and accuracy of the vehicle dynamics models, a simulated test road where built based on the National Traffic Highway Safety Administration (NHTSA) roll stability tests for heavy vehicles [33, 34]. The road in question is a J-turn, which mimics a highway exit. In addition, banking was also implemented in accordance with standards on how Swedish roads should be banked to reduce risk of crossfall [4]. Banking was added in the curve to ensure that the evaluation encapsulates the roads influence on the vehicular dynamics. An illustration of the constructed road and its intended travel path is given in Figure 6.1.

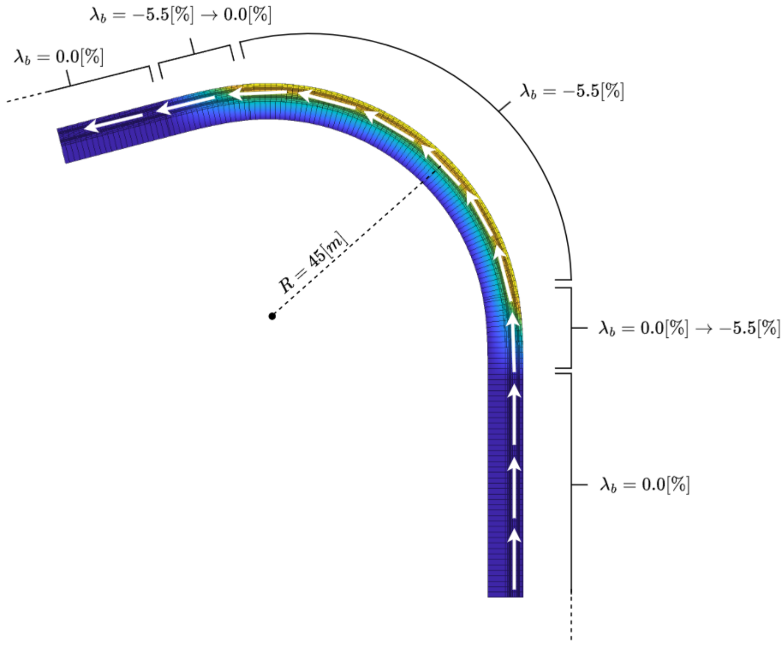

Figure 6.1: J-turn road with banking in turn. The radius of the turn is $45[m]$ with a transition period of around 15 [m] with linearly increasing curvature and banking. The vehicle will travel according to the white arrows (right lane). The heatmap on the road indicates the elevation of the road through its profile.

J-turn manoeuvre description: The manoeuvre will be done in accordance with the test performed by the NHTSA [33]. The vehicle will start by going straight forward with no steering input, thereafter the steering rate is set constant until the desired yaw rate is obtained to match curvature of a $45m$ radius turn. At that point, the steering is kept constant to maintain the yaw rate. The longitudinal velocity is selected to be just below the maximum velocity for the vehicle to not rollover on a flat road, in this case $44[km/h]$, in order to emphasize the road geometry influence over the vehicle dynamics.

6.2 High-fidelity model data adaptation

In order to properly validate the derived models, they had to be tested against a high fidelity simulation model. The model used in this study is called *Volvo Transport Model* (VTM), and is developed by Volvo Group Trucks Technology. The VTM was considered to be the "ground truth" in the model evaluation. The high fidelity model can simulate different vehicular configurations on many sets of roads. The high fidelity model will travel on the path defined by Figure 6.1 in the simulation environment.

To do a fair evaluation, the data obtained from the VTM model had to be adjusted in some areas to be utilized in our derived dynamics model. This had to be done as our model did not contain as many degrees of freedom as the VTM. The VTM model is a two-track model with Ackermann steering. That meant the propulsion forces and lateral forces had to be adjusted to fit our one-track model.

6.3 Model tuning

Beyond adapting the data obtained from the VTM, the derived dynamics model had to be tuned to match the data. The tuning was done by changing the tire parameters to allow for a better curve fitting. All the vehicle specific parameters were taken from the VTM. The cornering stiffness of the tyres were tuned by looking at the Normalized Lateral force to the lateral slip ratio of the lumped wheels. In this way the lateral slip stiffness coefficient CC_y could be found which together with the static axle loads obtained from the VTM formed the cornering stiffness. Figure 6.2 shows the normalized lateral force of the lumped wheels of the second axle, giving $CCy \approx 2.68$. This value was used for all axles except the first one, which was identified to generate too high lateral forces for the vehicle to follow the reference model. CC_y of the first axle was therefore manually fine tuned to identify a better fit with VTM. This process was done iteratively, but it should be mentioned that this tuning process can be done in other ways, such as utilizing optimization methods.

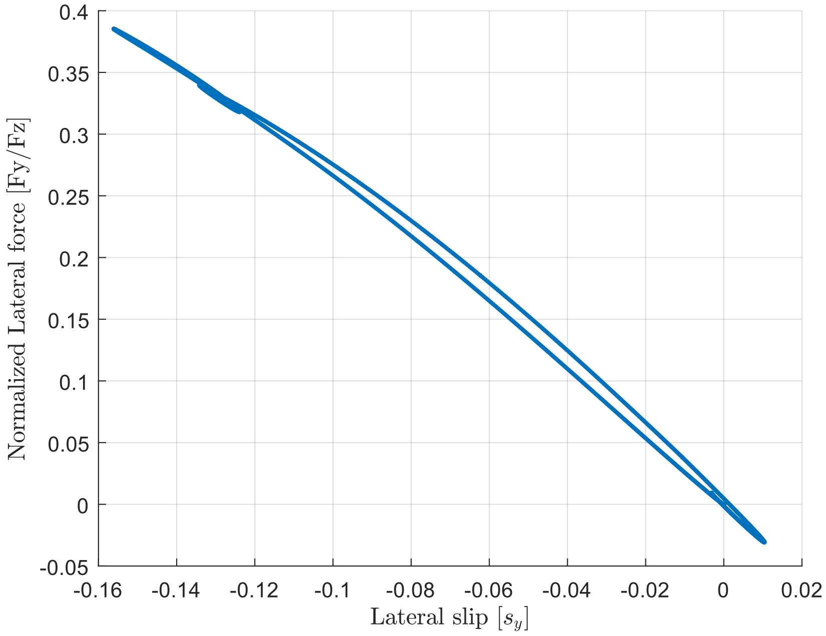

Figure 6.2: Normalized Lateral force of the lumped wheels obtained from the high-fidelity simulation. The gradient of the data points are approximately -2.68 and hence the lateral slip stiffness coefficient becomes $CC_y \approx 2.68$

6.4 Results from evaluating model accuracies

The combination used for the model evaluation is a Volvo FH tractor coupled with a semitrailer. The numerical parameters for the vehicle configuration has been obtained internally from the VTM directly. The numerical vehicle parameters used in our model is presented in Table C.1 found in Appendix C. By propagating the inputs from the path follower in the VTM through our model, we obtain state trajectories of both models that could be compared. By computing the mean squared error (MSE) between the true state of the high-fidelity model and the predicted ones, the performance of the different models and integration methods could be compared. The inputs used were the steering angle and the propulsion forces of the different axles.

The same model evaluation is done for different time step sizes, where large step sizes and high accuracy is preferable. Here we present two different time step lengths, $\Delta t = 0.1$ and $\Delta t = 0.01$. The results of the models with stepsize $\Delta t = 0.1$ are presented in Table 6.1. The results with stepsize $\Delta t = 0.01$ are presented in Table 6.2.

Table 6.1: MSE for states and outputs, different models and integration methods ($\Delta t = 0.1$).

Veh. Model	MSE x_1	MSE x_2	MSE x_3	MSE x_4	MSE x_5	MSE x_6
L - Analytical	4.72e-03	1.38e-03	0.73e-03	6.26e-05	2.22e-05	5.71e-05
NL - Euler	8.68e-04	1.69e-03	0.71e-03	11.12e-05	8.14e-05	2.27e-04
NL - RK2	1.41e-03	1.79e-03	0.70e-03	6.42e-05	4.46e-05	4.83e-05
NL - RK4	1.47e-03	1.69e-03	0.70e-03	6.38e-05	4.42e-05	5.56e-05

Veh. Model	MSE $a_{y,1}$	MSE $a_{y,2}$	Comp. time per step [ms]*
L - Analytical	2.16e-04	1.78e-04	0.1272
NL - Euler	1.42e-04	1.54e-04	0.4380
NL - RK2	1.59e-04	2.54e-04	0.6740
NL - RK4	1.46e-04	2.30e-04	1.1418

*Average over 100 simulations.

Table 6.2: MSE for states and outputs, different models and integration methods ($\Delta t = 0.01$).

Veh. Model	MSE x_1	MSE x_2	MSE x_3	MSE x_4	MSE x_5	MSE x_6
L - Analytical	4.76e-03	1.35e-03	1.11e-03	8.37e-05	3.45e-05	9.27e-05
NL - Euler	1.50e-03	1.64e-03	1.07e-03	8.63e-05	5.85e-05	10.31e-05
NL - RK2	1.56e-03	1.64e-03	1.07e-03	7.87e-05	5.52e-05	9.01e-05
NL - RK4	1.56e-03	1.64e-03	1.07e-03	7.80e-05	5.49e-05	8.90e-05

Veh. Model	MSE $a_{y,1}$	MSE $a_{y,2}$	Comp. time per step [ms]*
L - Analytical	1.97e-04	1.99e-04	0.1180
NL - Euler	1.47e-04	1.29e-04	0.4604
NL - RK2	1.41e-04	1.30e-04	0.6846
NL - RK4	1.40e-04	1.30e-04	1.1448

*Average over 100 simulations.

The results from Table 6.1-6.2 are indicative that no model suffers from significant inaccuracies, but overall shows promising performance. The accuracies varies between states, where states x_1, x_2 and x_3 have mean squared error around 10^{-3} and the remaining states x_4, x_5 and x_6 has smaller errors around 10^{-5}. Nevertheless, the most important measure to predict rollover is the lateral accelerations of the vehicular units. The accuracies of the outputs differ between the linear and non-linear model, however the variation between the different integration methods for the non-linear models does not improve the result significantly.

The largest tangible difference is the computation time for the models. The linear model takes the shortest amount of time as it computes the next state estimate only by linear operations. The nonlinear models take significantly more time. Using the Euler integration, the next state estimate is obtained first through a large number of nonliner computations in the state-space, and then one linear operation for the integration step. The RK2 method calls the nonlinear state space function twice and the RK4 method calls it 4 times. The RK4 method takes the longest to perform, up to 10 times longer compared to the linear model. The accuracy improvement from RK4 is negligible in relation to its increase in computation time.

The state trajectories for the different models, integration methods and step sizes in the evaluation process are presented completely in appendix B. For reference, we illustrate the linear model and the non-linear model with the forward Euler integration method in Figure 6.3-6.4 and Figure 6.5-6.6 respectively.

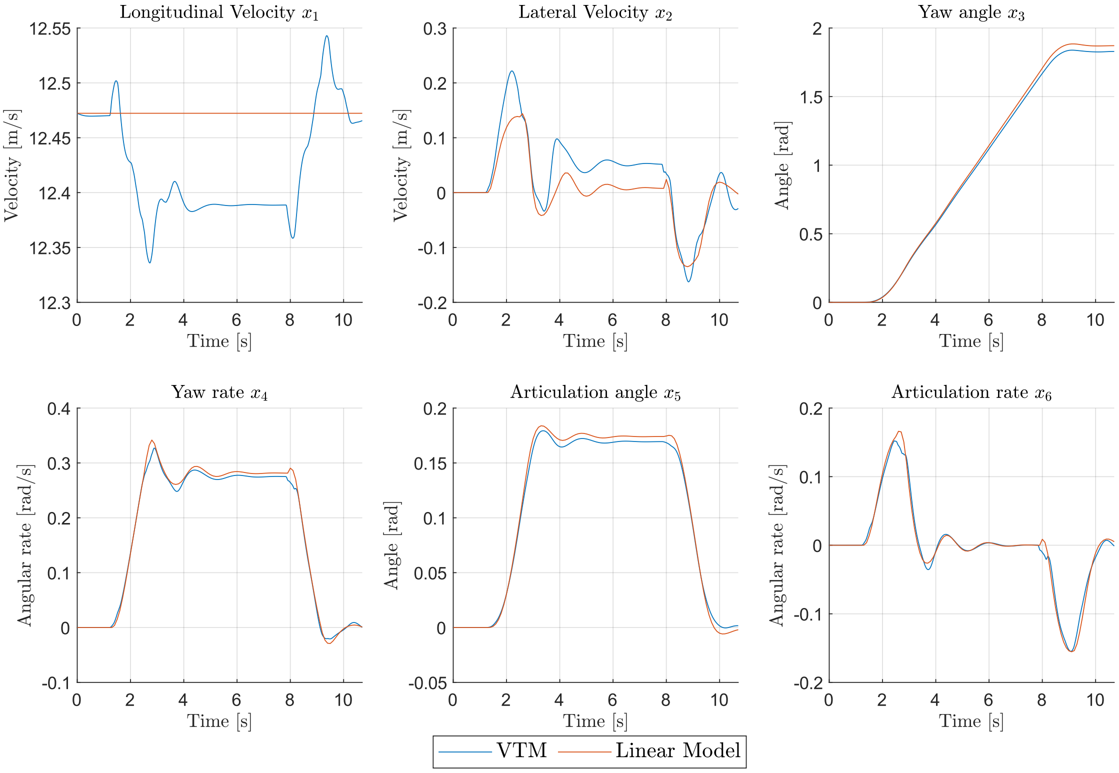

Figure 6.3: Vehicle model states from propagating inputs from VTM. The high fidelity model VTM is the blue graph, the derived Linear Vehicle dynamics model is the red graph. $\Delta t = 0.1$.

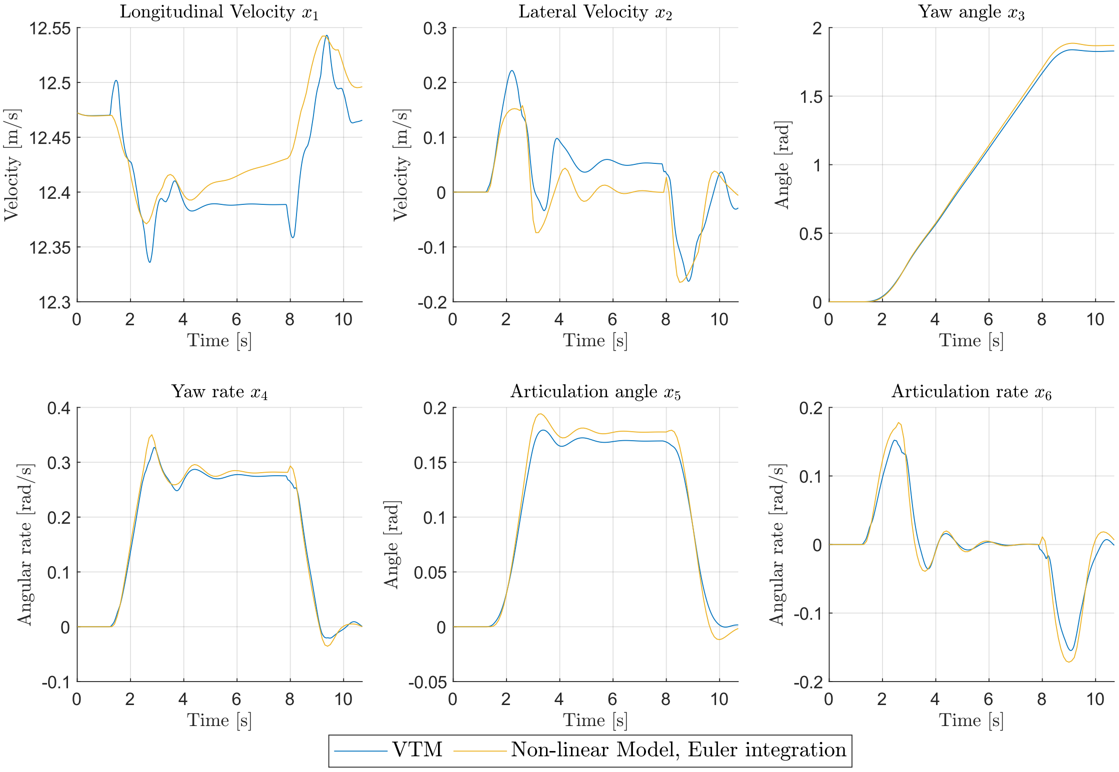

Figure 6.5: Vehicle model states from propagating inputs from VTM. The high fidelity model VTM is the blue graph, the derived Non-linear Vehicle dynamics model with forward Euler integration is the yellow graph. $\Delta t = 0.1$.

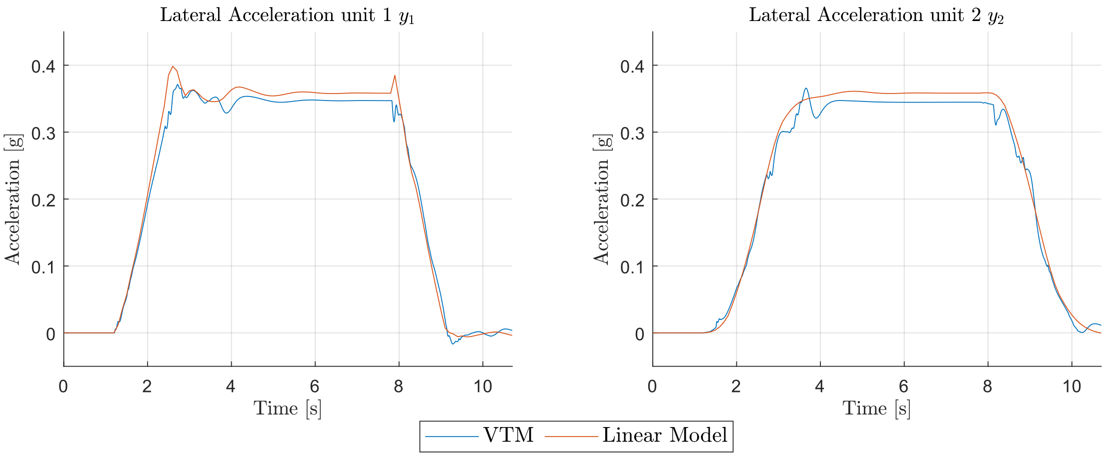

Figure 6.4: Vehicle model outputs from propagating inputs from VTM. The high fidelity model VTM is the blue graph, the derived Linear Vehicle dynamics model is the orange graph. $\Delta t = 0.1$.

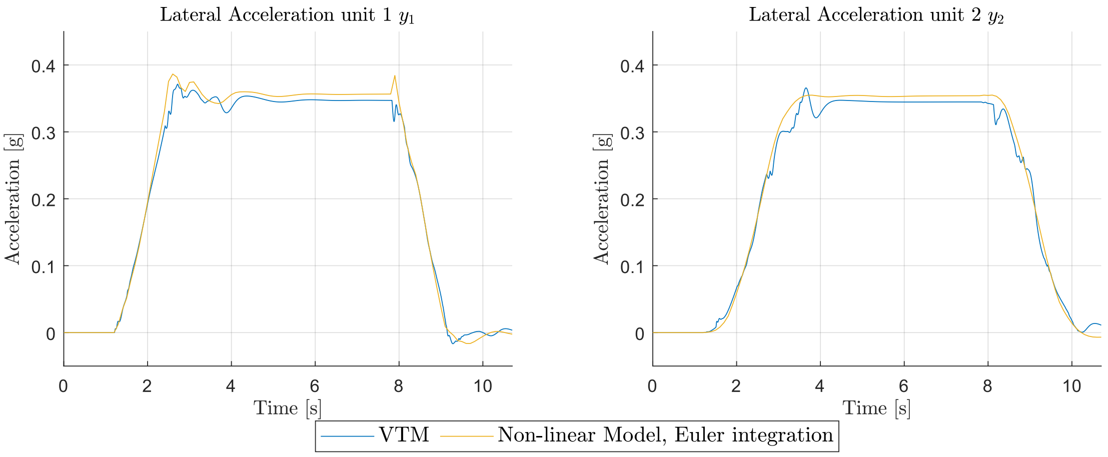

Figure 6.6: Vehicle model outputs from propagating inputs from VTM. The high fidelity model VTM is the blue graph, the derived Non-linear Vehicle dynamics model with forward Euler integration is the yellow graph. $\Delta t = 0.1$.

As evident in the Figures, the largest difference between the models is apparent in the first state x_1. The linear model assumes constant longitudinal velocity - so neither of the inputs, the road nor previous vehicle states has effect on the vehicle speed. However, this is not the case for the non linear model - where all of the mentioned factors will impact the longitudinal speed.

The second state x_2, lateral velocity, follows the trend in the VTM for both models. During the turn, the lateral velocity is centered around zero, which indicates that it is close to steady state.

Futhermore, the remaining states x_3, x_4, x_5 and x_6 shows a great fit to the high-fidelity model and captures the behaviour with great precision. With this model evaluation, we can confidently move forward and decide on what derived vehicle dynamics model to use in a predictive context to perform the predictive threat assessment.

7

Predictive Modelling

This chapter explains how the length of the prediction horizon was selected. It also covers how the vehicle dynamics model was utilized for predictions of driver inputs and the road properties. It is explained how the vehicle trajectory is converted into space domain to extract the road properties, and a simple driver model is presented that aims to follow the curvature of the upcoming road.

7.1 Prediction horizon

When predicting dangerous scenarios, it is crucial to consider how far into the future you need to look to allow sufficient time for threat identification and preventative action. Research indicates that for some stability programs, a 0.5-second prediction horizon is enough to detect potential dangers [35]. However, extending this horizon further can enhance control robustness and enable earlier interventions. The study also found that prediction horizons up to 3 seconds can provide greater assurance.

Several factors must be considered when selecting the prediction horizon: Actuator delays, the driver reaction time, and the time to slow down the vehicle to a safe state all needs to be considered when choosing a suitable prediction horizon. A longer prediction horizon can mitigate the impact of such delays and provide additional safety.

The actuator delay refers to the time interval between making a request and actuators executing said request. For the PTA proposed in this thesis it will namely be the delay of the brakes. This includes the brake lag and the brake rise time, i.e., the time it takes for air pressure to build up, when the brake pedal is pressed, to when the brakes are applied. Studies has shown that this delay is approximately 0.25-0.48s [36], for tractor-semitrailer combinations.

The next delay to consider is the driver reaction time. If the main goal of the PTA is to warn the driver, the time it takes for the driver to react must be considered. On average, drivers take about 1.5 seconds to react to sudden hazards [37], so incorporating this reaction time into the prediction horizon ensures that drivers can respond adequately to warnings.

Lastly, heavy vehicles require a certain amount of time and distance to decelerate to safe state. Estimating this time is challenging as it depends on factors such as the current speed of the vehicle and the imminent threat, both of which vary from one situation to another. If the vehicle is applying $-5m/s^2$ brake which for a tractor-semitrailer is considered hard braking, it takes approximately 0.56 seconds to slow the vehicle down by $10[km/h]$.

Considering all these delays, we have determined that a prediction horizon of 3 seconds should be sufficient for detecting hazardous situations, well in advance, to have the necessary time to decelerate the vehicle in a safe manner.

7.2 Selecting vehicle model and step size

As the previous chapter demonstrated, all the models showed promising performance in the evaluation. However, the decision was made to use the linearized model with timesteps of $\Delta t = 0.1[s]$ for the PTA.

The motivation for this is that the model accuracy in relation to the time it takes to compute a horizon is preferable. Moreover even though the model consists of several non-linear operations, the behaviour of the system is still rather linear, and captures the dynamics rather well. Also, the linear model enables the usage of the Kalman filter equations for uncertainty propagation, which in an efficient and convenient way allows predictions of what the distribution of the states will become.

A prediction horizon of $3[s]$, and a step size of $\Delta t = 0.1[s]$ requires 30 steps to predict the entire horizon, whereas a step size of $\Delta t = 0.01[s]$ requires 300 steps. Smaller steps generally generate better accuracy, but as the evaluation showed - this improvement was negligible. The reduced computational cost of the lower step size was considered preferable when trying to obtain real-time capabilities.

7.3 Introducing timesteps and prediction steps

The vehicle is assumed to generate measurements at a frequency of $100\,Hz$, which corresponds to one measurement every $\Delta t = 0.01\,[s]$. Whereas the predictions are performed every $0.1s$. To differentiate between the two time steps, different notations will be used. k is used for the time instant, indicating the current point in time. p is used for a prediction step 10 steps ahead. To indicate the time at which a measurement was obtained, the notation $k \mid k$ is introduced. $k + p \mid k$ means a single prediction step ahead and $k + np \mid k$ means an arbitrary prediction state, where $n \in [0, 30]$. We will also introduce the step size $\Delta t_{pred} = 0.1s$ used for the predictions.

7.4 Prediction of road properties

As described in Chapter 4, the road properties are modelled in the space domain. For reference, the road properties of both vehicle unit is given by the function below. For the specific time instance $k \mid k$ we have:

$$\begin{bmatrix} \lambda_{b1,k|k} \\ \lambda_{b2,k|k} \\ \lambda_{g1,k|k} \\ \lambda_{g2,k|k} \\ \kappa_{1,k|k} \end{bmatrix} = f_{road}(s_{1,k|k}) \tag{7.1}$$

Since the vehicle dynamics model is expressed in the time domain, it is necessary to convert the model to space domain to combine them in practice. If the location in global coordinates $(X_{1,k|k}, Y_{1,k|k})$, the velocity $(v_{x1,k|k},\ v_{y1,k|k})$, the heading $(\phi_{1,k|k})$ and the accelerations $(a_{x1,k|k},\ a_{y1,k|k})$ of the first unit are known, it is possible to predict the future position and the travelled distance at the next predicted time instant $k + p \mid k$. Using a constant acceleration model, the position of the subsequent step is given by:

$$\begin{bmatrix} X_{1,k+p|k} \\ Y_{1,k+p|k} \end{bmatrix} = \begin{bmatrix} X_{1,k|k} \\ Y_{1,k|k} \end{bmatrix} + M_{WCS}^{VCS}(\phi_{1,k|k}) \begin{bmatrix} \Delta t_{pred} & \frac{\Delta t_{pred}^2}{2} & 0 & 0 \\ 0 & 0 & \Delta t_{pred} & \frac{\Delta t_{pred}^2}{2} \end{bmatrix} \begin{bmatrix} v_{x1,k|k} \\ a_{x1,k|k} \\ v_{y1,k|k} \\ a_{y1,k|k} \end{bmatrix} \tag{7.2}$$

Keep in mind that the longitudinal acceleration will always be zero for the linear state space model. Additionally, it is essential to know the current position of the vehicle. The assumption is made that there exists a localization method on the vehicle, that reliably estimates the vehicle's position and travelled distance at the present moment of driving. The predicted total travelled distance $s_{1,k+p|k}$ one step ahead can then be obtained by using the Euclidian norm according to:

$$s_{1,k+p|k} = s_{1,k|k} + \sqrt{\left(X_{1,k+p|k} - X_{1,k|k}\right)^2 + \left(Y_{1,k+p|k} - Y_{1,k|k}\right)^2} \tag{7.3}$$

The road properties of both units, at the new predicted location can then be extracted from the road model using the new position as input:

$$\begin{bmatrix} \lambda_{b1,k+p|k} \\ \lambda_{b2,k+p|k} \\ \lambda_{g1,k+p|k} \\ \lambda_{g2,k+p|k} \\ \kappa_{1,k+p|k} \end{bmatrix} = f_{road}(s_{1,k+p|k}) \tag{7.4}$$

In summary, knowing the position and trajectory of the vehicle at timestep $k \mid k$ enables the prediction of road properties at timestep $k + p \mid k$. This process can then be repeated for each prediction step and hence it is possible to predict the road properties $k + np \mid k$.

7.5 Prediction of Driver Inputs

Predicting the future driver inputs, for ADAS functions, is a challenging problem since there is a lot of uncertainty in what the driver will do next. Most advanced stability control systems today, such as ESCs, just rely on a steering angle sensor along with the position of the acceleration or brake pedal to determine the driver's intention [38]. Briefly explained, ESC compares the driver steering to the yaw rate and the lateral acceleration of the vehicle to detect loss of control situations. Since these systems do not have any information of the future road, they can only use the current and historic information of the vehicle state and inputs to take action.

Therefore it is necessary to create some form of controller or driver model that can generate a control sequence ahead of time. As that area could be an entire thesis of its own, we propose a simple predictive driver model (SPDM) that will generate steering inputs based on the curvature of the road. We will compare our derived predictive driver model with 2 other simple models, namely: a constant steering model and a constant steering rate model, which is models of the simplest prediction of what a driver will do when the control system is not aware of the future.

The SPDM is derived as follows. During steady state cornering at an arbitrary prediction step $k + np \mid k$, the following equality is assumed to hold:

$$a_{y1,k+np|k} = \frac{v_{x1,k+np|k}^2}{R_{1,k+np|k}} = v_{x1,k+np|k}\dot{\phi}_{1,k+np|k} \tag{7.5}$$

Where $R_{1,k+np|k}$ is the predicted radius of the curve at timestep $k + np \mid k$. The corresponding curvature of the road is given by $\kappa_{1,k+np|k} = 1/R_{1,k+np|k}$. From Equation (7.5) it is possible to estimate the required yaw rate $\dot{\phi}_{1,k+np|k}$ for the first unit to match the road curvature $\kappa_{1,k+np|k}$ according to:

$$\dot{\phi}_{1,k+np|k} = v_{x1,k+np|k}\kappa_{1,k+np|k} \tag{7.6}$$

We can then compute what steering angle is necessary in order to obtain the desired yaw rate to maintain the correct heading of the road. We do this by solving for the steering angle in the fourth equation of the discretized state space model. By substituting the yaw rate with our newly formed expression in the linear state space, we get the steering angle:

$$\mathbf{u}_{k+np|k}(1) = \frac{(\kappa_{1,k+(n+1)p|k}v_{x1,k+(n+1)p|k}) - \mathbf{A}_{d,k}(4,:)\mathbf{x}_{k+np|k} - \mathbf{B}_{rd,k}(4,:)\mathbf{r}_{k+np|k}}{\mathbf{B}_{ud,k}(4,1)} \tag{7.7}$$

Now one issue arises, which is that the desired steering angle depends on the longitudinal velocity and road curvature for the next time instant $k + (n+1)p \mid k$. As the curvature of the road in the next time instant $k+2p \mid k$ depends on what control action we take in the previous time instant $k+p \mid k$, some form of solver is required to find the optimal steering angle. However, this can be avoided by introducing two assumptions.

Firstly, as the linear state space model assumes constant longitudinal velocity, we can safely introduce the assumption that $v_{x1,k+(n+1)p|k} = v_{x1,k+np|k}$. Secondly, as the timesteps are small, the change in curvature between the timesteps are assumed to be small as well ($\kappa_{k+(n+1)p|k} - \kappa_{k+np|k} \approx 0$), and therefore it can be plausible to take action based on the current curvature. In essence this introduces a "delay" in the road curvature, but as the delay is only one prediction step, it can be considered negligible. With these assumptions, we can solve for the steering angle using the current state of the vehicle and road:

$$\mathbf{u}_{k+np|k}(1) = \frac{(\kappa_{1,k+np|k}v_{x1,k+np|k}) - \mathbf{A}_{d,k}(4,:)\mathbf{x}_{k+np|k} - \mathbf{B}_{rd,k}(4,:)\mathbf{r}_{k+np|k}}{\mathbf{B}_{ud,k}(4,1)} \tag{7.8}$$

As a finishing step, rapid changes in the steering are smoothed out to more accurately mimic the behavior of a real driver and obtain a more realistic trajectory. The smoothing is also done to remove any high-frequent components that will impact the prediction negatively. Therefore, a simple moving average filter (SMA) was implemented as a low-pass filter, where the predicted steering angle is averaged over the last three inputs according to:

$$\mathbf{u}_{SMA,k+np|k}(1) = \frac{1}{3}\sum_{i=0}^{2}\mathbf{u}_{k+np-i|k}(1) \tag{7.9}$$

Since the decision was made to use the linear model, the propulsion and braking forces no longer influence the vehicle model and are set to zero. Therefore, only the desired steering angle is computed, and the remaining set of inputs is neglected. However, if a nonlinear model had been used, the remaining propulsion forces would also need to be predicted. By just setting the forces to zero would cause prediction of the vehicle to slow down as it turns, impacting accuracy.

To test the performance of the derived simple predictive driver model, we compare it to the other scenarios with a constant steering angle and constant steering rate. A snapshot of the predicted driver input and the real inputs are presented in Figure 7.1 below to illustrate how they behave.

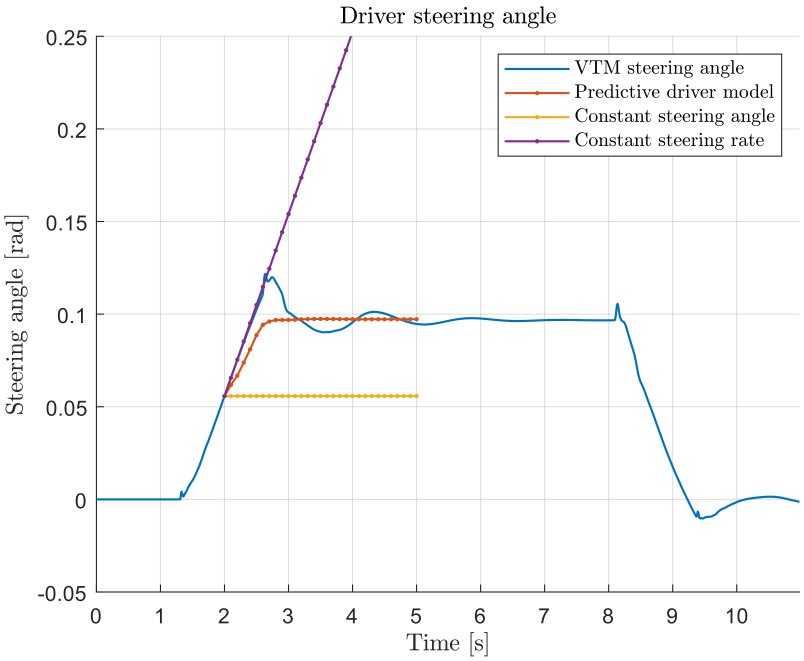

Figure 7.1: Proposed predictive driver model steering angle, compared to the VTM input, constant steering angle, and constant steering rate driver models.

The Figure summarizes the driver model´s strength and weaknesses. The constant steering model will not generate great predictions in transition periods, but is effective at steady state. The major issue is that, when the steering angle increases, the corresponding predicted lateral acceleration at the end of the horizon will be too low. In the opposite scenario, when the steering angle decreases, the predicted lateral acceleration will be to high.

The constant steering rate model can better capture the behavior during the transition periods. However, as evident in the Figure it drastically overshoots the prediction. In this scenario, the corresponding lateral acceleration would be very high and warn for dangerous scenarios when there are none. There would occur a false detection. Moreover it is extremely susceptible to noise and would require a smoothing solution to increase reliability. The horizon for the driver model would also have to be shorter to avoid any major over- or undershoots in the prediction.

The derived predictive driver model shows surprisingly good results considering its simplicity. It successfully captures the transition periods but falls short in capturing the peaks during these transitions. This discrepancy arises because the driver model in VTM is a PID-controller that has a tendency of steering to much to the road center and overshooting the reference path. A real human driver would also deviate from the lane center, which our model would fail to capture, however we can conclude that we have developed a satisfactory driver model that approximately performs as a real driver would do.

8

Predictive Threat Assessment - Stochastic Predictions

This chapter describes the methodology and functionality of the proposed predictive threat assessment method. It begins by defining the lateral acceleration limit as a stochastic limit, followed by how state, output, and uncertainty predictions are made. Next, it explains the implementation of a Kalman filter for current state estimation. The chapter then details how the risk of rollovers is quantified using joint probabilities and concludes the entire method, in an illustative block-schedule.

8.1 Defining stochastic rollover limit

As already described in Chapter 2, there is a lot of uncertainty in the vehicle parameters. Especially, in the COM height for the second unit which is used to define the rollover limit. Assuming the COM height is estimated as a Gaussian distribution, $H_k \sim \mathcal{N}\left(h_k, \sigma^2_{h,k}\right)$, we have functions to transform COM height to lateral upper and lower acceleration limits. Unfortunately, the COM height, h_k, is in the denominator of the functions which means the corresponding variance in $A_{ylim,k} \sim \mathcal{N}(a_{ylim,k}, \sigma^2_{a_{ylim},k})$ cannot be computed linearly. It also means the distribution for the limits no longer will be Gaussian.

To approximate the true distribution of the acceleration limit, one can employ Monte Carlo sampling. This involves generating random samples based on the COM height distribution and propagating these samples through the functions to produce a new output distribution. However, as long as the estimated height h_k is not close to zero and the variance is small, the acceleration limit's distribution can be approximated as a Gaussian. Either by computing the expected value and variance directly from the Monte Carlo samples, or simply by linearization around the estimated height. Given the two functions describing the lower and upper limits $f_{a_{ylim,lower}}(h_k, \lambda_{b,k})$, $f_{a_{ylim,upper}}(h_k, \lambda_{b,k})$ the transformation value, to linearly propagate the variance can be be approximated as:

$$F_{h,k} = \frac{\partial f_{a_{ylim,lower}}}{\partial h}\Big|_{h_k,\lambda_{b,k}} = \alpha_{comp}\frac{gw}{2h^2}\Big|_{h_k,\lambda_{b,k}} \tag{8.1}$$

Similarly, $F_{h,k}$ can be approximated for the upper limit, but the only difference will be a negative sign. However, when the term is squared to approximate the variance of the output, the sign will disappear. Hence, the variance of both limits will be the same. Given the two functions, the upper and lower limits and the output variance can be estimated as:

$$\begin{aligned} a_{ylim,lower,k} &= f_{a_{ylim,lower}}(h_k, \lambda_{b,k}) && (8.2)\\ a_{ylim,upper,k} &= f_{a_{ylim,upper}}(h_k, \lambda_{b,k}) && (8.3)\\ \sigma^2_{a_{ylim},k} &= F_{h,k}\sigma^2_{h,k}F^{\top}_{h,k}, && (8.4) \end{aligned}$$

Or simply expressed as Gaussian distributions:

$$\begin{aligned} A_{ylim,lower,k} &\sim \mathcal{N}\Big(a_{ylim,lower,k}, \sigma^2_{a_{ylim},k}\Big) && (8.5)\\ A_{ylim,upper,k} &\sim \mathcal{N}\Big(a_{ylim,upper,k}, \sigma^2_{a_{ylim},k}\Big) && (8.6) \end{aligned}$$

Additionally, if there is uncertainty in the road banking $\sigma^2_{\lambda_b,k}$, which is uncorrelated with the COM height, the combined uncertainty in the acceleration limit could be approximated by linearizing around $\lambda_{b,k}$:

$$F_{\lambda_b,k} = \frac{\partial f_{a_{ylim,lower}}}{\partial \lambda_b}\Big|_{h_k,\lambda_{b,k}} = \frac{\partial f_{a_{ylim,upper}}}{\partial \lambda_b}\Big|_{h_k,\lambda_{b,k}} = -g\alpha_{comp}\cos(\lambda_b) \qquad (8.7)$$

$$\begin{aligned} a_{ylim,lower,k} &= f_{a_{ylim,lower}}(h_k, \lambda_{b,k}) && (8.8)\\ a_{ylim,upper,k} &= f_{a_{ylim,upper}}(h_k, \lambda_{b,k}) && (8.9)\\ \sigma^2_{alim,k} &= F_{h,k}\sigma^2_{h,k}F^{\top}_{h,k} + F_{\lambda_b,k}\sigma^2_{\lambda_b,k}F^{\top}_{\lambda_b,k}. && (8.10) \end{aligned}$$

Although, to limit the scope of this thesis we will assume the road geometry has no uncertainty and are known.

Figure 8.1 portrays the upper acceleration limit distribution approximated by Monte Carlo Sampling and linearization. The lateral acceleration limit was generated assuming a COM height with an expected value of $h = 2.13m$, and a standard deviation of of $\sigma_h = 0.32m$. The banking was set to $\lambda_b = 0\%$. As seen in Figure 8.1, the approximated Gaussian distribution fits the true distribution rather well, and is considered sufficiently accurate to be further utilized in the PTA.

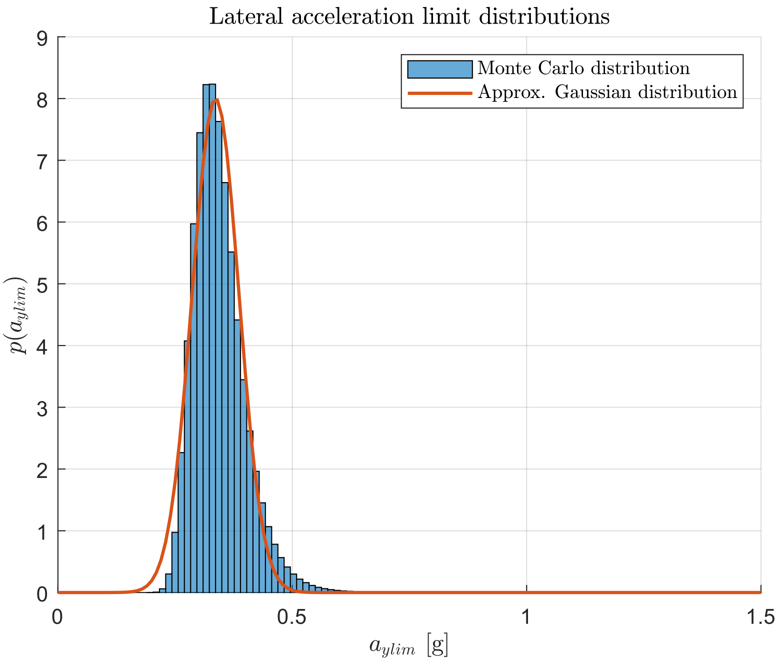

Figure 8.1: Upper lateral acceleration limit, as a stochastic variable. True distribution generated from Monte Carlo Sampling, and approximated Gaussian distribution derived from linearization.

8.2 Stochastic prediction of states and uncertainties

In accordance with modeling the defined rollover limits as stochastic, the vehicle trajectory can also be defined as a stochastic process. The equations mentioned in Chapter 5 deterministically computes how the states will change over time. However, to capture the uncertainties in the motion, it is wise to express the states and parameters as stochastic rather than deterministic. As for the rollover limits, all uncertainties in states are assumed to be Gaussian distributed. In such case we have:

$$\mathbf{X}_{k|k} \sim \mathcal{N}\Big(\mathbf{x}_{k|k}, \mathbf{P}_{k|k}\Big) \tag{8.11}$$

Where $\mathbf{X}_{k|k}$ is the stochastic states, at time $k \mid k$, described by the expected values $\mathbf{x}_{k|k}$ and the covariance matrix $\mathbf{P}_{k|k}$. Given the linear model from Equations (5.11 - 5.22), the future expected value and covariance can be predicted via a Kalman filter prediction step [39]:

$$\mathbf{x}_{k+p|k} = \mathbf{A}_{d,k}\mathbf{x}_{k|k} + \mathbf{B}_{ud,k}\mathbf{u}_{k|k} + \mathbf{B}_{rd,k}\mathbf{r}_{k|k} \tag{8.12}$$

$$\mathbf{P}_{k+p|k} = \mathbf{A}_{d,k}\mathbf{P}_{k|k}\mathbf{A}_{d,k}^{\top} + \mathbf{Q}_{k|k} \tag{8.13}$$

Equation (8.12) is the prediction of the next state, and is obtained by propagating the control inputs $\mathbf{u}_{k|k}$ and road $\mathbf{r}_{k|k}$ through the model. The predicted variance $\mathbf{P}_{k+p|k}$ is obtained from Equation (8.13) and gets an additive component $\mathbf{Q}_{k|k}$, which is the process noise at timestep k. The term $\mathbf{Q}_{k|k}$ covers the model inaccuracy, and the uncertainties in the inputs. In reality, $\mathbf{Q}_{k|k}$ is time variant and would change with the vehicle state, and the driving conditions as you get more uncertain about your position, and hence more uncertain about the road geometry and what driver will do at that location. However for simplicity we assume a constant additive process noise i.e., $\mathbf{Q}_{k|k} = \mathbf{Q}_{k+p|k} = \mathbf{Q}$.

The diagonal elements of $\mathbf{Q}$ was estimated by simulating the test manoeuvre and computing the variance of a single prediction step, giving a good representation of the model inaccuracy. This resulted in:

$$\mathbf{Q} = 10^{-4}\begin{bmatrix} 0.5945 & 0 & 0 & 0 & 0 & 0 \\ 0 & 0.1601 & 0 & 0 & 0 & 0 \\ 0 & 0 & 0.0190 & 0 & 0 & 0 \\ 0 & 0 & 0 & 0.0267 & 0 & 0 \\ 0 & 0 & 0 & 0 & 0.0030 & 0 \\ 0 & 0 & 0 & 0 & 0 & 0.0263 \end{bmatrix} \tag{8.14}$$

To include additional uncertainty of the driver acceleration and steering, as well as the road geometry, the variance of the longitudinal and lateral velocity was increased. In this way, it was concluded that a good estimation of $\mathbf{Q}$ to cover most of the uncertainty was:

$$\mathbf{Q} = 10^{-4}\begin{bmatrix} 594.5 & 0 & 0 & 0 & 0 & 0 \\ 0 & 16.01 & 0 & 0 & 0 & 0 \\ 0 & 0 & 0.0190 & 0 & 0 & 0 \\ 0 & 0 & 0 & 0.0267 & 0 & 0 \\ 0 & 0 & 0 & 0 & 0.0030 & 0 \\ 0 & 0 & 0 & 0 & 0 & 0.0263 \end{bmatrix}$$

To predict the states for a longer horizon than a single prediction step into the future, we need to consider how to do consecutive predictions. Given the predicted value, $\mathbf{x}_{k+p|k}$ and the covariance $\mathbf{P}_{k+p|k}$, one can compute the next predicted state and covariance as:

$$\mathbf{x}_{k+2p|k} = \mathbf{A}_{d,k}\mathbf{x}_{k+p|k} + \mathbf{B}_{ud,k}\mathbf{u}_{k+p|k} + \mathbf{B}_{rd,k}\mathbf{r}_{k+p|k} \tag{8.15}$$

$$\mathbf{P}_{k+2p|k} = \mathbf{A}_{d,k}\mathbf{P}_{k+p|k}\mathbf{A}_{d,k}^{\top} + \mathbf{Q}, \tag{8.16}$$

where $\mathbf{u}_{k+p|k}$, and $\mathbf{r}_{k+p|k}$ are dependent on the traveled distance $s_{k+p|k}$, and are predicted based on the driver model and the road model. Considering the case where predictions are done an arbitrary number of prediction steps, n-times into the future, the predicted states and uncertainties can be computed iteratively, by:

$$\mathbf{x}_{k+np|k} = \mathbf{A}_{d,k}^{n}\mathbf{x}_{k|k} + \sum_{i=0}^{n-1}\left(\mathbf{A}_{d,k}^{n-i}\mathbf{B}_{ud,k}\mathbf{u}_{k+ip|k} + \mathbf{A}_{d,k}^{n-i}\mathbf{B}_{rd,k}\mathbf{r}_{k+ip|k}\right) \tag{8.17}$$

$$\mathbf{P}_{k+np|k} = \mathbf{A}_{d,k}^{n}\mathbf{P}_{k|k}\mathbf{A}_{d,k}^{\top n} + \sum_{i=0}^{n-1}\mathbf{A}_{d,k}^{i}\mathbf{Q}\mathbf{A}_{d,k}^{\top i} \tag{8.18}$$

As the covariance matrix $\mathbf{P}_{k+np|k}$ only depends on the state transition matrix and the process noise, it is interesting to see how it grows over time. Figure 8.2 shows the growth in uncertainty over 30 predictions steps, corresponding to predictions $3[s]$ in to the future. $\mathbf{A}_{d,k}$ was linearized around $v_{x,k} = 12.5[m/s]$.

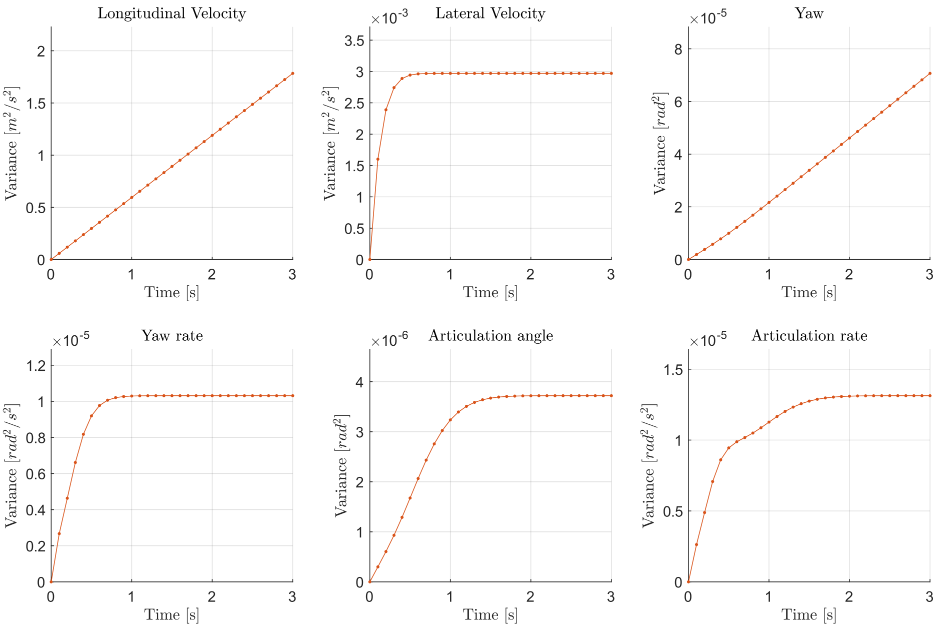

Figure 8.2: Propagtion of uncertainties through linear model over 3 second prediction horizon. Longitudinal velocity and yaw grows steadily whereas the remaining states grow at a decreasing rate.

As seen in Figure 8.2, Only the variance in longitudinal velocity and yaw increase indefinitely. However, this is expected both from a model side of view and a physical side of view. Considering the physical perspective, the vehicle can in no possible way, no matter the steering inputs, create infinite lateral velocity, or yaw rate. From a model side of view it is possible to look at the eigenvalues of $\mathbf{A}_{d,k}$, where the poles inside the unit circle is stable and will converge. For the real life case the longitudinal velocity would also converge due to resistance forces such as air resistance, which the model does not cover. It is also possible to identify that most of the model uncertainties has already reached is maximum around 1-1.5s, implying that after that time we do not get more uncertainty except for the longitudinal velocity and the yaw.

8.3 Stochastic prediction of lateral accelerations and uncertainties

Similarly to the deterministic model, the lateral accelerations can be determined using the output model. For reference, the lateral accelerations of an arbitrary prediction step is given by:

$$\mathbf{y}_{k+p|k} = g\Big(\mathbf{x}_{k+p|k}, \mathbf{u}_{k+p|k}, \mathbf{r}_{k+p|k}\Big) = \begin{bmatrix} a_{y1,k+p|k} \\ a_{y2,k+p|k} \end{bmatrix} = \begin{bmatrix} \dot{v}_{y1,k+p|k} + v_{x1,k+p|k}\dot{\phi}_{1,k+p|k} \\ \dot{v}_{y2,k+p|k} + v_{x2,k+p|k}\dot{\phi}_{2,k+p|k} \end{bmatrix} \tag{8.19}$$

$$\mathbf{y}_{k+p|k} \approx \mathbf{C}_{d,k}\mathbf{x}_{k+p|k} + \mathbf{D}_{ud,k}\mathbf{u}_{k+p|k} + \mathbf{D}_{rd,k}\mathbf{r}_{k+p|k}, \tag{8.20}$$

When the driver is operating close to the equilibrium point of the linearization, the uncertainties in lateral acceleration can be approximated as:

$$\mathbf{P}_{ay,k+p|k} = \mathbf{C}_{d,k}\mathbf{P}_{k+p|k}\mathbf{C}_{d,k}^{\top} \tag{8.21}$$

However since the linerization was performed around $\dot{\phi}_1 = 0$, the uncertainty in longitudinal velocity v_{x1} would have zero effect on the uncertainty in lateral acceleration. This is true for straight driving where speed does not affect the lateral acceleration, but in curves it is misleading since the longitudinal velocity is one of the major contributors to rollovers. To capture this behavior, a nonlinear method was chosen to model the uncertainty in lateral accelerations. Following a similar approach of an Extended Kalman filter (EKF) [39], the approximation of the uncertainty was linearized around the predicted operating point. Although, since the operating point for the acceleration consists of both states and derivatives, it was best described by the alternative output model $g(\dot{\mathbf{x}}, \mathbf{x})$.

By creating the concatenated state vector $\bar{\mathbf{x}}_{k|k} = [\mathbf{x}_{k|k}, \dot{\mathbf{x}}_{k|k}]^{\top}$, and the corresponding covariance matrix $\bar{\mathbf{P}}_{k|k}$, a new model was formed to predict the uncertainties of the outputs:

$$\bar{\mathbf{C}}_{d,k+p|k} = \left.\frac{\partial g(\bar{\mathbf{x}})}{\partial \bar{\mathbf{x}}}\right|_{\bar{\mathbf{x}}_{k+p|k}}, \tag{8.22}$$

$$\mathbf{P}_{ay,k+p|k} = \bar{\mathbf{C}}_{d,k+p|k}\bar{\mathbf{P}}_{k+p|k}\bar{\mathbf{C}}_{d,k+p|k}^{\top}. \tag{8.23}$$

However, to compute the covariance of both the states and derivatives, $\bar{\mathbf{P}}_{k|k}$, Equation (8.13) had to be adjusted. The concatenated covariance is computed according to:

$$\bar{\mathbf{P}}_{k+p|k} = \bar{\mathbf{A}}_{d,k}\bar{\mathbf{P}}_{k|k}, \bar{\mathbf{A}}_{d,k}^{\top} + \bar{\mathbf{Q}}_{k}, \tag{8.24}$$

Where

$$\bar{\mathbf{A}}_{d,k} = \begin{bmatrix} \mathbf{A}_{d,k} & 0 \\ \mathbf{A}_{c,k}\mathbf{A}_{d,k} & 0 \end{bmatrix}, \qquad \bar{\mathbf{Q}}_{k} = \begin{bmatrix} \mathbf{Q} & \mathbf{Q}\mathbf{A}_{c,k}^{\top} \\ \mathbf{A}_{c,k}\mathbf{Q} & \mathbf{A}_{c,k}\mathbf{Q}\mathbf{A}_{c,k}^{\top} \end{bmatrix}.$$

The multiplication $\mathbf{A}_{c,k}\mathbf{A}_{d,k}$ is required to predict the derivatives of the subsequent step, the same step as the discrete model. $\mathbf{A}_{c,k}\mathbf{Q}\mathbf{A}_{c,k}^\top$, is the propagated covariance of the derivatives, and the off-diagonal matrices $\mathbf{A}_{c,k}\mathbf{Q}$, and $\mathbf{Q}\mathbf{A}_{c,k}^\top$ are the covariance of the states compared to the derivatives.

8.4 Estimation of states and derivatives using an Extended Kalman Filter

Up until this point, it has been assumed that the states at present time of driving always has been known, having no uncertainty, i.e., $\bar{\mathbf{P}}_{k|k} = \mathbf{0}$, and $\mathbf{x}_{k|k} = \mathbf{x}_{VTM,k|k}$. Unfortunately, this is seldom the case in real life, where states could be difficult to measure, as well as the sensors suffering from noise. Fortunately, the vehicle models can not only be used for prediction, but also be used for a robust state estimation. Since the estimation of the vehicle is performed only once per time step, a more accurate nonlinear filter can be utilized for the estimation. Therefore, an EKF was designed for this purpose[39]. The state estimation process involves two main steps: prediction and update.

During the prediction step, the current state, the derivatives and the covariance are predicted based on the prior knowledge, $\bar{\mathbf{X}}_{k-1|k-1} \sim \mathcal{N}(\bar{\mathbf{x}}_{k-1|k-1},\ \bar{\mathbf{P}}_{k-1|\ k-1})$, $\mathbf{u}_{k-1|k-1}$, and $\mathbf{r}_{k-1|k-1}$. The prediction of the state are done according the nonlinear state space model, using Euler integration method, and the covariance is predicted by uncertainty propagation through the linearized model, similarly to Equation (8.24).

$$\mathbf{x}_{k|k-1} = \mathbf{x}_{k-1|k-1} + f(\mathbf{x}_{k-1|k-1}, \mathbf{u}_{k-1|k-1}, \mathbf{r}_{k-1|k-1})\Delta t \tag{8.25}$$

$$\dot{\mathbf{x}}_{k|k-1} = f(\mathbf{x}_{k|k-1}, \mathbf{u}_{k|k}, \mathbf{r}_{k|k}) \tag{8.26}$$

$$\bar{\mathbf{P}}_{k|k-1} = \bar{\mathbf{F}}_{d,k-1}\bar{\mathbf{P}}_{k-1|k-1},\bar{\mathbf{F}}_{d,k-1}^\top + \frac{\bar{\mathbf{Q}}_{k-1}}{10}. \tag{8.27}$$

Where

$$\bar{\mathbf{F}}_{d,k-1} = \begin{bmatrix} \mathbf{F}_{d,k-1} & 0 \\ \mathbf{A}_{c,k-1}\mathbf{F}_{d,k-1} & 0 \end{bmatrix}, \quad \bar{\mathbf{Q}}_{k-1} = \begin{bmatrix} \mathbf{Q} & \mathbf{Q}\mathbf{A}_{c,k-1}^\top \\ \mathbf{A}_{c,k-1}\mathbf{Q} & \mathbf{A}_{c,k-1}\mathbf{Q}\mathbf{A}_{c,k-1}^\top \end{bmatrix},$$

And the linearized system, $\mathbf{A}_{c,k-1}$ and $\mathbf{F}_{d,k-1}$, is derived from Equation (5.11-5.22), with sample time $\Delta t = 0.01[s]$. The discrete model for estimation is denoted $\mathbf{F}_{d,k-1}$ to distinguish from the previously mentioned discrete model $\mathbf{A}_{d,k-1}$ running at $\Delta t_{pred} = 0.1[s]$. The reason why $\bar{\mathbf{Q}}_{k-1}$ is divided by ten, is due to the shorter step size of the prediction, meaning the additive uncertainty does not increase as much as in the longer prediction steps previously mentioned. As there is no uncertainty in driver intention and road geometry at the present time, **Q** did not need to be adjusted as in (A.6).

When a measurement at time k is available the Kalman filter makes an update of its estimate. We will assume that all of the states are possible to measure, along with the longitudinal and lateral acceleration of the first unit. The measurements at time k are denoted $\mathbf{z}_k$, and are assumed to have additive white Gaussian noise, with covariance $\mathbf{R}$. The update step is performed using the nonlinear measurement model, denoted $h(\dot{\mathbf{x}}_k, \mathbf{x}_k)$. It is used to relate the predicted state to the measurements, and correct the state estimate. Given the available measurements the following model is created to predict the observations:

$$h(\dot{\mathbf{x}}_k, \mathbf{x}_k) = \begin{bmatrix} v_{x1,k} \\ v_{y1,k} \\ \phi_{1,k} \\ \dot{\phi}_{1,k} \\ \theta_{2,k} \\ \dot{\theta}_{2,k} \\ a_{x1,k} \\ a_{y1,k} \end{bmatrix} = \begin{bmatrix} \mathbf{x}(1)_k \\ \mathbf{x}(2)_k \\ \mathbf{x}(3)_k \\ \mathbf{x}(4)_k \\ \mathbf{x}(5)_k \\ \mathbf{x}(6)_k \\ \dot{\mathbf{x}}(1)_k - \mathbf{x}(2)_k\mathbf{x}(4)_k \\ \dot{\mathbf{x}}(2)_k + \mathbf{x}(1)_k\mathbf{x}(4)_k \end{bmatrix} \tag{8.28}$$

Similarly to Equations (8.22- 8.23), the measurement model is linearized around the estimated state and derivatives $\bar{\mathbf{x}}_{k|k-1}$, resulting in the linear measurement model $\bar{\mathbf{H}}_{k|k-1}$. The linear model is then used to compute the innovation covariance and the Kalman gain, which is used to update the estimated state and the covariance:

$$\bar{\mathbf{S}}_{k|k-1} = \bar{\mathbf{H}}_{k|k-1}\bar{\mathbf{P}}_{k|k-1}\bar{\mathbf{H}}_{k|k-1}^{\top} + \mathbf{R} \tag{8.29}$$

$$\bar{\mathbf{K}}_{k|k-1} = \bar{\mathbf{P}}_{k|k-1}\bar{\mathbf{H}}_{k|k-1}^{\top}\bar{\mathbf{S}}_{k|k-1}^{-1} \tag{8.30}$$

$$\bar{\mathbf{x}}_{k|k} = \bar{\mathbf{x}}_{k|k-1} + \bar{\mathbf{K}}_{k|k-1}\Big(\mathbf{z}_k - h(\dot{\mathbf{x}}_{k|k-1}, \mathbf{x}_{k|k-1})\Big) \tag{8.31}$$

$$\bar{\mathbf{P}}_{k|k} = \bar{\mathbf{P}}_{k|k-1} - \bar{\mathbf{K}}_{k|k-1}\bar{\mathbf{S}}_{k|k-1}\bar{\mathbf{K}}_{k|k-1}^{\top} \tag{8.32}$$

8.5 Quantifying the risk of rollover

When a prediction horizon for the vehicular lateral acceleration of both units has been obtained at a given timestep, a prediction of the lateral acceleration trajectories throughout the horizon and the confidence are obtained. These uncertainties can then be used to quantify the risk of a rollover over the horizon. In this thesis, the risk of rollover is defined by the joint probability distributions, of all the situations where lateral acceleration exceeds the rollover limit for any of the units.

To quantify these probabilities, we need to consider three stochastic variables for each unit and their distributions. The first stochastic variable is the estimated lateral acceleration of the vehicle unit, at an arbitrary prediction instant $k + np \mid k$ that is distributed according to the normal distribution:

$$A_{yi,k+np|k} \sim \mathcal{N}\left(a_{yi,k+np|k}, \sigma^2_{a_yi,k+np|k}\right) \tag{8.33}$$

The variances $\sigma^2_{a_y1,k+np|k}$, and $\sigma^2_{a_y2,k+np|k}$ are found from the diagonal elements of the covariance matrix $\mathbf{P}_{ay,k+np|k}$. The second and third stochastic variables are the approximated upper and lower acceleration limits for the vehicle unit respectively. The expected value of the limits is changed according to the prediction of the road geometry, but the variance stays the same.

$$A_{ylim,upper,i,k+np|k} \sim \mathcal{N}\left(a_{ylim,upper,i,k+np|k}, \sigma^2_{a_{ylim,upper},i,k}\right) \tag{8.34}$$

$$A_{ylim,lower,i,k+np|k} \sim \mathcal{N}\left(a_{ylim,lower,i,k+np|k}, \sigma^2_{a_{ylim,lower},i,k}\right) \tag{8.35}$$

From these three variables it is possible to construct two joint probabilities that are crucial to quantify the risk of a rollover. Namely: the joint probability that the vehicle unit lateral acceleration exceed the upper limit, and the joint probability that the vehicle unit lateral acceleration subceed the lower limit. These events cover the risk of a rollover occurring to either the left or the right side.

$$p(A_{ylim,upper,i,k+np|k} < A_{yi,k+np|k}) \tag{8.36}$$

$$p(A_{yi,k+np|k} < A_{lim,lower,i,k+np|k}) \tag{8.37}$$

For normally distributed variables, the problem of finding $p(A < B)$ is equivalent to finding $p(A - B < 0)$. As such, the two joint probabilities (8.36-8.37) can be evaluated with the use of cumulative distribution function (CDF) of the standard normal distribution.

$$p(A_{ylim,upper,i,k+np|k} < A_{yi,k+np|k}) = \Phi\left(\frac{a_{yi,k+np|k} - a_{ylim,upper,i,k+np|k}}{\sqrt{\sigma^2_{a_y,i,k+np|k} + \sigma^2_{a_{ylim,upper},i,k}}}\right) \tag{8.38}$$

$$p(A_{yi,k+np|k} < A_{ylim,lower,i,k+np|k}) = \Phi\left(\frac{a_{ylim,lower,i,k+np|k} - a_{yi,k+np|k}}{\sqrt{\sigma^2_{a_y,i,k+np|k} + \sigma^2_{a_{ylim,lower},i,k}}}\right) \tag{8.39}$$

As such, it is possible to quantify the risk of a rollover occuring given the uncertainty of the parameters as a probability that an event will occur. The sum of the two probabilities is the total probability that a rollover will occur in any of the possible directions:

$$p_{rollover,k+np|k} = p(A_{ylim,upper,i,k+np|k} < A_{yi,k+np|k}) + p(A_{yi,k+np|k} < A_{ylim,lower,i,k+np|k}) \tag{8.40}$$

An illustration of the two joint probabilities for an arbitrary timestep are illustrated in Figure 8.3. The part of the total volume of the ellipses that are inside the red region correspond to the probability that a rollover will occur for a given direction. The joint distribution illustrated has a 32.74 percent probability of exceeding the upper limit, and 0.00 percent probability of subceeding the lower limit. The total probability for a rollover for the given time is hence 32.74 percent. In the prediction algorithm, multiple of these joint probabilities are obtained and evaluated. As such, it is possible to quantify the threat over the entire prediction horizon. This quantification can then be used to take preventative action such as warning the driver. If the vehicle model would have no error at all, a rollover would happen when the probability exceeds 50%. As this is unlikely to be the case, the threshold in a real-life application would need to be well below that level. However selecting a suitable level for the threshold is outside the scope of this thesis.

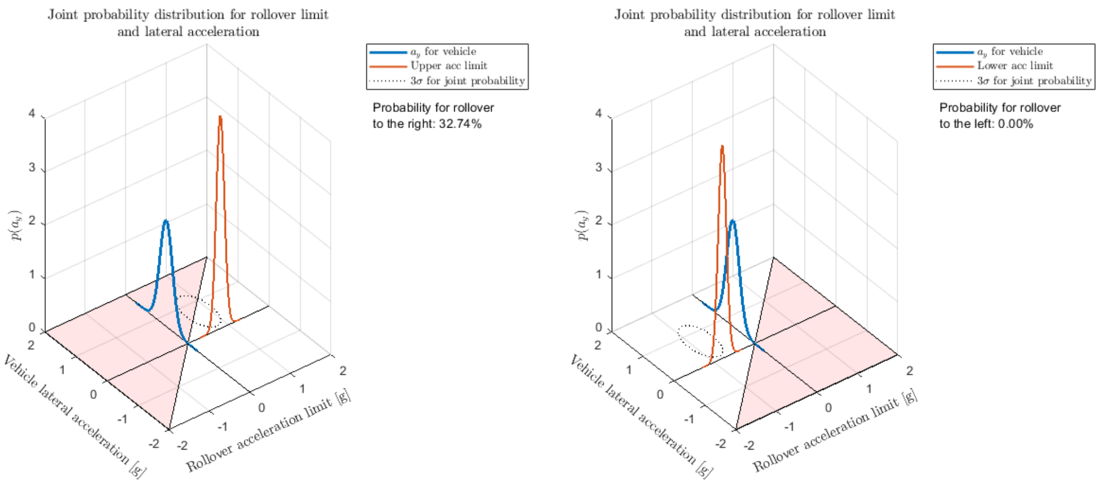

(a) Upper limit distribution

(b) Lower limit distribution

Figure 8.3: Joint probabilities for quantifying the rollover risk. The blue line represent the distribution of the vehicle lateral acceleration, and the red line represent the limit. Together these form joint probabilities illustrated by the black ellipses on the x-y plane. The red area defines the region where rollovers will occur.

8.6 Proposed Predictive Threat Assessment - Complete algorithm

The functionality of the proposed predictive threat assessment method is illustrated by the block-schedule in Figure 8.4. It shows the functionality on a higher level of abstraction.

The first blue region is the state estimator. It takes the previous state estimate, previous driver input and previous road geometry to predict what the current state is. The prediction is then updated according to the measurements available and we obtain an estimate of the current states and position. Both the expected value and the covariance.

The second yellow region is the predictor block. The first time it is run, it uses the current state estimate and distance travelled to predict the future trajectory. It takes the current state and road placement and obtains the road properties. The predicted road geometry together with the state then goes into the predicted driver block, which predicts what the input will be based on the road and the vehicle state. Thereafter the lateral accelerations distribution and the next state is predicted using the linear model. The states are then fed back to the beginning, and the process starts over, using the predicted state to derive road properties and driver inputs. This is repeated 30 times to predict the coming $3[s]$ of driving.

The last purple region describes the threat quantifier. It uses the road geometry at each prediction steps and adapts the stochastic rollover limits. This limit is then compared with the predicted lateral accelerations and computes the probability that the limit is exceeded given the confidence. The probality can then be used to trigger a safety action, such as warning the driver, or autonomously slow down the vehicle.

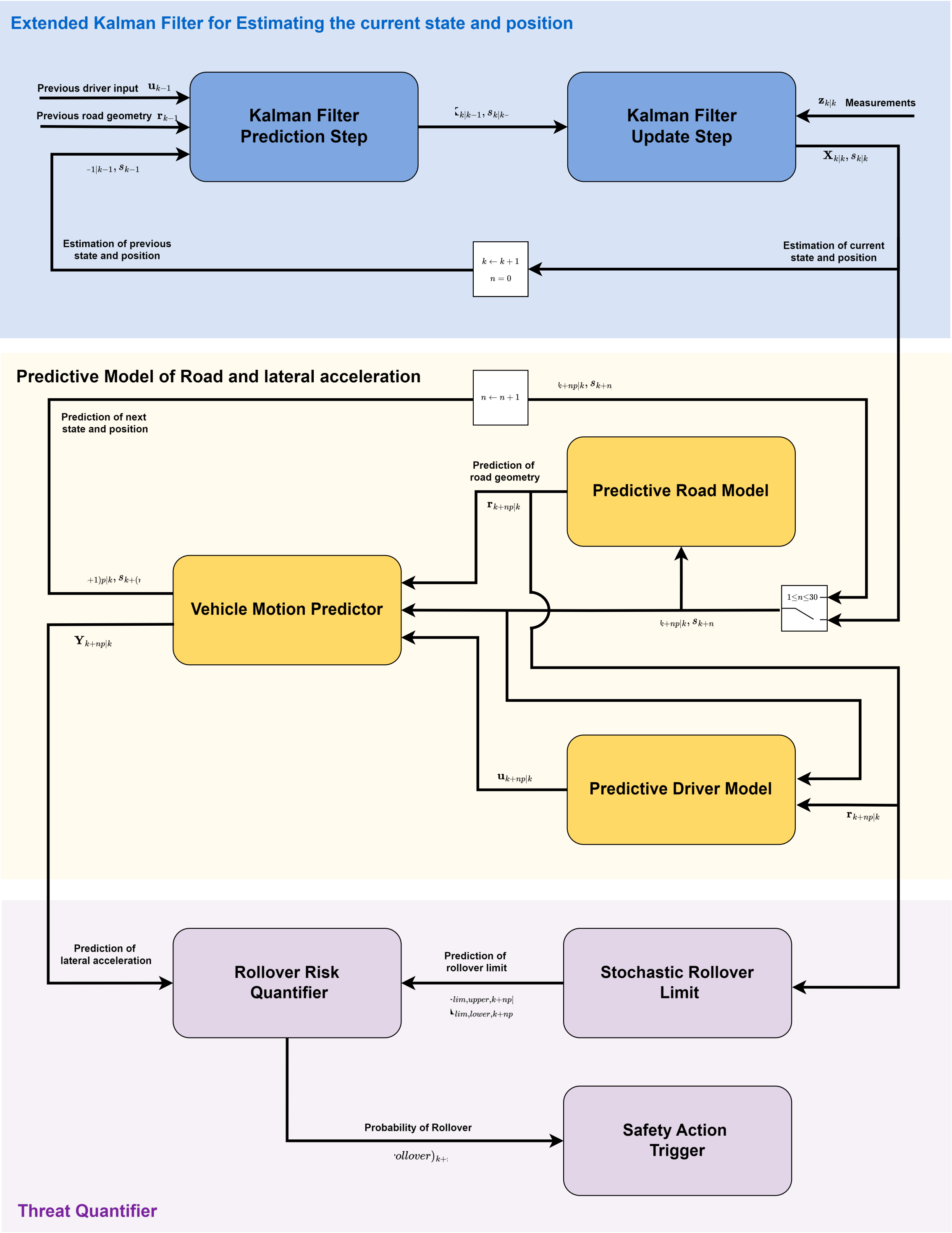

Figure 8.4: Proposed predictive threat assessment schedule.

9

Evaluation of proposed Predictive Threat Assessment method

This chapter evaluates the proposed PTA method. It presents three different test scenarios where the vehicle performs a J-turn at varying levels of banking, and the predicted lateral acceleration distributions and the rollover limits are compared. The PTA is also evaluated using a higher speed. The behavior of the driver model is then assessed for each of the three test cases. The chapter also evaluates the performance of the PTA and the EKF using real vehicle data.

9.1 Demonstration of Predictive threat assessment

In this section, we demonstrate the performance of the proposed PTA in a simulation environment. The road used is similar to the J-turn described in Chapter 6, but with three different levels of banking implemented. This allows us to evaluate both the impact on vehicle dynamics and the system's ability to detect potential threats. We will present snapshots of how the PTA perform during the entry of the curve, where potential dangers are high. The numerical vehicle parameters used are the same as the evaluation process, presented in Table C.1 in Appendix C.

9.1.1 J-turn manoeuvre on a flat road (0.0%)

Figure 9.1, shows the predicted lateral acceleration of both vehicle units on a flat road, and the $\pm 3\sigma$-confidence intervals computed by the linear approximation. The road geometry has no influence on the rollover limit, which is kept constant throughout the entire simulation.

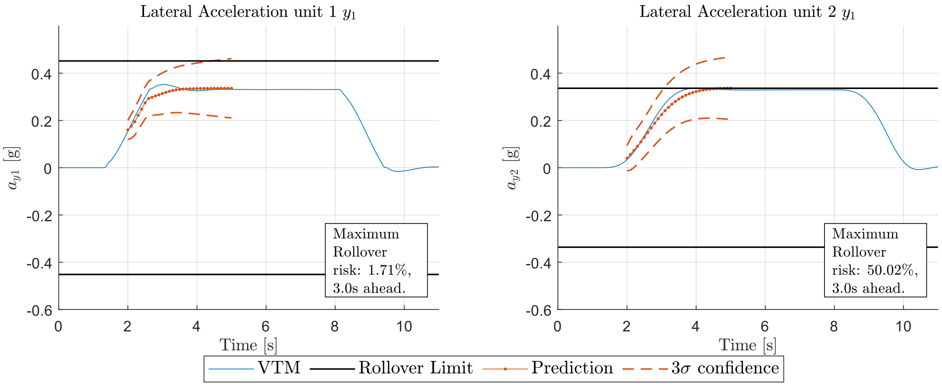

Figure 9.1: Predicted lateral accelerations and uncertainties for both vehicle units on an unbanked road. Predicted lateral acceleration is in orange with the 3 sigma confidence interval marked with dashed lines. The true accelration of the VTM is in blue and rollover limits are solid black lines.

The predicted acceleration is close to the actual accelerations of the vtm during the entire simulation. There is an overshoot in the true lateral acceleration for the first unit at around 3 seconds of simulation, which partly can be explained by the overshoot in steering angle of the VTM pathfollower, explained in Section 7.5. But it can also be explained by the roll-dynamics that generates lateral acceleration that the high-fidelity model captures. The 3σ-confidence interval of the prediction is growing throughout the prediction horizon which indicates that the uncertainty grows, which is expected for a real driver as well. It reaches its maximum uncertainty at the end of the horizon at 3 seconds. For the given time instant, the front unit detects the highest probability for a rollover 3 seconds ahead, quantified at 1.71% risk of rollover. Due to the higher COM of the trailing unit, the rollover limit for that unit is lower, and the PTA predicts that the vehicle is about to rollover. The PTA quantifies the biggest threat 3 seconds ahead at a risk of 50.02%, indicating that a safety action should be triggered. By looking at the vertical wheel forces in the VTM simulation environment, it is apparent that the vehicle was more or less riding on the outer wheels and had very little contact with the inner wheels. Despite experiencing such a large lateral load transfer, a complete wheel lift never occurs and the vehicle manages to drive through the entire turn and finish the simulation. It should be emphasised that such a manoeuvre in real life is severely dangerous, and should be avoided beforehand. Thankfully, the PTA was able to detect this risk.

9.1.2 J-turn manoeuvre on a banked curve (5.5%)

The next test was to run the high fidelity simulation on a correctly banked left turn. The results is displayed in Figure 9.2. For this test, a banking of 5.5% was used, meaning that the left-side wheels are the lower ones, according to our definition. In this case the road geometry affects the vehicle dynamics, as well as the driver inputs the SPDM generates. The approximated rollover limit is in this case adapted by considering the predicted geometry of the road.

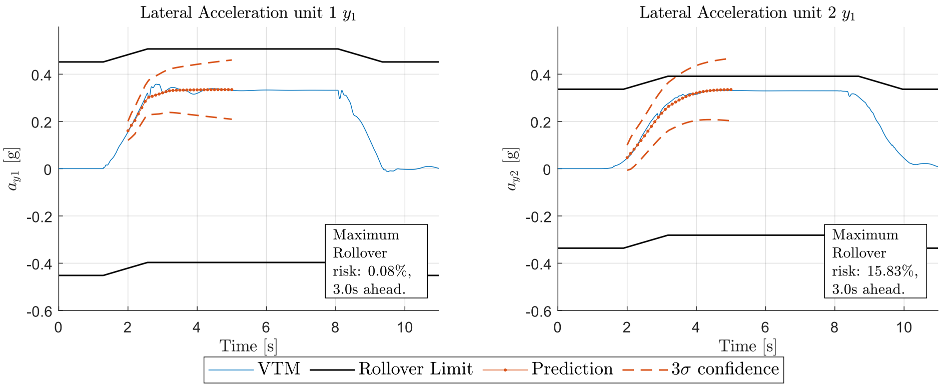

Figure 9.2: Predicted lateral accelerations and uncertainties for both vehicle units on a banked road of 5.5%. Predicted lateral acceleration is in orange with the 3 sigma confidence interval marked with dashed lines. The true accelration of the VTM is in blue and rollover limits are solid black lines.

In the case where the road is banked, it is apparent how the acceleration limits are shifted and creates larger margins between the limit and the actual accelerations. It is also apparent that the vehicle dynamics model is able to capture the effect of the road. As such, the predictive driver model also considers the geometry of the road and is still able to do plausible predictions on what the steering input and the lateral acceleration will be. For the given time instant, we can see that both the lower and upper limit is shifted upwards. They have not been shifted a lot, but the shift has changed the level of threat quite drastically. For the first unit the risk is still pretty low, just like the unbanked case. But for the second unit, the probability of rollover has decreased from 50.02% to 15.83%. This is a drastic decrease considering that the only difference is the geometry of the road. If the PTA in this case would not consider the road geometry, the threat would be quantified to a similar level as the unbanked road.

9.1.3 J-turn manoeuvre on an improperly banked curve (-2.5%)

The final simulation is on a road with -2.5% adverse banking, meaning that the road itself is not built according to Swedish standards [4]. The predicted road geometry will hence shift the limit to increase the level of risk, while at the same time requires the driver to steer more. The lateral accelerations and uncertainties can be seen in Figure 9.3 below.

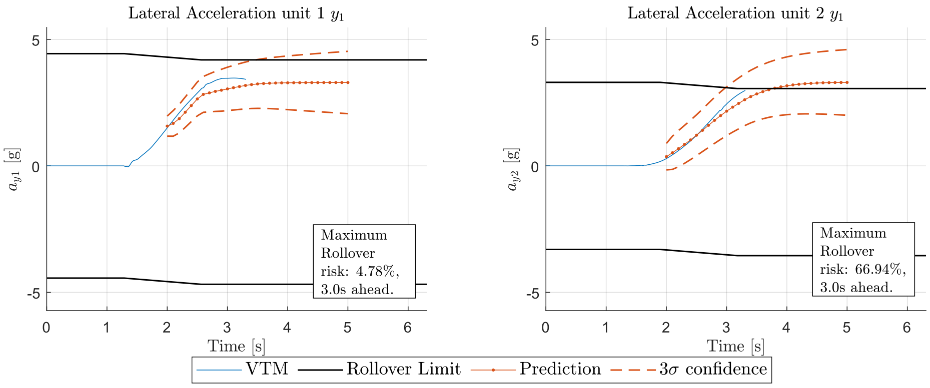

Figure 9.3: Predicted lateral accelerations and uncertaintes for both vehicle units on an improperly banked road. Predicted lateral acceleration is in orange with the 3 sigma confidence interval marked with dashed lines. The true acceleration of the VTM is in blue and rollover limits are solid black lines.

In this scenario when the road is wrongfully banked, it actually occurs a wheel lift in the simulation environment. The simulation is stopped at the time of wheel lift which occurs after 3 seconds of simulation time, but the predictive driver model still predicts a sequence of inputs to match the vehicles yaw rate with the curvature. In this case we can see that the threat for the first unit is larger, reaching a probability of rollover of 4.78%. However the second unit detects a threat of rollover with the probability reaching 66.94%, an increase of about 16 percentage units as compared to the unbanked case. If the road geometry is not consider in such a case, the predictive threat assessment will quantify the probability of a rollover to be lower than it actually is.

9.1.4 J-turn manoeuvre on banked curve at higher speed (5.5%)

To evaluate if the PTA works for more scenarios than just $44[km/h]$, it was also tested at different speeds. Figure 9.4 below shows the banked road of 5.5% being traversed by the tractor-semitrailer at a higher speed of $48[km/h]$. As seen in the Figure the VTM simulation terminates after 3 seconds as a wheel lift of the semitrailer occur. The PTA detects the maximum risk of rollover to be 65.51% two seconds ahead and are hence able to detect the impeding rollover.

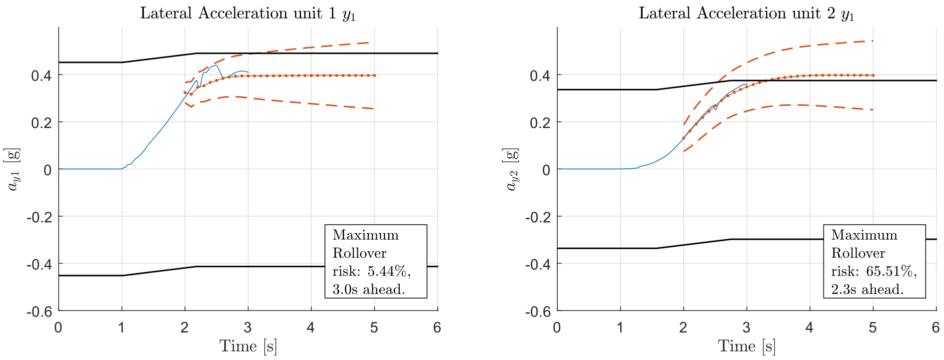

Figure 9.4: Predicted lateral accelerations and uncertainties for both vehicle units on a banked road at too high speed. Predicted lateral acceleration is in orange with the 3 sigma confidence interval marked with in dashed lines. The true accelration of the VTM is in blue and rollover limits are solid black lines.

What is common for all of these simulations is that the curve has been approached at too high speed. Even though the correctly banked road reduces the rollover risk, these driving conditions should be avoided altogether. The best way of avoiding this situation is to lower the speed of the vehicle. The probabilistic threat metric could be used for that purpose, for example if the risk of rollover exceeds 10% then the longitudinal speed could be lowered slightly. It is also possible to allow a higher risk at a later time instant, where it might be okay to have 20% risk after 3 seconds but not within 0.5 seconds, when there is less time to respond.

9.2 Evaluation of Driver model

The performance of the driver are assessed in Figure 9.5 below.

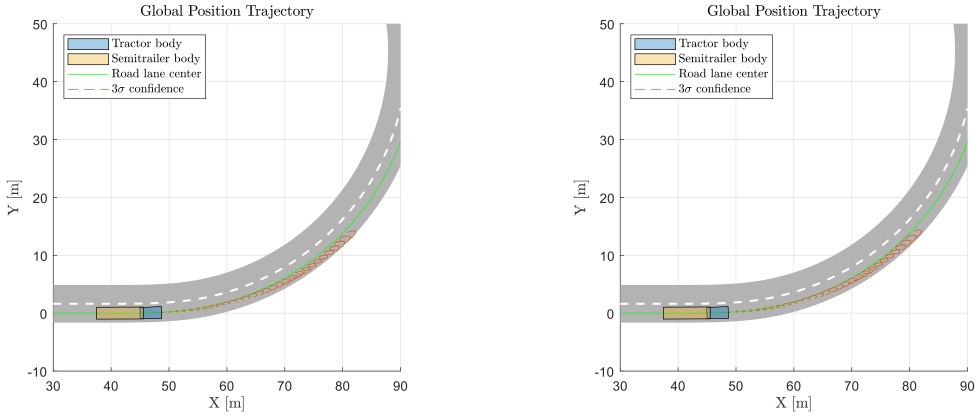

(a) Predicted position, 0.0% banking **(b)** Predicted position, −5.5% banking

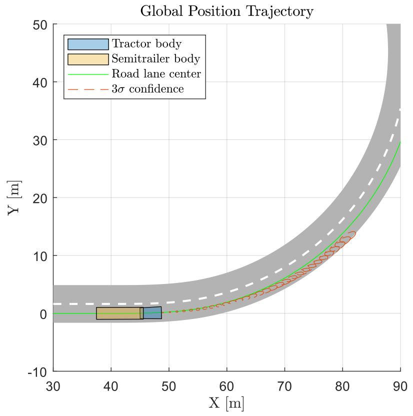

(c) Predicted position, 2.5% banking

Figure 9.5: Predicted position by the driver model for the different level of road banking at the same time instant.

As can be seen from the figures the predicted global position for the different cases are very similar. Even though the geometry of the road is altered, the SPDM is able to compute the future control sequence, while compensating for the effect of banking. In the −5.5% banked curve, the required steering angle is lower as the banking itself makes the vehicle turn. On the other hand, when the banking is improper, the required steering angle is slightly higher.

As mentioned in Section 7.5, one assumption is introduced in which the model bases its required steering angle on the current curvature, where it actually should consider the upcoming curvature in the next timestep. The effect of this assumption is shown in the figures above, where it can be seen that the predicted position is slightly off centre from the lane. This is due to the one-step delay in the curvature. As a curve starts, the predictive driver model considers this one step too late, meaning that it´s predicted steering angle will be slightly too low in each step during the transition curve. When the curvature goes back to a straight line, the predictive driver model expects the steering angle to hold and overestimates the steering slightly.

Moreover, the uncertainties in longitudinal velocity, lateral velocity and yaw have been translated into positional uncertainty. This provides an idea of where the vehicle is predicted to be in the future and whether that prediction is feasible or not. The deviation from the lane center is about $1[m]$ after 3 seconds of travel. The confidence on the lateral displacement is around $\pm 0.5[m]$. It is unclear if this trajectory covers the trajectory of what an actual driver would take, and would need to be further investigated.

9.3 Evaluation of Extended Kalman Filter

To evaluate how vulnerable the proposed PTA method was to noise, additive white random Gaussian noise was added to the deterministic data generated from the VTM, and a test on the banked road was performed once again. As seen in Figure 9.6, the EKF managed to remove almost all of the noise and still managed to follow the VTM's true state rather well. The EKF was therefore determined to work well in simulation environment where the vehicle parameters were known.

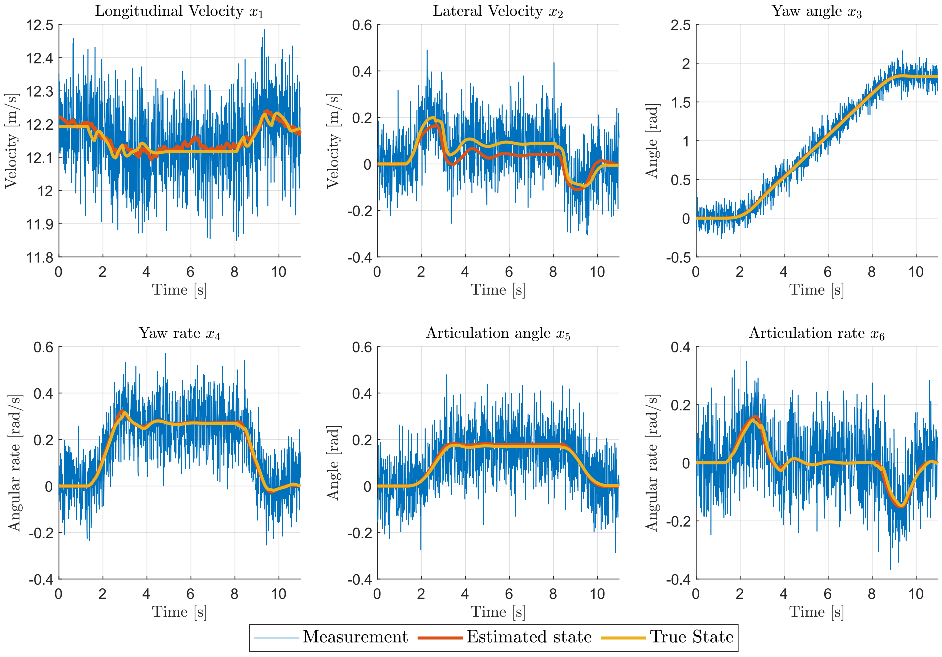

Figure 9.6: Evaluation of EKF on noisy measurement data.

9.4 Evaluation of PTA on real vehicle data

To check if the PTA could work in a real life scenario, it was also compared to real vehicle data of a tractor semitrailer combination maneuvering a circular track with $110[m]$ radius. The data was recorded using two high precision RT3000 v3 Inertial and GPS Navigation Systems, where one sensor was mounted on each unit. The test was originally performed to analyze slip and skidding of a combination vehicle and was therefore performed on packed snow. Starting from standstill the speed of the vehicle was gradually increased until skidding occurred. The decision to use this test for evaluating the EKF, instead of a more rollover-representative scenario, was based solely on having the high-accuracy RT3000 sensors at hand, especially on the second unit. Even though it would be more interesting to use the actual sensors in production vehicles, it was deemed not possible due to not all measurements, such as the articulation angle and articulation rate, being readily available. These measurements could however be synthesized from the difference in yaw and yaw rate of the front and trailing unit, explaining partly why the RT3000 INS systems needed to be used. A second reason why the high accuracy sensors was considered necessary, in the evaluation phase, was to have precise measurements of the lateral accelerations, to be considered the ground truth when validating the PTA.

Unfortunately, no road data was available for the test. However, given that the test location was known to be on a frozen lake outside of Arjeplog, Sweden, we could confidently state that no banking or road grade was evident. As for the curvature, it could simply have been estimated from the track radius. However due to the track not being a perfect circle, a curve fitting algorithm from the GPS position data would have been required to get a good estimate. Given that the test did not reflect a rollover scenario, it was settled that it would be simpler to avoid the use of the predictive driver model and instead use the real steering signal from the driver as input to the system. To get a fair evaluation of how the PTA would perform in a real life scenario, new data would therefore need to be collected. Yet, outside of the predictive context, the available test data still offered valuable insights into how the PTA, and especially the state estimation, performs.

Figure 9.7 shows the predicted lateral acceleration of the first and second unit of the vehicle compared to the measurements. Unfortunately not all the vehicle parameters, such as the yaw-moment of inertia and the center of mass, was obtainable from the test and therefore had to be estimated, using the VTM, given the known payload of 6 tonnes. The cornering stiffness of the tyres also had to be re-tuned for the model to work properly. As seen in the Figure, if the model is tuned for the specific scenario, it is possible to predict lateral accelerations of both units.

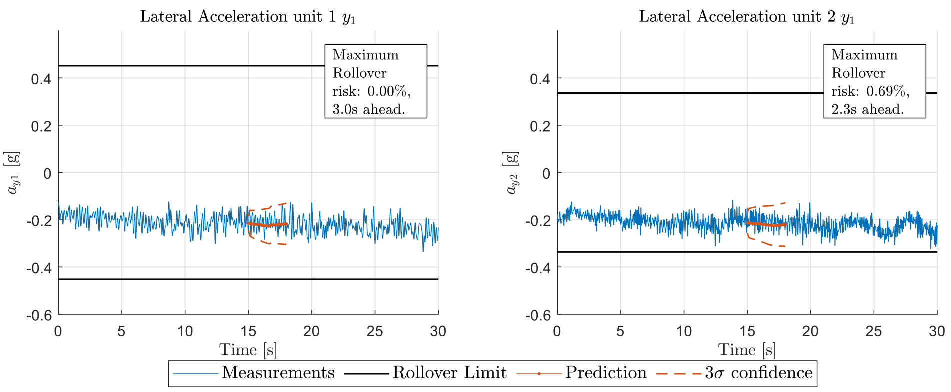

Figure 9.7: Prediction of lateral acceleration from real test data.

For the state estimation the EKF did not perform as well on real data as hoped. In particular the lateral velocity was especially hard to estimate, which can be seen in Figure 9.8. If this poor estimation was caused by slip or skidding occurring or other model errors, such as errors in the parameter estimation needs to be further evaluated. As the linear vehicle model had all eigenvalues inside the unit circle, it might physically not even be possible to reach those level of lateral velocity from the model. However, as the lateral acceleration mostly depends on the longitudinal velocity and the yaw rate, as long as those states are estimated fairly well the PTA would probably work fine. Apart from the lateral velocity most other states were reasonably well estimated. The filter managed to suppress most of the noise and gave a smooth estimate of the state. As no noise-free data of the ground truth existed it's difficult to tell how accurate the estimation was. Given the current measurement noise and process noise, one could argue that the vehicle dynamics model was trusted a bit too much, as the estimate did not follow the measurements at all times. It would therefore be compelling to review the tuning process. It is also apparent from the figure that the filter functioned the best at a specific longitudinal speed around $15 - 15.5[m/s]$, or in between $10 - 15$ seconds in the simulation. If this also is caused by model errors, or if the tire model needs to be tuned differently for varying speeds, would also be interesting to investigate.

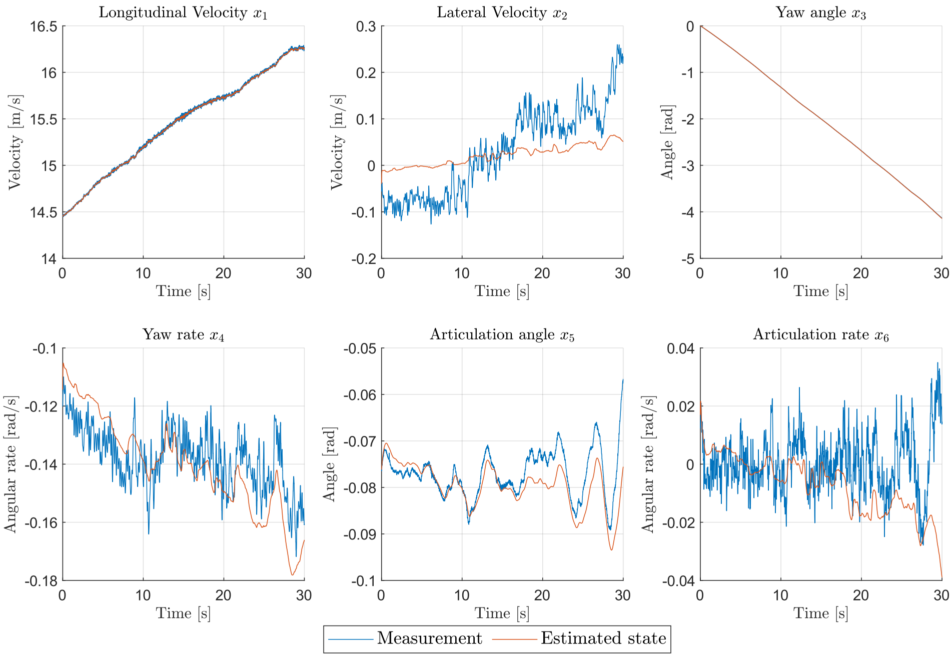

Figure 9.8: Estimated vehicle states from EKF using real test data.

10

Discussion

This chapter describes the findings of the thesis and what they imply. The strengths and limitations of the PTA is discussed, together with possible future work that could improve the research area.

10.1 Implications from the results

The PTA method proposed in this thesis has shown promising results when it comes to detecting rollover in simulation environment. We identified that the lateral acceleration and load transfer was the key variables to consider when detecting rollovers, while some researches also suggest that the vehicle roll should be considered. The predicted lateral accelerations were close to the simulated values of the high-fidelity model, and what it did not manage to capture by predictions is covered by its confidence interval.

The road could be incorporated in the PTA in three ways: In the vehicle dynamics motion model, in the driver model and in the threat metric describing the risk of rollover. The PTA was able to capture the effect of road geometry, both in the vehicle motion, and in the proposed stochastic threat metric. From the high-fidelity evaluations it was shown that our proposed lateral acceleration limits were well suited for detecting rollover risk, and can likely stand-alone in tractor-semitrailer combinations. The combination of an accurate threat metric and motion prediction algorithm can however provide additional safety, ensuring the vehicle to have enough time to slow down and prevent accidents.

The simple driver model proposed in this thesis showed improved threat assessment compared to constant steering angle and steering rate models. By incorporating the road geometry into the driver model it is possible to extend the prediction horizon of driver steering angle from a few tenths of a second to longer horizons up to 3 seconds. Incorporating the road geometry into the model also resulted in more accurate predictions and an improved threat assessment.

Except for the driver intentions, there is a lot of uncertainty in vehicle parameters, the state estimation, and in the model accuracy. By modeling the states and parameters as Gaussian distribution it is possible to account for these uncertainties. The developed PTA is flexible, meaning the level of additive uncertainty can be controlled in order to cover a larger area of possible outcomes. The PTA also allows for managing the acceptable level of risk, by controlling how often the safety action should be triggered. Since the risk of rollover is computed for each prediction step it is also possible to have varying level of acceptable risk, and trigger different actions, depending on the situation. For instance, at low levels of risk 3 seconds ahead in time, it could be sufficient to warn the driver, whereas for higher levels of risk in the imminent future the PTA could be used to trigger emergency braking. It is however unclear if the current level of additive uncertainty is enough to cover the vehicle model uncertainties, and the behaviour of what an actual driver would do in 3 seconds time. Thus even if the actual driver follows the road the PTA might miss potential rollovers.

Lastly the model is highly efficient due to the linear form and Gaussian approximations. It would most likely be possible to implement in real time on an actual tractor-semitrailer vehicle. Already as of today the simulation are done well below real time, and if the PTA was optimized on hardware it would likely be possible to achieve even faster computation times.

However, there are also some weaknesses to the proposed method. The model relies heavily on the availability of road geometry data, and the current state estimator uses measurements not readily available in production vehicles. The accuracy of the EKF is also questionable and would have to be evaluated further. Additionally, the model would not work effectively if the driver deviates significantly from the lane center. The model is flexible but not sufficiently robust to account for aggressive driver deviations and avoidance maneuvers. It is therefore only suitable for the cases where the road geometry is the main contributor to rollover. It is also ambiguous how accurate the assumption is that all uncertainties can be represented as Gaussian distributions, and that the additive uncertainty is the same during each prediction step. The true level of uncertainty would therefore need to be evaluated and compared to our approximations to evaluate how useful it is in a real life scenarios. Before the PTA would be relevant to implement on an actual vehicle, a significant amount of research would therefore need to be conducted.

10.2 Future work

As this thesis only scratches the surface of detecting rollovers in a predictive context, it highlights numerous areas that could benefit from further research. Below is a list of some identified areas that needs further exploration given our suggested approach.

- **Create a better driver model**: The predicted state trajectory is highly dependent on what sequence of control the driver model decides to take to follow the road. This thesis employs a rather basic open-loop controller that tries to remain on the road by following the curvature. As it is only controlled by the current curvature and not in any way by the future road or deviation from the center it has a tendency to drive off the road during transition curves. A more complex driver model or path follower could instead utilize more information about the road and take better planned control. As such the accuracy of the prediction would increase. Alternatively, the problem can be approached by determining whether a sequence of driver inputs exists, over a sufficiently long horizon, that prevents rollover. If no such sequence can be found, an intervention or warning can be issued to alert the driver.

- **Test model at multiple longitudinal speeds**: As this study only considers speeds around 45-50 km/h, it is not possible to answer for the model performance at other speeds. It is unclear if the linear tyre model would work the same for lower, or higher longitudinal speeds or if it would need to be adapted in some way.

- **Investigate true level of additive uncertainty:** Our proposed PTA assumes that the additive process uncertainty is Gaussian distributed and the same during the entire prediction horizon, which is definitely not the case as we get more uncertain about what the road will be and what the driver will do. The true distribution of the uncertainty, and how it increases during the prediction horizon therefore needs to be further investigated.

- **Test more manoeuvres**: The proposed method should be evaluated in more manoeuvres beyond the J-turn. Firstly, the model evaluation should be performed considering more manoeuvres, as it may be that the vehicle model is over-tuned for the specific scenario described in this study. Secondly, J-turns is not the only manoeuvre that causes rollovers and to get a fair evaluation of the performance of the PTA more scenarios needs to be considered.

- **Test different vehicle configurations**: As the study only covers a two-unit vehicle configuration in the predictive context, the study cannot answer for how the proposed method would perform for larger configurations. A suspicion is that finding the inverse of the Lagrangian when deriving the explicit form will increase the complexity, and it might be necessary to look into other models. It would also be interesting to test the proposed threat metric for more configurations. We suspect that the road geometry would influence the vehicle no matter the combination, but finding the compliance factor of the different vehicle units will likely be a challenge.

- **Real time estimation of vehicle parameters and updating the PTA**: As of now, all vehicle parameters and uncertainties has been assumed to be known. As this is not the case in real life, the parameters would need to be estimated. Especially estimating the COM height and variance real time could be of extra interest, making it possible to adapt the lateral acceleration limit under operation. As the COM height is one of the main contributors to rollover, a better estimate of the height and limits would yield a better threat assessment.

- **Investigation of driver behavior**: This thesis assumes that the driver intends to follow the road and maintain the correct heading. However, for this to be accurate the vehicle would need to be driven by a "perfect" driver. As this is not the case and a driver most likely will deviate more or less from the planed trajectory, accelerate and brake differently, the proposed method could benefit from continuously estimating how the driver behaves. The estimation of the driver behaviour could then be used to better control the uncertainty of drivers intentions. For a driver that follows the road perfectly, the distribution can be more gathered around the mean, whereas a driver that deviates a lot from the intended path, may show more unpredictable and hence more uncertain behavior.

- **Real world testing**: One major area to address is the real world testing of a refined version of the proposed algorithm. As there is no available recorded data from previous tests whose main intention was for rollover detection, with the necessary sensors on both units, it is as of now not possible to test the method. A specific test needs to be designed with the intention to gather data that could be used either online or offline to see if the proposed method can predict an initiation of a rollover. Moreover, to do real world testing the road model would need to be changed for the use of an HD map.

- **Expand model to consider multiple vehicle paths and trajectories**: As of now, the proposed method only considers one road at a time. However, the method could be elevated and be made more robust by considering multiple possible roads. An example of such an event is an intersection or a off-ramp on the highway, where the vehicle has two or more possible paths it can follow. In such case, the proposed method would evaluate the rollover risk related to the individual paths, and would have to in a clever way decide which one to trust, as describing the combined probability as Gaussian would give a poor estimate. As rollovers often happens at highway exists this is especially interesting.

11

Conclusion

This thesis work has indeed shown that it is possible to assess the risk of rollover in AHVs predictively by considering the future geometry of the road. We modelled a tractor-semitrailer using Lagrange mechanics and managed to connect the model with a road model, describing the level of banking and road grade and how it will affect the motion. This is not something many researchers have studied for combination vehicles. The road was modelled as a reference line of properties and allowed for varying levels of banking and slope, similarly to how a real road would be designed, and how it would be represented in HD maps. The proposed PTA showed promising results in simulation environment, managing to capture all the lateral accelerations of one simulated by an high-fidelity Model. However, it is unclear how well it would perform in a real-life scenario, especially the estimations of vehicle states. By modelling the vehicle dynamics as a linear model and the uncertainties as Gaussian distributions, it was possible to effectively estimate the level of risk and achieve real-time capabilities. But if these approximations are valid in reality needs to be further evaluated. We have shown that the proposed method is flexible in controlling the level of uncertainty and acceptable level of risk, but the problem of selecting suitable tuning-parameters still needs to be addressed.

Bibliography

[1] C. B. Winkler, D. Blower, and R. D. Ervin, “Rollover of Heavy Commercial Vehicles,” UMTRI-99-19, Univ. of Michigan Transportation Research Institute, Ann Arbor, MI, 1999.

[2] J. Granlund, “Feldoserade vägkurvor,” Vectura Transportarkitekt, 2013. [Online]. Available: `https://www.researchgate.net/publication/320323755_Feldoserade_vagkurvor`. [Accessed: June 13, 2024].

[3] Y. Yin, H. Wen, L. Sun, and W. Hou, "The Influence of Road Geometry on Vehicle Rollover and Skidding," *International Journal of Environmental Research and Public Health*, vol. 17, 2020.

[4] Trafikverket, "Krav - VGU, Vägars och gators utformning," TRV pubplikation 2022:001, version 1.0, pp. 56-58, 2022. [Online]. Available: `https://bransch.trafikverket.se/for-dig-i-branschen/vag/Utformning-av-vagar-och-gator/vagar-och-gators-utformning-vgu/`.

[5] J. Granlund and K. Edvardsson, "Utformning av tvärfall för minskad krängningsrisk i kurva. Uppdragsrapport till Transportstyrelsen," Transportstyrelsen, WSP Sverige AB, Version 2.0, 2016, pp. 17-19.

[6] G. J. Taylor, P.E., "Roadway Horizontal Alignment," PDH Library, 2015, pp. 20-24.

[7] J. Granlund, "Identifying 16,000 unsafe curves on state roads in Sweden," Helgums Grus AB, 2021, pp. 1-2.

[8] M. Keall and S. Newstead, "VSRG Research Program: Evaluation of ESC and SUV roll stability control," Monash University Acident Research Centre, Melbourne, 2021, pp. 22-23, vol. 1.

[9] B. Schofield, "Vehicle Dynamics Control for Rollover Prevention," Licentiate Thesis, Department of Automatic Control, Lund University, 2006.

[10] M. D. Keall and S. Newstead, "Evaluation of the effectiveness of vehicle roll stability control (RSC) for high center of gravity light passenger vehicles in Australasia," Monash University Accident Research Centre, Melbourne, 2021,

vol. 22.

[11] Y. He, X. Yan, X. Y. Lu, D. Chu, and C. Wu, "Rollover risk assessment and automated control for heavy duty vehicles based on vehicle-to-infrastructure information," *IET The Institution of Engineering and Technology*, vol. 13, 2021.

[12] L. Sun, L. Chen, Y. Yin, Y. Tian, and X. Zhang, "Risk Assessment of Rollover and Skidding due to Pavement Roughness and Differential Settlement for Enhancing Transportation Safety," *Journal of Advanced Transportation*, 2021.

[13] Y. Sellami, H. Imine, A. Boubezoul, and J. C. Cadiou, "Rollover risk prediction of heavy vehicles by reliability index and empirical modelling," *Vehicle System Dynamics*, vol. 56, no. 3, pp. 385–405, 2017.

[14] D. Hyun and R. Langari, "Modeling to Predict Rollover Threat of Tractor-Semitrailers," *Vehicle System Dynamics 39(6):401-414, International Journal of Vehicle Mechanics and Mobility*, 2010.

[15] B. C. Chen and H. Peng, "Rollover Warning for Articulated Heavy Vehicles Based on a Time-to-Rollover Metric," *ASME Journal of Dynamical Systems, Measurement, and Control*, vol. 127, no. 3, pp. 406-414, 2005.

[16] T. Chou and T. W. Chu, "An improvement in rollover detection of articulated vehicles using the grey system theory," *Vehicle System Dynamics*, vol. 52, no. 5, pp. 2014-2026, 2014. National Defence University, Taiwan.

[17] J. Dahl *et al.*, "Collision avoidance: A literature review on threat-assessment techniques," *IEEE Transactions on Intelligent Vehicles*, vol. 4, no. 1, pp. 101-113, 2018.

[18] P. Falcone, M. Ali, and J. Sjöberg, "Predictive Threat Assessment via Reachability Analysis and Set Invariance Theory," *IEEE Transactions on Intelligent Transportation Systems*, vol. 12, no. 4, pp. 1352-1361, Dec. 2011. Chalmers University of Technology.

[19] M. Brännström, F. Sandblom, and L. Hammarstrand, "A probabilistic framework for decision-making in collision avoidance systems," *IEEE Transactions on Intelligent Transportation Systems*, vol. 14, no. 2, pp. 637-648, Jun. 2013.

[20] A. Eidehall and L. Petersson, "Threat assessment for general road scenes using Monte Carlo sampling," in *Proc. 2006 IEEE Intelligent Transportation Systems Conference*, pp. 1173-1178, Oct. 2006.

[21] R. Rajamani, *Vehicle Dynamics and Control*, 2nd ed. New York, NY, USA: Springer-Verlag, Jan. 2006.

[22] M. S. Kati, "Definitions of Performance Based Characteristics for Long Heavy Vehicle Combinations," Chalmers University of Technology, Jun. 2013.

[23] G. Moreno Contreras, J. Carlos Serrano, and C. Pena Cortés, "Stability and Lateral Load Transfer in Heavy Vehicles," University of Pamplona, Colombia, 2019, *International Journal of Mechanical Engineering and Technology (IJMET)*, vol. 10, no. 12, pp. 451-459, Dec. 2019.

[24] R. Rajamani, N. Piyabongkarn, V. Tsourapas, and J. Y. Lew, "Real-Time Estimation of Roll Angle and CG Height for Active Rollover Prevention Applications," in *Proceedings of the American Control Conference*, Jan. 2009.

[25] T. Ghandriz, B. Jacobson, L. Nilsson, N. Laine, and N. Fröjd, "Computationally Efficient Nonlinear One- and Two-Track Models for Multitrailer Road Vehicles," *IEEE Access*, Oct. 2020.

[26] ISO, "ISO 8855:2011(en), Road vehicles — Vehicle dynamics and road-holding ability — Vocabulary," 2011.

[27] B. Jacobson, "Compendium in vehicle motion engineering," 2024. Chalmers University of Technology.

[28] S. Gros and B. Egardt, "Modelling and Simulation, Lecture notes for the Chalmers course ESS101," Chalmers University of Technology, Feb. 2022.

[29] S. Nedevschi, R. Schmidt, T. Graf, R. Danescu, D. Frentiu, T. Marita, F. Oniga, and C. Pocol, "3D Lane Detection System Based on Stereovision," in *Proceedings of the IEEE Intelligent Transportation Systems Conference*, Washington D.C., Nov. 2009.

[30] P. Sun, X. Zhao, Z. Xu, R. Wang, and H. Min, "A 3D LiDAR Data-Based Dedicated Road Boundary Detection Algorithm for Autonomous Vehicles," *IEEE Access*, vol. 7, pp. 21231-21240, Feb. 2019.

[31] R. Liu, J. Wang, and B. Zhang, "High Definition Map for Automated Driving: Overview and Analysis," *Journal of Navigation*, vol. 73, no. 2, pp. 324-341, Aug. 2019.

[32] HERE Technologies, "HERE HD Live Map, High-definition map content for automated driving solutions," Available: https://www.here.com/platform/HD-live-map.

[33] NHTSA, "Tractor Semi-Trailer Stability Objective Performance Test Research – Roll Stability," U.S. Department of Transportation, National Highway Traffic Safety Administration, May 2011.

[34] D. Eisele and H. Peng, "Vehicle Dynamics Control with Rollover Prevention for Articulated Heavy Trucks," University of Michigan, 2000.

[35] Y. Akhmetov, L. Laine, D. Rémond, L. Maiffredy, and V. Harth, "Predictive Driver Interpreter by Using Inverse Model for Heavy Vehicles," 2010.

[36] F. P. Bayan, A. D. Cornetto III, A. Dunn, and E. Sauer, "Brake Timing Measurements for a Tractor-Semitrailer Under Emergency Braking," *SAE International Journal of Commercial Vehicles*, vol. 118, no. 2, pp. 245-255, Oct. 2009.

[37] D. B. Fambro, R. J. Koppa, D. L. Picha, and K. Fitzpatrick, "Driver Perception-Brake Response in Stopping Sight Distance Situations," *Transportation Research Record*, vol. 1570, no. 1, pp. 1-10, 1997.

[38] A. T. van Zanten, "Evolution of Electronic Control Systems for Improving the Vehicle Dynamic Behavior," Jan 2002.

[39] Q. Li, R. Li, K. Ji, and W. Dai, "Kalman Filter and Its Application," in *Proceedings of the 8th International Conference on Intelligent Networks and Intelligent Systems (ICINIS)*, Nov. 2015.

A

one-track one-unit model derivation

The most fundamental vehicle dynamics model is the one-track one-unit model, often referred to as a bicycle model. The simplest model has two axles, with a steerable front axle and propulsion/braking forces in all wheels. An illustration of the model can be seen in Figure A.1 below.

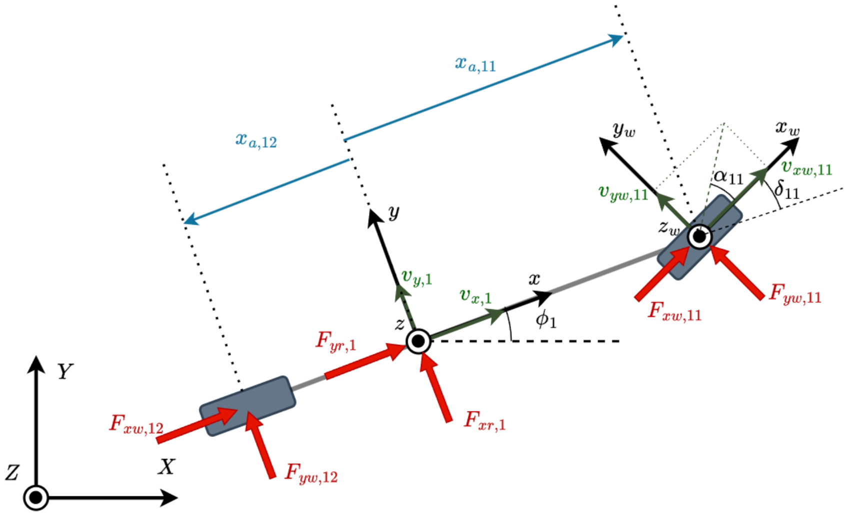

Figure A.1: Visualization of a One-Track One-Unit Model. The model is situated in the external inertia frame WCS.

The system in Figure A.1 is a one track, one unit model. It has an internal coordinate system VCS (x, y, z) (ISO8855). It has an external coordinate system WCS (X, Y, Z) and tyre coordinate system TCS (x_w, y_w, z_w). The model is traversing on a 2-dimensional plane (the X, Y plane) and rotates around the Z axis. To begin the lagrangian dynamics approach, we have to first define our generalized coordinates. For this configuration, we choose the generalized coordinates as:

$$\mathbf{q} = \begin{bmatrix} X_1 \\ Y_1 \\ \phi_1 \end{bmatrix}, \dot{\mathbf{q}} = \begin{bmatrix} \dot{X}_1 \\ \dot{Y}_1 \\ \dot{\phi}_1 \end{bmatrix}$$

Here, X_1 is the global longitudinal position of the vehicle in the WCS, Y_1 is the global latitudinal position of the vehicle in the WCS, and ϕ_1 is the yaw orientation of the vehicle in the WCS. $\dot{X}_1$ and $\dot{Y}_1$ are the global velocities, and $\dot{\phi}_1$ is the yaw rate of the vehicle. We use the subscript 1 to denote this as unit 1.

Now when the generalied coordinates are set, we need to formulate the lagrangian of the system. We start this off with defining the kinetic energy of this system. The system is traversing in the WCS, and also rotating. So we have both translational kinetic energy and rotational kinetic energy. We formulate:

$$T_1(\mathbf{q}, \dot{\mathbf{q}}) = \frac{1}{2} m_1 \left(\dot{X_1}^2 + \dot{Y_1}^2 \right) + \frac{1}{2} I_{zz,1} \dot{\phi_1}^2 \tag{A.1}$$

Where m_1 is the mass of the unit and $I_{zz,1}$ is the moment of inertia of the unit around the z-axis of rotation.

The potential energy of the system is present in the springs and also in the height of the center of the mass. However, since we only model a planar dynamics model, there is no dimension for the height. We do not model the suspension so there is no potential energy stored in springs or dampers. Even if we did model the potential energy, the magnitude would be negligable in relation to the magnitude of kinetic energy at higher velocities. Hence we include the assumption that:

$$V_1(\mathbf{q}) \approx 0 \tag{A.2}$$

We can now obtain the Lagrangian for this unit as:

$$\begin{aligned} \mathcal{L}(\mathbf{q}, \dot{\mathbf{q}}) &= T_1(\mathbf{q}, \dot{\mathbf{q}}) - V_1(\mathbf{q}) && \text{(A.3)} \\ &= \frac{1}{2} m_1 (\dot{X_1}^2 + \dot{Y_1}^2) + \frac{1}{2} I_{zz,1} \dot{\phi_1}^2 && \text{(A.4)} \end{aligned}$$

Continuing the model derivation, we now have to consider how the external forces act on the system, i.e. we need to define the generalized forces $\mathbf{Q}$. We do so by determining the components of:

$$\mathbf{Q} = \begin{bmatrix} Q_{X_1} \\ Q_{Y_1} \\ Q_{\phi_1} \end{bmatrix} \tag{A.5}$$

The generalized forces $\mathbf{Q}$ have to be expressed in the same coordinate system as the generalized coordinates $\mathbf{q}$, i.e. the WCS. Since we have a set och forces $\mathbf{F}_{1,\ldots,n_F}$ acting on the system on a set of points $\mathbf{p}_{1,\ldots,n_F}$, where n_F is the amount of forces and positions, we can formulate the generalized forces according to:

$$\mathbf{Q} = \sum_{i=1}^{n_F} \frac{\partial \mathbf{p}_i^\top}{\partial \mathbf{q}} \mathbf{F}_i \tag{A.6}$$

For this vehicle configuration, we have the forces acting on the front wheels $\mathbf{F_1}$, the rear wheels $\mathbf{F_2}$, and the forces acting on the COM, due to the road profile $\mathbf{F_3}$.

$$\mathbf{F}_1 = M_{WCS}^{VCS}(\phi_1) M_{VCS}^{TCS}(\delta_1 1) \begin{bmatrix} F_{xw,11} \\ F_{yw,11} \end{bmatrix} \tag{A.7}$$

$$\mathbf{F}_2 = M_{WCS}^{VCS}(\phi_1) \begin{bmatrix} F_{xw,12} \\ F_{yw,12} \end{bmatrix} \tag{A.8}$$

$$\mathbf{F}_3 = M_{WCS}^{VCS}(\phi_1) \begin{bmatrix} F_{xr,1} \\ F_{yr,1} \end{bmatrix} \tag{A.9}$$

Here the forces has been expressed in the WCS, the same as our generalized coordinates. The lateral forces generated by the tyres can be reformulated according to a linear or non-linear tyre model. By doing so, the lateral wheel forces are expressed in terms of $v_{x,w}, v_{y,w}$ and δ_1 instead. To find the corresponding global positions of the forces, one can use the length from COM to the axles x_a and apply a rotation. Note that axles positioned behind the COM, e.g x_a12 has negative length.

$$\mathbf{p}_1 = \begin{bmatrix} X_1 \\ Y_1 \end{bmatrix} + M_{WCS}^{VCS} \begin{bmatrix} x_{a11} \\ 0 \end{bmatrix} \tag{A.10}$$

$$\mathbf{p}_2 = \begin{bmatrix} X_1 \\ Y_1 \end{bmatrix} + M_{WCS}^{VCS} \begin{bmatrix} x_{a12} \\ 0 \end{bmatrix} \tag{A.11}$$

$$\mathbf{p}_3 = \begin{bmatrix} X_1 \\ Y_1 \end{bmatrix} \tag{A.12}$$

The generalized forces $\mathbf{Q}$ can then be computed according to (A.6), and we have sufficient expressions to formulate the Euler-Lagrange equation for the system.

$$\frac{d}{dt} \frac{\partial \mathcal{L}}{\partial \dot{\mathbf{q}}} - \frac{\partial \mathcal{L}}{\partial \mathbf{q}} = \mathbf{Q} \tag{A.13}$$

However, in vehicle dynamics it is often more interesting to express the dynamics in terms of variables in the inertial reference frame VCS instead of the external WCS, Due to driver inputs and vehicle states being measured in that frame of reference. This means that we want to express the Euler-Lagrange Equation (3.29) in terms of v_{x1}, v_{y1} and local wheel forces $F_w x$ instead of global forces. Due to the Pythagorean identity, the Lagrangian function (3.13) can be expressed in the form of local velocities as:

$$\mathcal{L}(v_{x1}, v_{y1}, \dot{\phi}_1) = \frac{1}{2} m_1 \left(v_{x1}^2 + v_{y1}^2 \right) + \frac{1}{2} I_{zz,1} \dot{\phi_1}^2, \tag{A.14}$$

To go from the velocities in WCS to VCS, a rotation is applied:

$$\begin{bmatrix} v_{x1} \\ v_{y1} \end{bmatrix} = M_{VCS}^{WCS}(\phi_1) \begin{bmatrix} \dot{X}_1 \\ \dot{Y}_1 \end{bmatrix}, \tag{A.15}$$

This means that $v_{x,1}$ and $v_{y,1}$ will be expressed as a functions of $\dot{X}_1, \dot{Y}_1$ and ϕ_1. Therefore chain rule differentiation needs to be performed on the Euler-Lagrange expression to evaluate it accordingly.

$$\frac{\partial \mathcal{L}}{\partial \dot{X}_1} = \frac{\partial \mathcal{L}}{\partial v_{x1}} \frac{\partial v_{x1}}{\partial \dot{X}_1} + \frac{\partial \mathcal{L}}{\partial v_{y1}} \frac{\partial v_{y1}}{\partial \dot{X}_1} = \frac{\partial \mathcal{L}}{\partial v_{x1}} \cos(\phi_1) - \frac{\partial \mathcal{L}}{\partial v_{y1}} \sin(\phi_1) \tag{A.16}$$

$$\frac{\partial \mathcal{L}}{\partial \dot{Y}_1} = \frac{\partial \mathcal{L}}{\partial v_{x1}} \frac{\partial v_{x1}}{\partial \dot{Y}_1} + \frac{\partial \mathcal{L}}{\partial v_{y1}} \frac{\partial v_{y1}}{\partial \dot{Y}_1} = \frac{\partial \mathcal{L}}{\partial v_{x1}} \sin(\phi_1) + \frac{\partial \mathcal{L}}{\partial v_{y1}} \cos(\phi_1) \tag{A.17}$$

$$\frac{\partial \mathcal{L}}{\partial \phi_1} = \frac{\partial \mathcal{L}}{\partial v_{x1}} \frac{\partial v_{x1}}{\partial \phi_1} + \frac{\partial \mathcal{L}}{\partial v_{y1}} \frac{\partial v_{y1}}{\partial \phi_1} = \underbrace{\frac{\partial \mathcal{L}}{\partial v_{x1}}}_{A} v_{y1} - \underbrace{\frac{\partial \mathcal{L}}{\partial v_{y1}}}_{B} v_{x1}, \tag{A.18}$$

And the last terms of the LHS of the Euler-Lagrange equations will remain:

$$\frac{\partial \mathcal{L}}{\partial \dot{\phi}_1} = I_{zz} \dot{\phi}_1, \tag{A.19}$$

$$\frac{\partial \mathcal{L}}{\partial X_1} = 0, \tag{A.20}$$

$$\frac{\partial \mathcal{L}}{\partial Y_1} = 0 \tag{A.21}$$

The time derivatives $\frac{d}{dt}\frac{\mathcal{L}}{\dot{\mathbf{q}}}$ can hence be derived by the product rule as:

$$\frac{d}{dt}\frac{\mathcal{L}}{\dot{X}_1} = -A\sin(\phi_1)\dot{\phi}_1 + \dot{A}\cos(\phi_1) - B\cos(\phi_1)\dot{\phi}_1 - \dot{B}\sin(\phi_1) \tag{A.22}$$

$$\frac{d}{dt}\frac{\mathcal{L}}{\dot{Y}_1} = A\cos(\phi_1)\dot{\phi}_1 + \dot{A}\sin(\phi_1) - B\sin(\phi_1)\dot{\phi}_1 + \dot{B}\cos(\phi_1) \tag{A.23}$$

$$\frac{d}{dt}\frac{\mathcal{L}}{\dot{\phi}_1} = I_{zz}\ddot{\phi}_1, \tag{A.24}$$

Or in VCS with the rotation $M_{VCS}^{WCS}(\phi_1)$, it can simply be expressed as:

$$\frac{d}{dt}\frac{\mathcal{L}}{v_{x1}} = \dot{A} - B\dot{\phi}_1 \tag{A.25}$$

$$\frac{d}{dt}\frac{\mathcal{L}}{v_{y1}} = \dot{B} + A\dot{\phi}_1 \tag{A.26}$$

$$\frac{d}{dt}\frac{\mathcal{L}}{\dot{\phi}_1} = I_{zz}\ddot{\phi}_1, \tag{A.27}$$

At this point, we have expressed the LHS of the Euler-Lagrange equation in terms of variables in the vehicle unit. Now, we need to do the same for the generalized forces $\mathbf{Q}$:

$$\mathbf{Q}_{VCS} = \begin{bmatrix} Q_{x1} \\ Q_{y1} \\ Q_{\phi_1} \end{bmatrix} = \begin{bmatrix} M_{VCS}^{WCS}(\phi_1)\begin{bmatrix} Q_{X_1} \\ Q_{Y_1} \end{bmatrix} \\ Q_{\phi_1} \end{bmatrix} \tag{A.28}$$

$$\mathbf{Q}_{VCS} = \begin{bmatrix} Q_{x1} \\ Q_{y1} \\ Q_{\phi_1} \end{bmatrix} = \begin{bmatrix} M_{VCS}^{WCS}(\phi_1) & \mathbf{0}_{2\times 1} \\ \mathbf{0}_{1\times 2} & \mathbf{I}_{1\times 1} \end{bmatrix} \begin{bmatrix} Q_{X_1} \\ Q_{Y_1} \\ Q_{\phi_1} \end{bmatrix} \tag{A.29}$$

$$\mathbf{Q}_{VCS} = \begin{bmatrix} Q_{x1} \\ Q_{y1} \\ Q_{\phi_1} \end{bmatrix} = \begin{bmatrix} M_{VCS}^{WCS}(\phi_1) & \mathbf{0}_{2\times 1} \\ \mathbf{0}_{1\times 2} & \mathbf{I}_{1\times 1} \end{bmatrix} \mathbf{Q}_{WCS} \tag{A.30}$$

And finally, if we define the state vector as $x = [v_{x1}, v_{y1}, \phi_1]^\top$, the input vector as $u = [\delta_{11}, F_{xw11}, F_{xw12}]^\top$, and the road properties as $r = [\lambda_{b1}, \lambda_{s1}]^\top$, we obtain the implicit equations of motion EOM:

$$F(x, \dot{x}, u, r) = 0 = \begin{cases} \dot{A} - B\dot{\phi}_1 - Q_{x1} \\ \dot{B} + A\dot{\phi}_1 - Q_{y1} \\ I_{zz}\ddot{\phi}_1 - Av_{y1} + Bv_{x1} - Q_{\phi_1} \end{cases} \tag{A.31}$$

B

Evaluation figures for vehicle dynamic models

B.1 State trajectory and output plots for $\Delta t = 0.01$

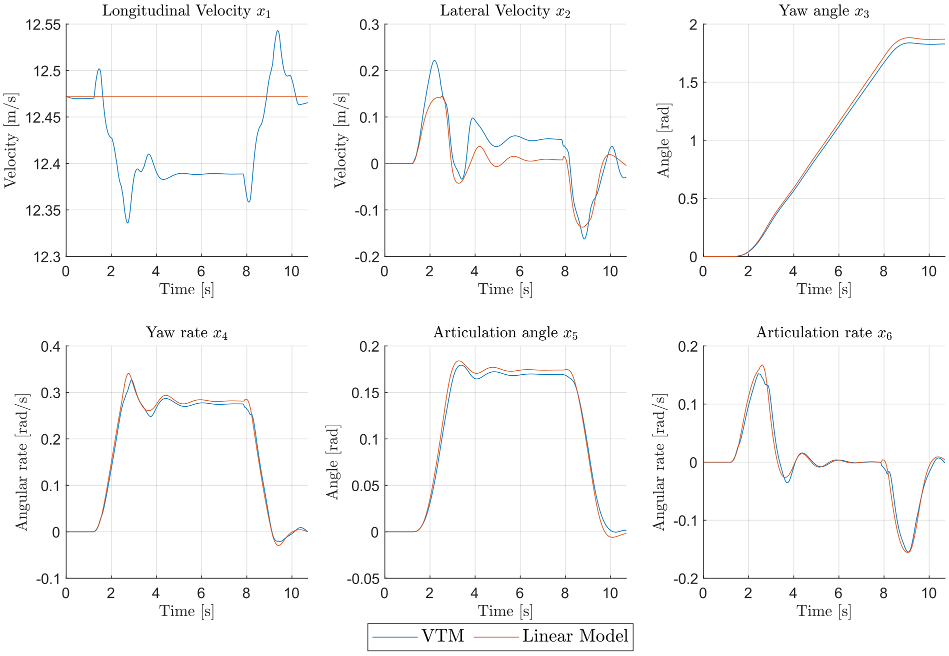

Figure B.1: Vehicle model states from evaluation. Linear model. $\Delta t = 0.01[s]$.

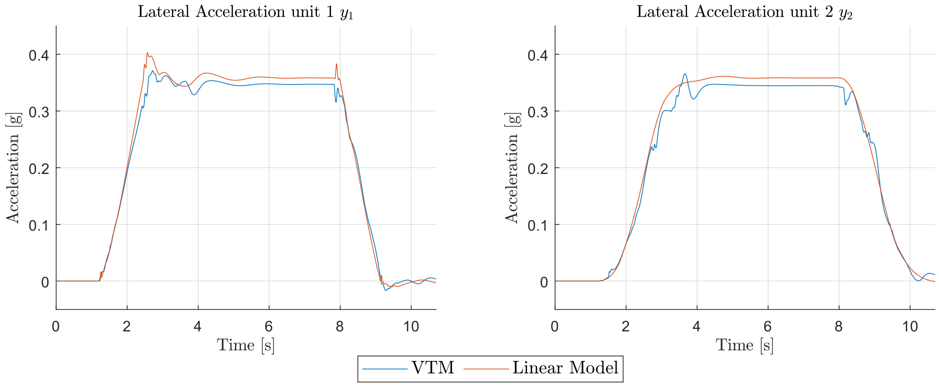

Figure B.2: Vehicle model outputs. Linear model. $\Delta t = 0.01[s]$.

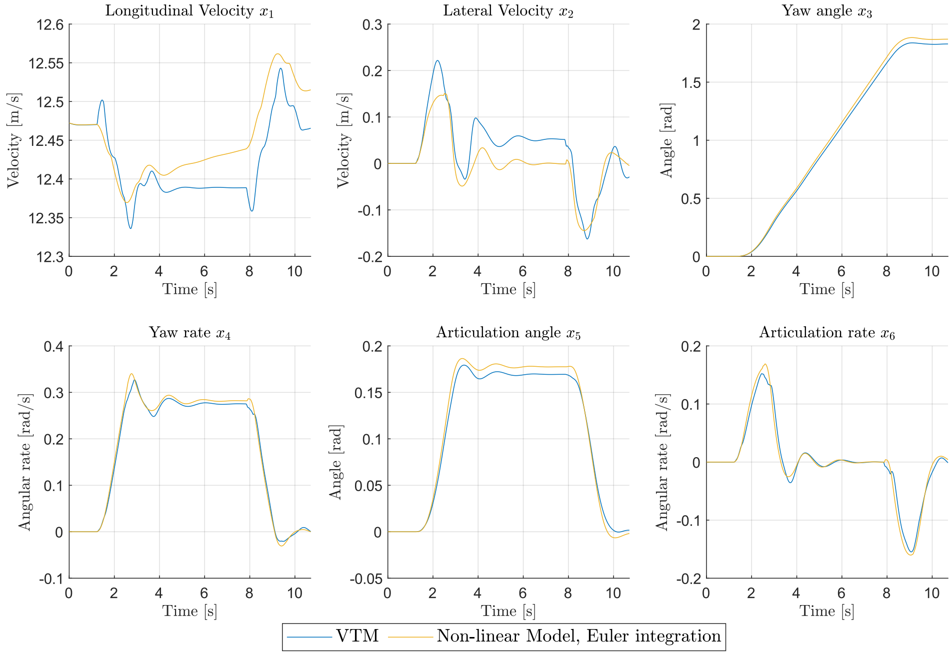

Figure B.3: Vehicle model states from evaluation. Non-linear model with forward Euler integration. $\Delta t = 0.01[s]$.

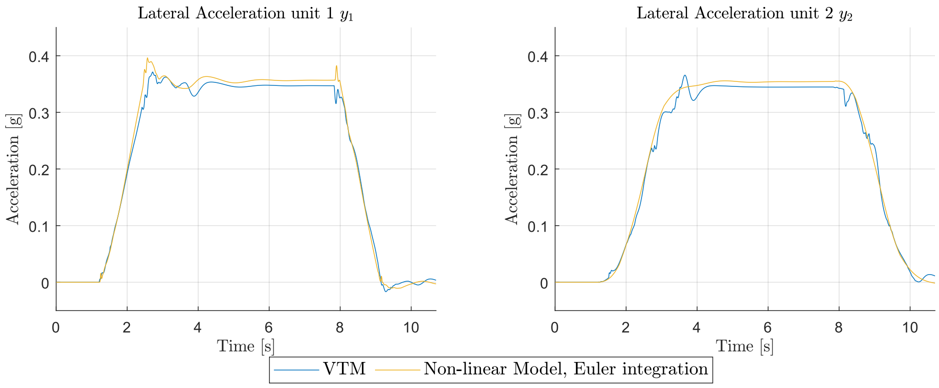

Figure B.4: Vehicle model outputs. Non-linear model with forward Euler integration. $\Delta t = 0.01[s]$.

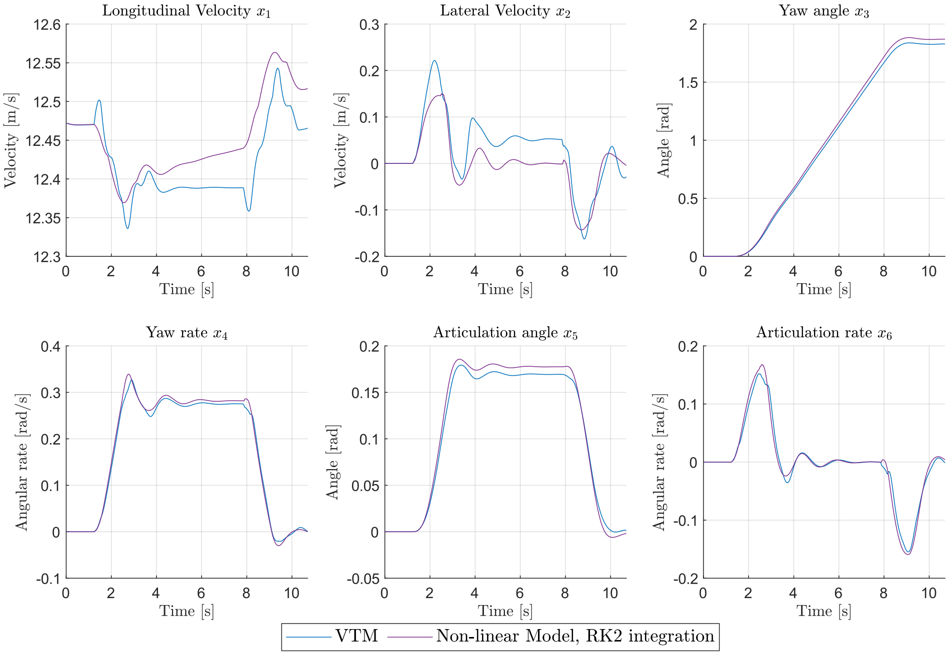

Figure B.5: Vehicle model states from evaluation. Non-linear model with RK2 integration. $\Delta t = 0.01[s]$.

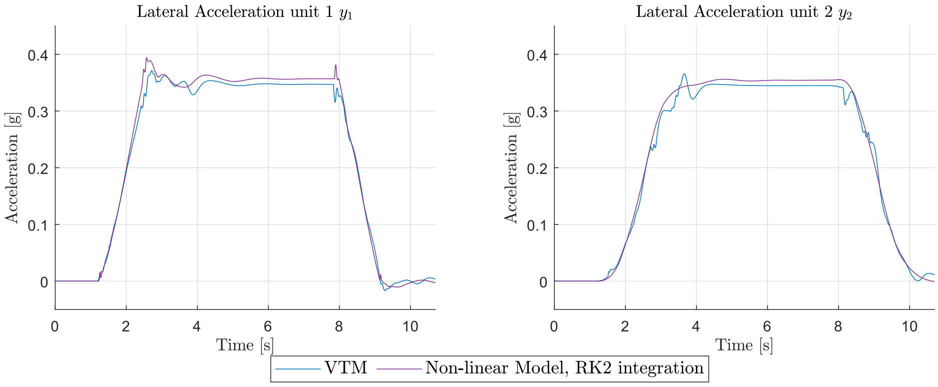

Figure B.6: Vehicle model outputs. Non-linear model with RK2 integration. $\Delta t = 0.01[s]$.

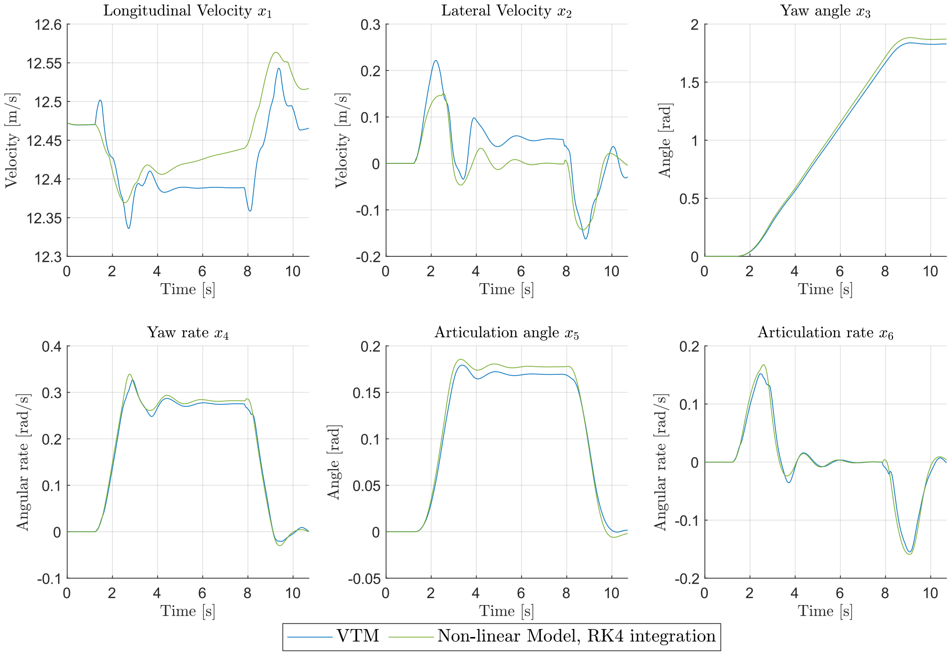

Figure B.7: Vehicle model states from evaluation. Non-linear model with RK4 integration. $\Delta t = 0.01[s]$.

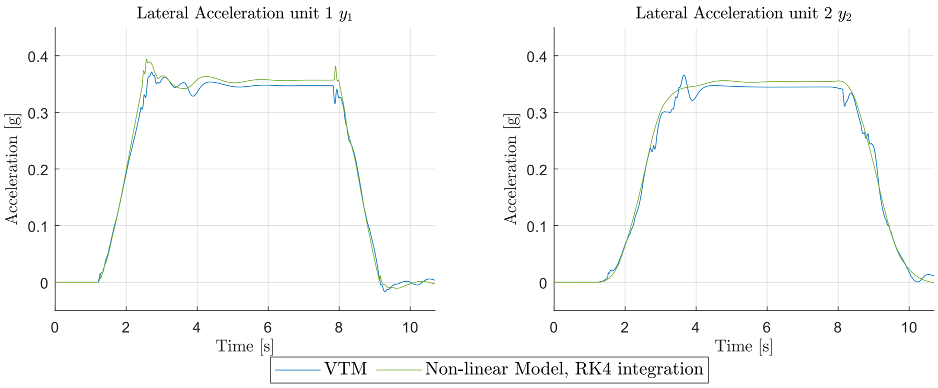

Figure B.8: Vehicle model outputs. Non-linear model with RK4 integration. $\Delta t = 0.01[s]$.

B.2 State trajectory and output plots for $\Delta t = 0.1$

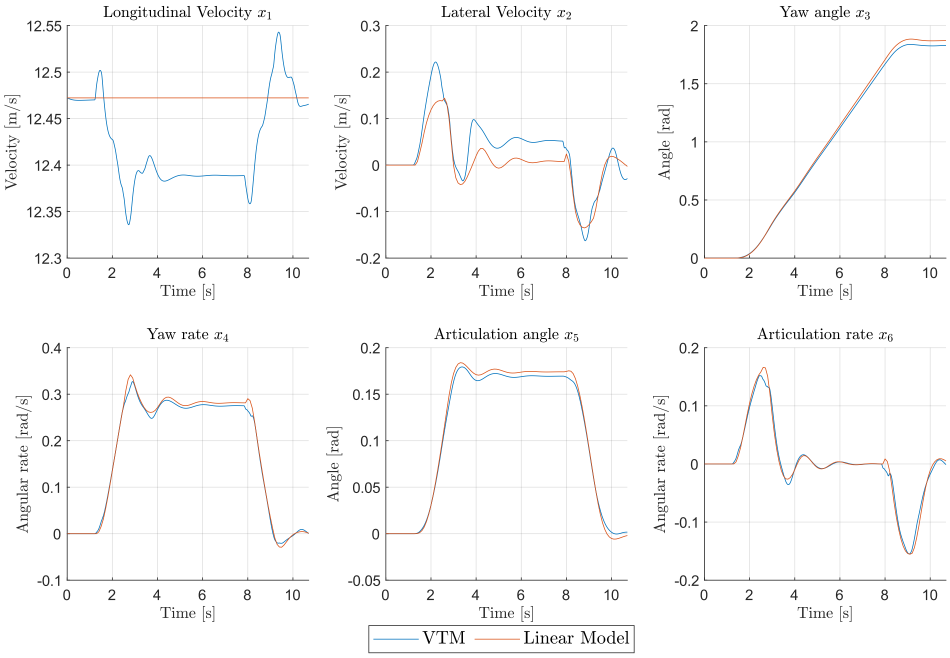

Figure B.9: Vehicle model states from evaluation. Linear model. $\Delta t = 0.1[s]$.

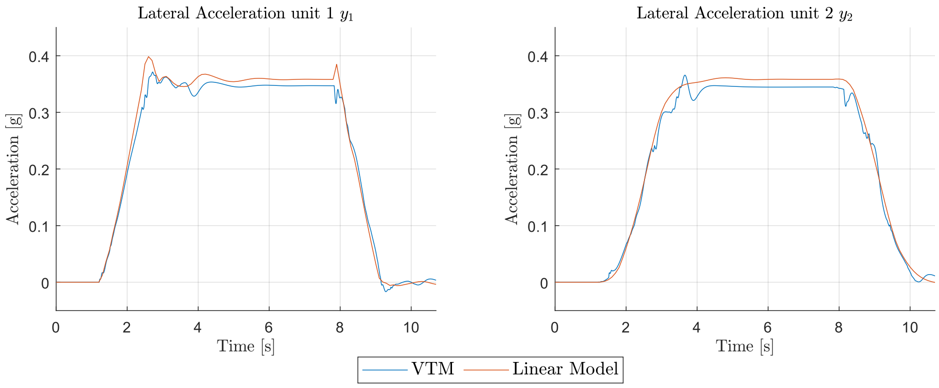

Figure B.10: Vehicle model outputs. Linear model. $\Delta t = 0.1[s]$.

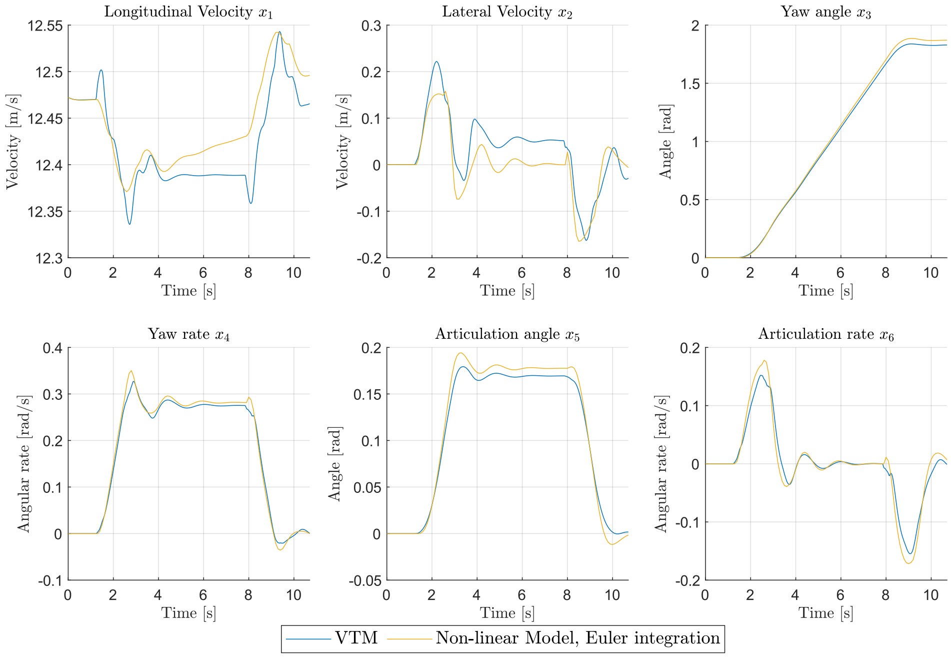

Figure B.11: Vehicle model states from evaluation. Non-linear model with forward Euler integration. $\Delta t = 0.1[s]$.

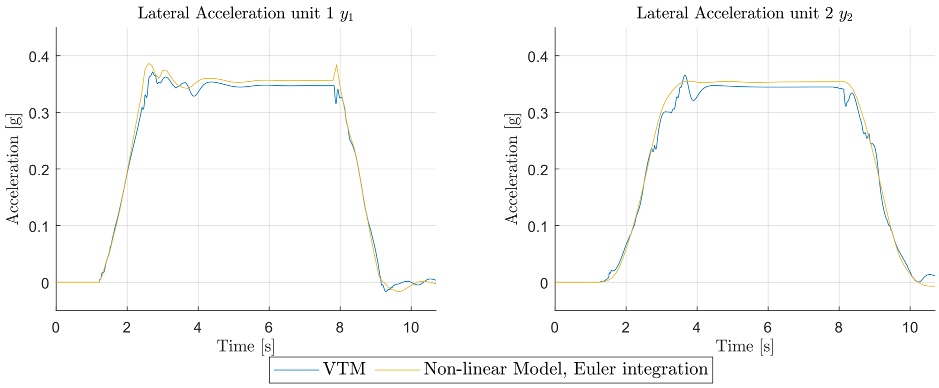

Figure B.12: Vehicle model outputs. Non-linear model with forward Euler integration. $\Delta t = 0.1[s]$.

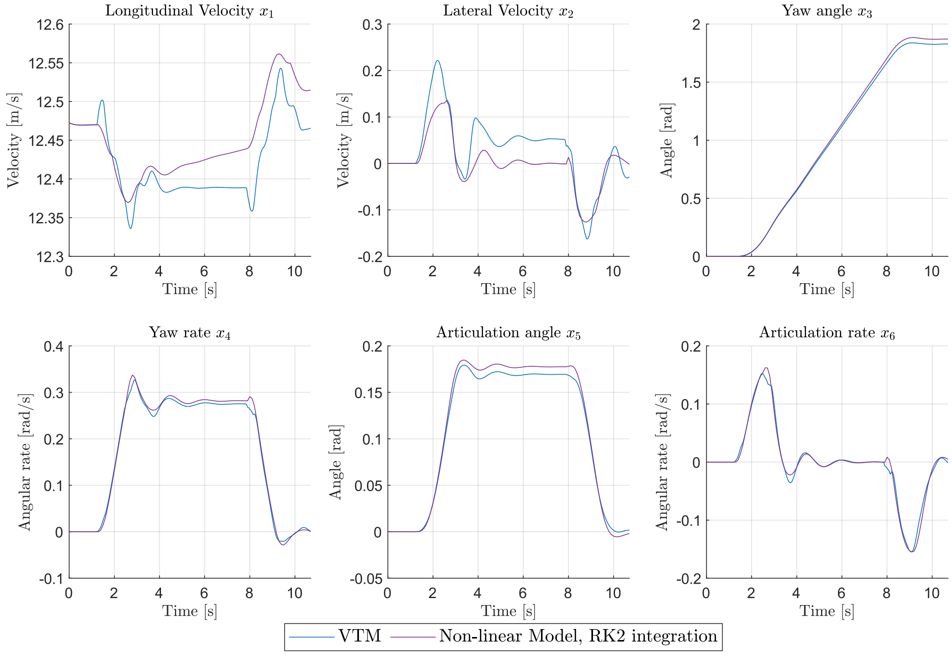

Figure B.13: Vehicle model states from evaluation. Non-linear model with RK2 integration. $\Delta t = 0.1[s]$.

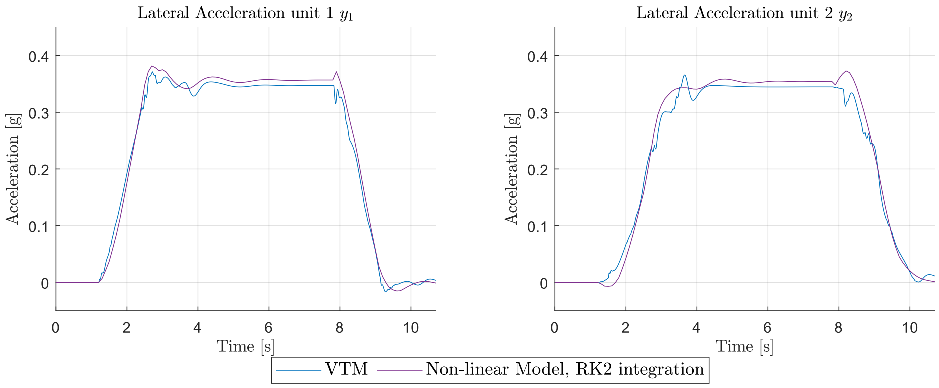

Figure B.14: Vehicle model outputs. Non-linear model with RK2 integration. $\Delta t = 0.1[s]$.

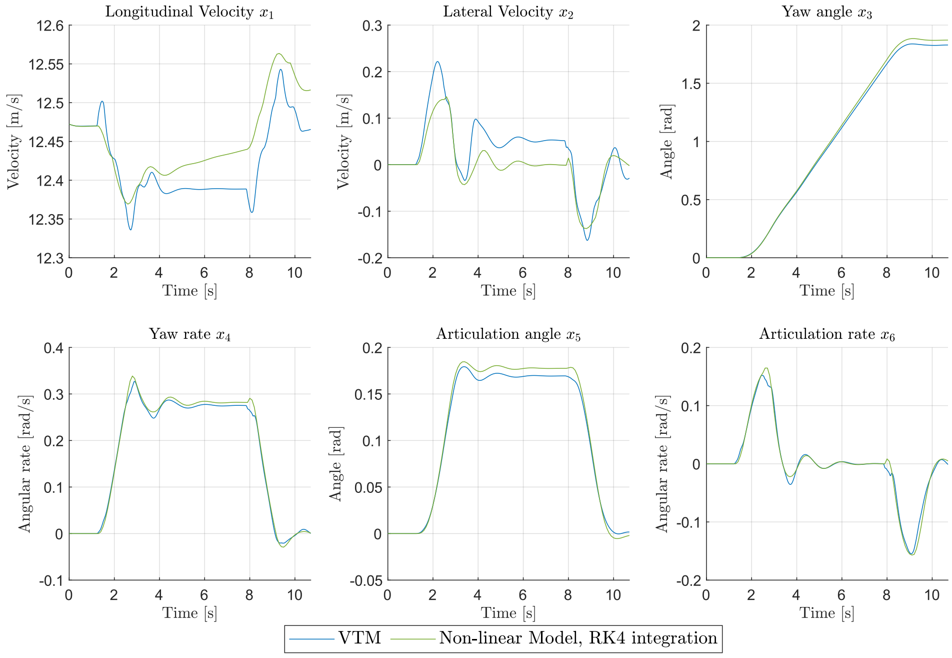

Figure B.15: Vehicle model states from evaluation. Non-linear model with RK4 integration. $\Delta t = 0.1[s]$.

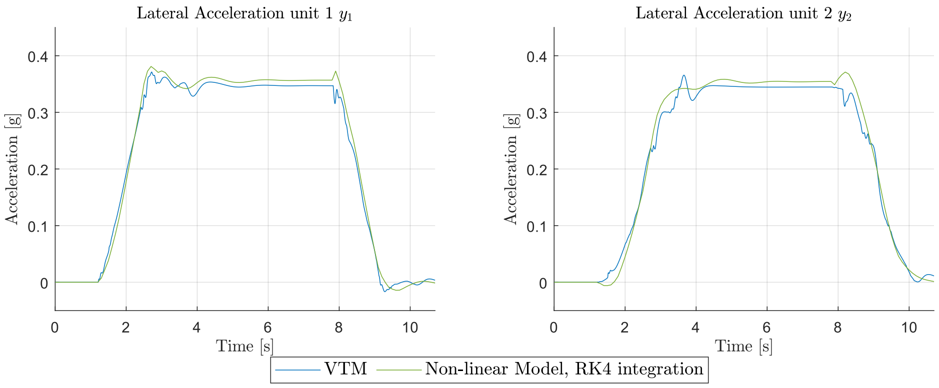

Figure B.16: Vehicle model outputs. Non-linear model with RK4 integration. $\Delta t = 0.1[s]$.

C

Numerical vehicle and tyre parameters

Table C.1: Numerical values for vehicle dynamics model.

Table redacted for Chalmers publication due to sensitive information.

DEPARTMENT OF ELECTRICAL ENGINEERING
CHALMERS UNIVERSITY OF TECHNOLOGY
Gothenburg, Sweden
www.chalmers.se

CHALMERS
UNIVERSITY OF TECHNOLOGY